Discrete Curvature Theories and Applications

Dissertation by

Xiang Sun

In Partial Fulfillment of the Requirements

For the Degree of

Doctor of Philosophy

King Abdullah University of Science and Technology, Thuwal,

Kingdom of Saudi Arabia

August 2016

EXAMINATION COMMITTEE APPROVALS FORM

The dissertation of Xiang Sun is approved by the examination committee

Committee Chairperson: Prof. Dr. Helmut Pottmann
Committee Members: Prof. Dr. Alexander Bobenko, Prof. Dr. Peter Wonka, Prof. Dr. Ying Wu

ABSTRACT

Discrete Curvature Theories and Applications

Xiang Sun

Discrete Differential Geometry (DDG) concerns discrete counterparts of notions and methods in differential geometry. This thesis deals with a core subject in DDG, discrete curvature theories on various types of polyhedral surfaces that are practically important for free-form architecture, sunlight-redirecting shading systems, and face recognition.

Modeled as polyhedral surfaces, the shapes of free-form structures may have to satisfy different geometric or physical constraints. We study a combination of geometry and physics – the discrete surfaces that can stand on their own, as well as having proper shapes for the manufacture. These proper shapes, known as circular and conical meshes, are closely related to discrete principal curvatures. We study curvature theories that make such surfaces possible.

Shading systems of freeform building skins are new types of energy-saving structures that can re-direct the sunlight. From these systems, discrete line congruences across polyhedral surfaces can be abstracted. We develop a new curvature theory for polyhedral surfaces equipped with normal congruences – a particular type of congruences defined by linear interpolation of vertex normals. The main results are a discussion of various definitions of normality, a detailed study of the geometry of such congruences, and a concept of curvatures and shape operators associated with the faces of a triangle mesh. These curvatures are compatible with both normal congruences and the Steiner formula.

In addition to architecture, we consider the role of discrete curvatures in face recognition. We use geometric measure theory to introduce the notion of asymptotic cones associated with a singular subspace of a Riemannian manifold, which is an

extension of the classical notion of asymptotic directions. We get a simple expression of these cones for polyhedral surfaces, as well as convergence and approximation theorems. We use the asymptotic cones as facial descriptors and demonstrate the practicability and accuracy of their applications in face recognition.

ACKNOWLEDGEMENTS

My most sincere and utmost thanks go to my advisor, Prof. Helmut Pottmann, for being incredibly supportive and heuristic. Helmut inspired me to the Ph.D. in the first place and relentlessly supported me even when the stress of the Ph.D. became overwhelming. The discussions I had with Helmut was always inspirational and insightful. For all these years Helmut guided me with his enthusiasm, brilliant mind and great attention to the details. He is, definitely, the best advisor I could ever think of.

Thanks to Prof. Alexander Bobenko, Prof. Peter Wonka and Prof. Ying Wu for devoting their valuable time to participate in my Ph.D. committee.

My collaboration with Prof. Johannes Wallner was a great pleasure. His wide knowledge and kindness have been a great support to the projects that we work together, and I learned a lot from him too. Big thanks to Prof. Jean-Marie Morvan for the immense help in geometry, especially the theory of normal cycles. The coffee breaks that we had been important parts of my Ph.D. life. My two visits to TU Wien was incredible and many of my ideas originated there. Thanks to Amir Vaxman, Doris Hotz and Prof. Martin Peternell for helping me during my stay in Vienna. I also appreciated my visit to Ecole Centrale de Lyon and my colleagues there: Prof. Liming Chen, Huaxiong Ding, Yinhang Tang and Wuming Zhang. Thanks them for bringing me to the area of face recognition.

The lively and social environment at the Visual Computing Center has made the whole experience incredibly more gratifying. My deep gratitude to my colleagues and former colleagues, Caigui Jiang, Yongliang Yang and Lubing Fan, who have been continuously supportive.

This thesis is dedicated to my family. Without their understanding, endless love and unconditional support, this dissertation would have never been possible.

TABLE OF CONTENTS

Chapter 1

Introduction

Geometry is perhaps one of the oldest subjects in mathematics. Its origin goes back to approximately 3000 B.C. in ancient Egypt. At that time, the Egyptians studied geometry and mainly used it in astronomy and architecture, building the famous Egyptian temples and pyramids [1]. Ever since then, various topics of geometry have been developed (see for example [2, 3]), and their applications range from the basic length, area, volume measurements to the sophisticated physics theory like the general relativity [4] and the string theory [5].

Today the connection of geometry with computer science brings in a new area of research called *discrete differential geometry (DDG)* [6]. The rich contents of applications in this area include many important topics such as geometric modeling [7], computer graphics [8, 9] and architectural design [10]. In all these applications mathematicians as well as the computer scientists have to deal with *discrete surfaces* or *meshes*, geometric objects that are represented by collections of points, edges, and faces. The reason is obvious as they are the suitable types of data that computers can process [11].

In 2009, Bobenko and Suris wrote the first monograph [12] on DDG. In this monograph they define the subject of discrete differential geometry as "aims at the development of discrete equivalents of notions and methods of smooth surface theory". They also address that the key message of this new geometry topic would be "discretize the whole theory, not just the equations". In this point of view, DDG is

more than some adoption of discretization schemes for partial differential equations but an independent branch of geometry in parallel with differential geometry. Indeed many research contributions as well as this thesis follow this insight, see for example [13, 14, 15].

One of the most important discrete concepts are the curvatures. *Discrete Curvatures* in DDG are analogies of curvatures in classic differential geometry. Whereas the curvatures of smooth manifolds (surfaces) are uniquely defined, there have been various kinds of definitions of discrete curvatures based on different applications and mathematical tools, see for example [16, 17, 18, 19, 14, 20, 21, 22, 23, 24, 25]. Some of them reach the same result, [14] and [23] obtain the same expression for the Gauss curvature in 3D, namely the angular defect formula. However in most cases the results are different. As an example in [22], the authors discuss the pros and cons of four *Discrete Laplace operators* and conclude that no one is better than the others in all aspects.

This thesis studies discrete curvature theories that are motivated by applications. We are interested in curvature theories that are useful in architectural design and face recognition. In the former case curvatures guide the design of the shapes and the later curvatures serve as features of the faces. In both instances, we elaborate the use of the integral form of definitions of classic curvatures in developing the new discrete curvatures.

1.1 Topics of the thesis

This thesis contributes to discrete curvature theories on triangle and planar quadrilateral meshes that are practically important for free-form architecture, sunlight-redirecting shading systems, and face recognition.

1.1.1 Principal meshes under static equilibrium

The free-form architectural design has two major considerations – the geometric shape of the underlying surfaces and the mechanics laws that a building has to fulfill.

One of the interesting geometric shapes for architectural design are the principal meshes. *Principal meshes* are meshes having vertex-offsets (*circular meshes*) or face-offsets (*conical meshes*). Such meshes have exact offests and are natural models for multi-layer free form structures [21]. They also have other advantages in manufacturing like the 'nearly rectangular panels' [26]. Principal meshes are also interesting theoretically, as they are, as the name indicates, a discretization of principal curvature lines [27, 28, 29].

For architectural applications, structural feasibility is of high importance. A simplified way of achieving it is to require static equilibrium, sometimes with the additional constraint of allowing compressive forces only and thus obtaining self-supporting structures [30, 31, 32, 33]. A subclass of principal meshes in force equilibrium are associated with structures that require a minimal amount of material to be built [34].

Whereas both principal meshes and meshes under static equilibrium are closely related to architecture, the combination of the two, however, has never been considered. We refer to such a mesh as *principal mesh under static equilibrium* or shortly PMSE, and it is one of the topics of this thesis. In this thesis we first discuss two basic approaches – a progating approach and a global optimization – that can both partially solve the problem of constructing PMSEs. Then we discuss the combination of the two that leads to a robust construction of PMSEs.

1.1.2 Vertex normals and face curvatures based on triangle meshes

The system of straight lines orthogonal to a surface (called the *normal congruence* of that surface) has close relations to the surface's curvatures and is a well-studied object

of classical differential geometry, see e.g. [35]. It is quite surprising that this natural correspondence has not been extensively exploited in discrete differential geometry: most notions of discrete curvature are constructed in a way not involving normals, or involving normals only implicitly. There are however applications such as support structures and shading/lighting systems in architectural geometry where line congruences, and in particular normal congruences, come into play [36]. We continue this study, elaborate on discrete congruences in more depth and present a novel discrete curvature theory for triangle meshes which is based on discrete line congruences.

1.1.3 Asymptotic Cones of Embedded Singular Spaces

We work in the framework of geometric measure theory, more specifically using the normal cycle theory, and use the formalism introduced in [37],[38] and [23] to propose an extension of the definition of the classical *asymptotic directions* to a large class of singular spaces $\mathcal{W}$. Instead of building a new "curvature measure" on any couple $(\mathcal{W}, M)$, we associate a map that assigns a *cone* (called an *asymptotic cone*) of vector fields on M to each Borel subset of M. In particular, if $M = \mathbb{E}^N$, we can reduce the target of this map to the set of quadratic cones of $\mathbb{E}^N$. Moreover, choosing a fixed scalar $r > 0$, we associate a field of cones leaving the tangent bundle $T\mathbb{E}^N$ with such a couple $(\mathcal{W}, \mathbb{E}^N)$.

1.2 Structure of the thesis

The remainder of the thesis is organized into five chapters. Chapter 2 reviews the related work on architectural geometry, 3D face recognition, and theories of normal cycles.

Chapter 3 deals with principal meshes under force equilibrium. We review the TNA and discuss the static equilibrium in Section 3.1. Section 3.2 briefly reviews the concept of mesh parallelism and two types of offset meshes. In Section 3.3 we

introduce an *equilibrium surface* and study the way of generating meshes from a few quads, which is a Cauchy-like problem. In Section 3.4 we introduce a robust approach that combines a standard global optimization with the Cauchy problem.

Chapter 4 discusses a discrete face curvature theory built on the normal congruences of discrete surfaces. Section 4.1 summarizes properties of smooth congruences and elaborates on an example arising in the context of linear interpolation of surface normals. Section 4.2 first recalls discrete congruences following the work of Wang et al. [36] and then focuses on the interesting geometry of a new version of discrete normal congruences (defined over triangle meshes). We shed new light onto the behavior of linearly interpolated surface normals and discuss the problem of choosing vertex normals. In Section 4.3, discrete congruences lead to a curvature theory for triangle meshes which has many analogies to the classical smooth setting. Unlike most other concepts of discrete curvature, it assigns values of the curvatures (principal, mean, Gaussian) to the faces of a triangle mesh. We discuss the internal consistency of this theory and demonstrate by examples (Section 4.4) its suitability for curvature estimation and other applications.

Chapter 5 studies the new concept of asymptotic directions of embedded singular spaces and its applications. Section 5.1 begins with classical definitions asymptotic curvatures of an (oriented $\mathcal{C}^\infty$) Riemannian manifold M (of finite dimension). Section 5.2 first reviews the geometry of the tangent bundle of M, and then introduces the so-called *asymptotic form* defined in that tangent bundle. Section 5.3 uses the theory of the normal cycle [39], [40] to introduce the notion of *asymptotic measures* defined in the tangent bundle of M, associated with a large class of singular subsets $\mathcal{G}$ (called *geometric subsets* in [39]). We describe them explicitly in classical situations (when $\mathcal{G}$ is smooth or a polyhedron). Then, we construct the *asymptotic cones*. In particular, we show how this construction generalizes the asymptotic directions defined on a smooth surface in $\mathbb{E}^3$. In particular, we give an explicit expression of

the asymptotic cones associated with a 2-polyhedron in $\mathbb{E}^3$. Section 5.4 deals with a general theorem of convergence of asymptotic cones. In particular, we give explicit assumptions in terms of the fatness of the sequence of polyhedra, implying the convergence of the sequence of cones for a suitable pseudo-metric. Section 5.5 presents two applications. First, we give a method to build asymptotic lines on a triangulation. Then, we give a method to approximate the asymptotic lines of a smooth surface approximated by a polyhedron. We test our method on various smooth or discrete surfaces. Section 5.6 briefly discuss the applications of the asymptotic cones in face recognition.

Chapter 6 concludes the thesis, summarizes its main contributions and outlines open problems and potential future work.

Chapter 2

Related work

2.1 Architectural geometry

Ever since its invention, geometry has always been an important and powerful tool in designing and constructing buildings [41, 42, 43, 44, 45, 46]. Pottmann was the first to introduce the words *architectural geometry* in his monograph [10] and demonstrates the importance of DDG in (free-form) architectural design. The Eiffel pavilion project [47] and the envelope of Yas Marina Hotel [48] are concrete examples of applications of architectural geometry.

A review of recent progress in architectural geometry can be found in the survey paper [26] by Pottmann et al. Liu et al. introduced the planar quad meshes and conical meshes in [27]. Pottmann et al. further developed the geometry of offset meshes and introduced circular and conical meshes [21, 28]. Bobenko et al. studied the curvature theory of these offset meshes in detail [25]. The method of *thrust network analysis* was investigated in detail by Block and coworkers [30, 31]. It was later combined with differential geometry by Vouga et al. in [32], thus stimulating further work in this direction [49, 50]. Tang et al. [33] found an effective optimization strategy which leads to an interactive design tool for meshes under static equilibrium and other geometric constraints.

2.2 Line congruences

Smooth line congruences represent a classical subject. An introduction may be found in the monograph by Pottmann and Wallner [51]. Discrete congruences have appeared both in discrete differential geometry and geometry processing. Let us first mention contributions which study congruences based on triangle meshes: A computational framework for normal congruences and for estimating focal surfaces of meshes with known or estimated normals has been presented by Yu et al. [52]. The paper by Wang et al. [36] is described in more detail below.

Congruences associated with quad meshes are discrete versions of parametrized congruences associated with parametrized surfaces. In particular, the so-called torsal parametrizations are discussed from the integrable systems perspective by Bobenko and Suris [12]. An earlier contribution in this direction is due to Doliwa et al. [53]. These special parametrizations also occur as node axes in torsion-free support structures in architectural geometry [27, 21, 28].

Curvatures of triangle meshes are well studied subjects. One may distinguish between numerical approximation schemes (such as the jet fitting approach [54] or integral invariants [55]) on the one hand, and extensive studies from the discrete differential geometry perspective on the other hand. Without going into any detail we mention that these studies include discrete exterior calculus [14], the geometry of offset-like sets and distance functions [23], or various ways of defining shape operators [56, 57]. Naturally, also Yu et al. [52] address this topic when studying discrete normal congruences and focal surfaces. We present here yet another definition of curvatures for triangle meshes which is based on discrete normal congruences, and which is at the same time motivated by the Steiner formula (which also plays an important role in [23] and [21, 25]).

2.3 Curvatures measures and geometric invariants

In the past decades, there has been a growing interest in defining geometric invariants describing singular spaces [58, 59, 16, 60, 37, 38, 61, 62, 63, 64, 65, 66, 23, 67]. Such invariants are generally subject to two assignments:

1. They must fit with the classical invariants when the underlying set is a smooth manifold or submanifold.

2. They must satisfy some continuity conditions. For instance, if a sequence of singular spaces tends (for a suitable topology) to a smooth space, then the invariants defined on the singular spaces also tend to the smooth ones.

After the length, the area and the volume, the most popular smooth geometric invariants are (sectional, Ricci, scalar, principal) curvatures, which are smooth functions (or tensors) defined on a (smooth) (sub)manifold and its tangent space. A classical approach to extending these curvatures to singular spaces $\mathcal{W}$ of a Riemannian manifold M, is to replace functions by measures on M. These measures are defined by integrating invariant differential forms over Borel subsets. As an example, Lipschitz-Killing curvature measures for singular spaces of a Riemannian manifold can be defined as follows:

- The first step is to generalize the unit normal bundle of a smooth submanifold to singular spaces. This has been done for convex subsets and for subsets of positive reach. More generally, the theory of the normal cycle [40] allows us to define an integral current on a large class of singular subsets, called geometric subsets of a Riemannian manifold, generalizing the unit normal bundle.

- The second step consists of defining standard differential forms on the tangent bundle of the ambient space.

- Finally, integrating these differential forms on the normal cycle, builds invariant measures, satisfying the two assignments described above.

2.4 3D curvature based face recognition

In the last few decades, biometrics is extensively used in computer science as a form of human identification and access control. With the development of 3D information acquisition technology, it is convenient to collect 3D data and thus face recognition (FR) has attracted increasing attention in recent years [68, 69].

Since 3D face sensors can accurately and sensitively capture the geometrical shape of the underlying 3D facial surfaces, designing a discriminating facial geometric surface feature is a critical issue in 3D face recognition. In general, the normal and the curvatures (e.g., the principal curvatures, the mean curvature and the Gaussian curvature) are the most commonly used geometric features to describe the facial local surface. Maes et al. applied the mean curvature in DoG based scale space to detect salient vertices and then adopted histogram of shape index (calculated with maximal curvature and minimal curvature) in local regions to build the descriptor [70]. Kakadiaris et al. analyzed the normal map and geometry image by using a wavelet transform [71]. Szeptycki et al. adopted the mean curvature and the Gaussian curvature to locate the most salient facial feature points (e.g., nose tip and two eye inner corners) [72]. Li et al. proposed a facial shape descriptor called multi-scale and multi-component local normal patterns that determines the orientation of a surface at each point and contains informative local surface shape information [73]. Tonchev et al. processed the curvature analysis and range image representation on the input point cloud [74]. Hwang et al. extended Gabor wavelet kernels by adding a spatial curvature term and adjusted the width of the Gaussian at the kernel for a low-resolution image [75].

Chapter 3

Principal Meshes Under Static Equilibrium

3.1 Thrust network analysis and static equilibrium

The introduction of *thrust network analysis* (TNA) in this section follows the papers by Block et al. [30, 31], Vouga et al. [32] and Tang et al. [33]. TNA was first applied to the vaulted masonry structures which are modeled as *self-supporting surfaces*.

Self-supporting surfaces. A structure, considered as an arrangement of blocks (bricks, stones), holds together by itself, with additional support present only during construction [32]. Such structure is assumed to follow two classic assumptions [76]:

Assumption 1: Masonry has no tensile strength, but the individual building blocks do not slip against each other (because of friction or mortar). On the other hand, their compressive strength is sufficiently high so that failure of the structure is by a sudden change in geometry and not by material failure.

Assumption 2 (The Safe Theorem): If a system of forces can be found which is in equilibrium with the load on the structure and which is contained within the masonry envelope then the structure will carry the loads, although the actual forces present may not be those postulated by that system.

Under these assumptions, Block et al. [30, 31] introduced a fictitious *thrust network* of discretized stresses contained in the masonry. This network is a system of forces in equilibrium with the structure's dead-load and turns out to be coherent with the classical finite element analysis discussed in [77]. A structure is self-supporting if

and only if it can carry a thrust network of only compressive forces.

Meshes under static equilibrium. In [32], Vouga et al. shown theoretically that TNA also applies to the thrust networks that possess both compressive and tensile forces. A structure that carries a thrust network under static equilibrium without requiring all forces to be compressive is called a *mesh under static equilibrium* [33]. The mathematical formulation is as follows:

A mesh $\mathcal{M}$ is represented by $\mathcal{M} = (V, E, F)$. Following [30] and [33], we discretized them as force densities W_i associated with vertices v_i. The load acting on this vertex is then given by $W_i = \frac{1}{2}\sum_{j\sim i}\rho_{ij}L_{ij}$, where $L_{ij} = ||\mathbf{v}_i - \mathbf{v}_j||$ is the length of an edge $\mathbf{v_i v}_j \in E$ and ρ_{ij} is the load density of that edge. In the following, we will consider uniform load density ρ over all edges unless stated otherwise. We assume that stresses are carried by the edges of the mesh: the force exerted on the vertex v_i by the edge connecting v_i, v_j is given by $\mathbf{f}_{ij} = w_{ij}(\mathbf{v}_i - \mathbf{v}_j)$. Tensile forces have $w_{ij} \leq 0$, while compressive forces have $w_{ij} \geq 0$. The *static equilibrium* (SE) at each vertex then reads as follows: With $\mathbf{v_i} = (\mathbf{x_i}, \mathbf{y_i}, \mathbf{z_i})$ we have

$$\sum_{j\sim i}\mathbf{f}_{ij} = [0, 0, W_i]^T. \tag{3.1}$$

or,

$$\sum_{j\sim i} w_{ij}(x_i - x_j) = \sum_{j\sim i} w_{ij}(y_i - y_j) = 0, \tag{3.2}$$

$$\sum_{j\sim i} w_{ij}(z_i - z_j) = W_i. \tag{3.3}$$

A mesh under static equilibrium has the static equilibrium at all its vertices, see of Figure 3.1. It can be seen that a mesh under static equilibrium can be represented by the thrust network it carries.

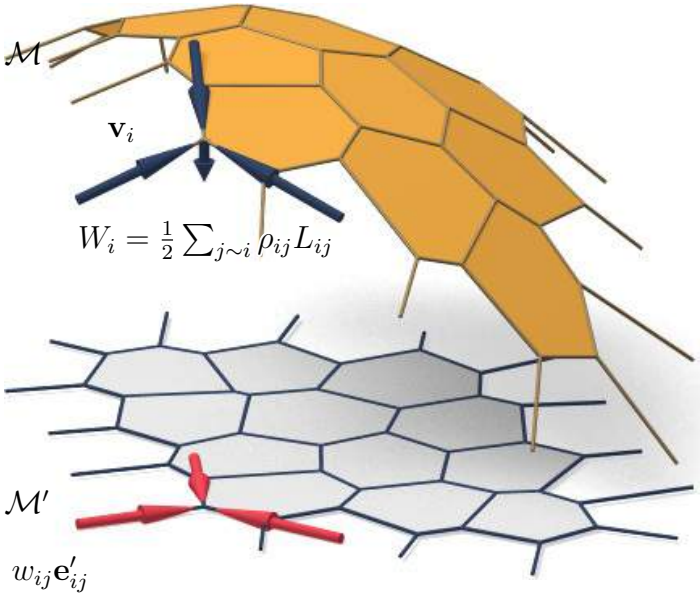

Figure 3.1: A mesh $\mathcal{M}$ (as well as the thrust network) under static equilibrium with dangling edges indicating external forces. This network together with its forces which balance vertical loads $\mathbf{W}_i$ projects onto a planar mesh $\mathcal{M}'$ with equilibrium forces $w_{ij}e'_{ij}$ in its edges.Figure from [32].

3.2 Mesh parallelism and principal meshes

The introduction to the mesh parallelism and the principal meshes in this section follows the papers by Pottmann et al.[21, 78, 28, 25]. The parallel meshes are particularly important in architectural geometry as they are very good models of multi-layer freeform structures [21, 10, 26].

Mesh parallelism. If mesh $\mathcal{M}$ has N vertices, we denote its vertices by the list $(m_1, ..., m_N) \in \mathbb{R}^{3N}$, see Figure 3.2. We use $\mathcal{C}(\mathcal{M})$ to denote the linear $3N$-dimensional space of meshes combinatorially equivalent to $\mathcal{M}$. If $\mathcal{M}^1$, $\mathcal{M}^2$ have the same combinatorics, a linear combination $\lambda_1\mathcal{M}^1 + \lambda_2\mathcal{M}^2$ is defined vertex-wise; this operation corresponds to the linear combination of vectors in $\mathbb{R}^{3N}$. Meshes $\mathcal{M}^1$, $\mathcal{M}^2$ with planar faces are *parallel* if they are combinatorially equivalent, and corresponding edges are parallel.

Offset meshes and exact offset meshes. Meshes are *offsets* of each other if they are parallel, and, in addition, their distance from each other is constant throughout the

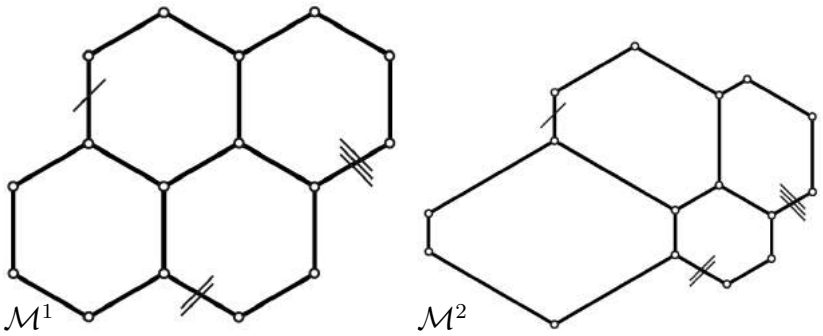

Figure 3.2: A pair of parallel meshes $\mathcal{M}^1$ and $\mathcal{M}^2$. Figure from [21].

mesh. The distance $d = \text{dist}(\mathcal{M}^1, \mathcal{M}^2)$ between two meshes $\mathcal{M}^1$, $\mathcal{M}^2$ can have different precise definitions and lead to different kinds of offsets. The offsets which are interesting in this thesis are the following two:

1. *vertex offsets*: The distance of corresponding vertices $\mathbf{m}_i^1, \mathbf{m}_i^2$ equals a constant d, which does not depend on the vertex.

2. *face offsets*: The distance of faces (actually, planes which carry faces) is independent of the face and equals d.

Discrete Gauss images. If $\mathbf{p}$ is a point of a smooth surface and $\mathbf{n}$ is the unit normal vector there, then $\bar{\mathbf{p}} = \mathbf{p} + d\mathbf{n}$ would be a point of an offset surface at distance d. If $\mathbf{p}, \bar{\mathbf{p}}$ are given, we can recover the unit normal vector by $\mathbf{n} = (\bar{\mathbf{p}} - \mathbf{p})/d$. If $\bar{\mathcal{M}}$ is an offset mesh of $\mathcal{M}$ we can mimic this construction and define a discrete Gauss image mesh $\mathcal{S} := (\bar{\mathcal{M}} - \mathcal{M})/d$, whose vertices $\mathbf{s}_i = (\bar{\mathbf{m}}_i - \mathbf{m}_i)/d$ can be regarded as discrete normal vectors.

Circular meshes and conical meshes. Consider a mesh $\mathcal{M}$, its offset mesh $\bar{\mathcal{M}}$ at distance d, and define the Gauss image mesh $\mathcal{S} = (\bar{\mathcal{M}} - \mathcal{M})/d$. Then the following is true:

1. $\bar{\mathcal{M}}$ is a vertex offset of $\mathcal{M} \Leftrightarrow$ the vertices of $\mathcal{S}$ are contained in the unit sphere $\mathbb{S}^2$. If $\mathcal{S}$ is a quad mesh and no edges degenerate, then $\mathcal{M}$ has a vertex offset if and only if $\mathcal{M}$ is a *circular mesh*, i.e., each face has a circumcircle.

2. $\bar{\mathcal{M}}$ is a face offset of $\mathcal{M} \Leftrightarrow$ the faces of the Gauss image mesh $\mathcal{S}$ are tangent to $\mathbb{S}^2$. A mesh has a face offset if and only if it is a *conical mesh*, i.e., the faces around a vertex are tangent to a cone of revolution.

Principal meshes. Circular meshes and conical meshes are together called *principal meshes* (PMs).

Principal meshes under force equilibrium. Principal meshes that are further under force equilibrium are called *principal meshes under static equilibrium* (PMSEs).

Isotropic principal meshes. Here we consider principal meshes in isotropic space, that is the *isotopic circular meshes* and *isotropic conical meshes*. An isotropic circular mesh is a mesh whose top-view is circular and isotropic conical mesh is its dual.

There is a natural force equilibrium of an isotropic circular mesh whose force diagram is dual of its top-view. In this case, the load is, in general, not the actual load.

3.3 Generating PMSEs from Cauchy data

In this section we discuss how to get PMSEs from a strip of quads with some additional conditions on both geometry and forces, that is, solving a Cauchy problem from some initial conditions on geometry and forces, and generate a PMSE layer by layer. See Figure 3.3(a).

3.3.1 The equilibrium surface

We first consider only the static equilibrium at each vertex. Let us look at a local situation depicted in Fig. 3.3(b): Given two quads $\mathbf{o}\mathbf{v}_1\mathbf{v}_{12}\mathbf{v}_2$ and $\mathbf{o}\mathbf{v}_4\mathbf{v}_{14}\mathbf{v}_1$, we would like to find vertex $\mathbf{v}_3$ of the next layer.

We also assume that forces $\mathbf{f}_1$ along edges $\mathbf{o}\mathbf{v}_1$ and $\mathbf{o}\mathbf{v}_2$ are known. Therefore in the static equilibrium condition 3.1, we have 5 unknowns: the force vector $\mathbf{f}_3$ along edge $\mathbf{o}\mathbf{v}_3$, the length L_3 and the magnitude of force $\mathbf{f}_4$ along edge $\mathbf{o}\mathbf{v}_4$. Meanwhile

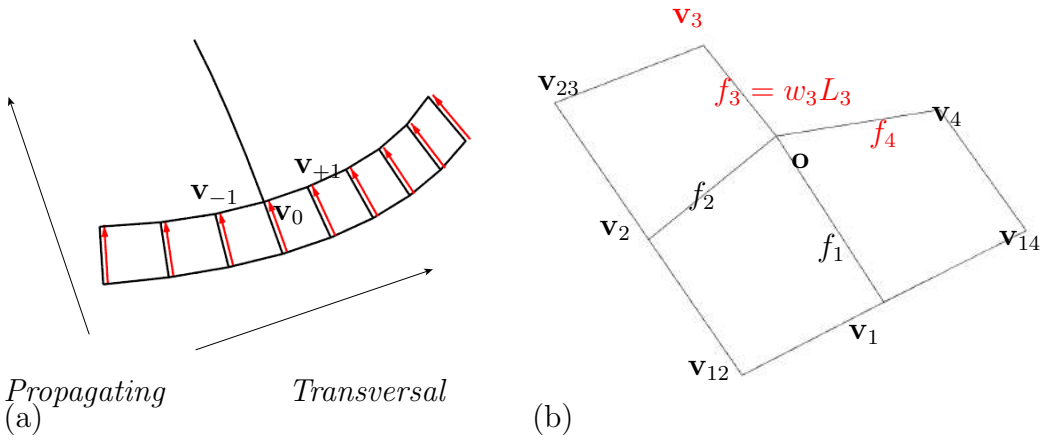

Figure 3.3: (a) A strip of quads (in transversal direction) and a polyline (in propagating direction) as a set of Cauchy data for finding PMSEs. (b) Finding $\mathbf{v}_3$ from neighbouring data. Quantities in black are known and those in red are unknown.

we have three equations in 3.1. Since we have two degrees of freedom, the set of all possible positions for $\mathbf{v}_3$ is generically a surface, which we call *equilibrium surface*.

For simplification we write $\mathbf{f_i} = f_i \mathbf{d}_i$ and $W = \sum_{i=1}^{4} \frac{1}{2}\rho L_i = -(\mu + \lambda L_3)$, where $\mathbf{d}_i$s are unit edge vectors of $\mathbf{ov}_i$s, and

$$\mu = -\frac{1}{2}\rho(L_1 + L_2 + L_4), \tag{3.4}$$

$$\lambda = -\frac{1}{2}\rho. \tag{3.5}$$

$\mathbf{d}_3$ is spherically parameterized as

$$\mathbf{d}_3 = (\cos\theta\cos\phi, \cos\theta\sin\phi, \sin\theta)^T, \quad \theta \in [-\pi/2, \pi/2], \phi \in [0, 2\pi). \tag{3.6}$$

The unknowns are L_3, f_3, f_4 and $\mathbf{d}_3$. With the unit vector $\mathbf{k} = [0, 0, 1]^T$ the static equilibrium condition 3.1 can be re-written as:

$$f_3\mathbf{d}_3 + f_4\mathbf{d}_4 + L_3\lambda\mathbf{k} = -f_1\mathbf{d}_1 - f_2\mathbf{d}_2 - \mu\mathbf{k} =: \mathbf{r} \tag{3.7}$$

It is easy to solve this linear system for f_3, f_4, L_3, with $\mathbf{d}_4 = [d_{4x}, d_{4z}, d_{4z}]^T$ and $\mathbf{r} = [r_x, r_y, r_z]^T$:

$$L_3 = \frac{(d_{4y}r_z - d_{4z}r_y)\cos\phi + (d_{4z}r_x - d_{4x}r_z)\sin\phi + (d_{4x}r_y - d_{4y}r_x)\tan\theta}{\lambda(d_{4y}\cos\phi - d_{4x}\sin\phi)}. \tag{3.8}$$

We are interested in the implicit equation $F(x, y, z) = 0$ of the equilibrium surface. Using the relations

$$\begin{aligned} x^2 + y^2 + z^2 &= L_3^2, \\ x &= L_3\cos\theta\cos\phi, \\ y &= L_3\cos\theta\sin\phi, \\ z &= L_3\sin\theta, \end{aligned} \tag{3.9}$$

we find that the equilibrium surface is in general an algebraic surface of order 4 and has the form

$$F(x,y,z) = (x^2+y^2+z^2)(ex+fy)^2-(ax+by+cz)^2 = 0, \quad (ax+by+cz)\cdot(ex+fy) \geq 0. \tag{3.10}$$

Here, the coefficients are

$$\begin{aligned} &a = d_{4y}r_z - r_y d_{4z}, \quad b = -d_{4x}r_z + r_x d_{4z}, \quad c = d_{4x}r_y - r_x d_{4y}, \\ &e = -\rho d_{4y}/2, \quad f = \rho d_{4x}/2, \quad \mathbf{r} = -f_1\mathbf{d}_1 - f_2\mathbf{d}_2 + \rho(L_1 + L_2 + L_4)\mathbf{k}/2. \end{aligned} \tag{3.11}$$

The surface always contains a straight line in the plane $ex + fy = 0$,

$$x = t; \quad y = -et/f; \quad z = (af - be)/cf \cdot t. \tag{3.12}$$

We discuss two special cases arose from the expression (3.10).

Vertical edge. $e = f = 0$, $\Rightarrow d_{4x} = d_{4y} = 0$, $d_{4z} = \pm 1$; This means that edge $\mathbf{ov}_4$ is

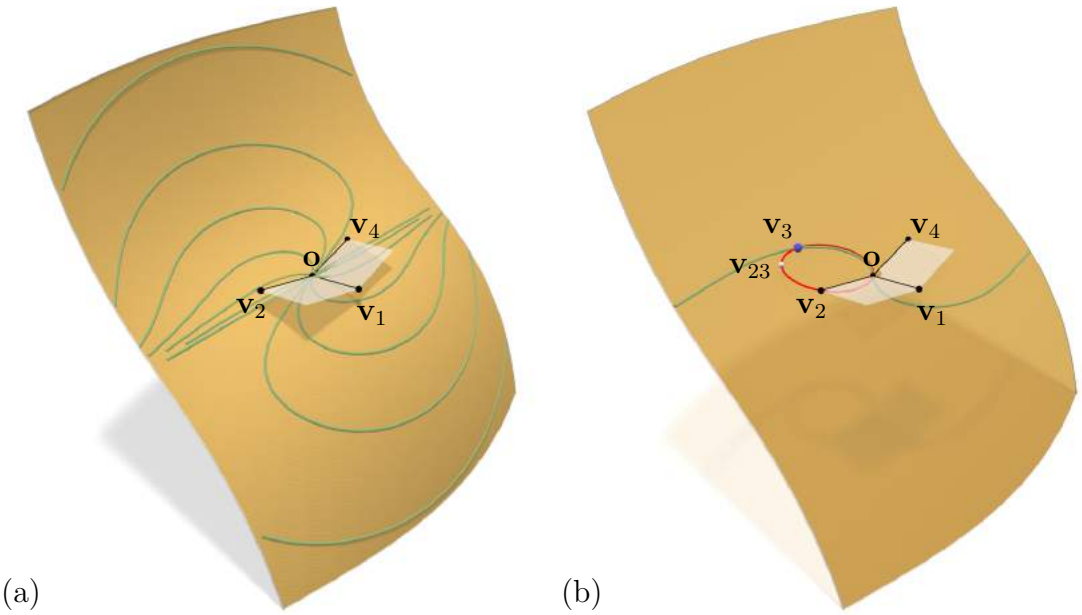

(a) (b)

Figure 3.4: (a) The equilibrium surface of $\mathbf{v}_3$. The green curves are its intersection with different planes through edge $\mathbf{ov}_2$. (b) A circle through points $\mathbf{o}$, $\mathbf{v}_2$ and $\mathbf{v}_{23}$ is drawn in red. The green curve is the intersection of the equilibrium surface with the plane through the circle

vertical. We also have $a = -r_y d_{4z}$, $b = r_x d_{4z}$, $c = 0$, and the equilibrium surface is reduced to a vertical plane:

$$(f_1 d_{1y} + f_2 d_{2y})x - (f_1 d_{1x} + f_2 d_{2x})y = 0. \tag{3.13}$$

This is a case where *overhang* [33] happens. If we further look at the static equilibrium equation (3.7), the system is singular as $\det(\mathbf{A}) = [\mathbf{d}_3, \mathbf{d}_4, \lambda\mathbf{k}] = [\mathbf{d}_3, \pm\mathbf{k}, \lambda\mathbf{k}] = 0$. We have the following relations

$$f_3 = \frac{\sqrt{r_x^2 + r_y^2}}{\cos\theta} = \frac{\sqrt{(f_1 d_{1x} + f_2 d_{2x})^2 + (f_1 d_{1y} + f_2 d_{2y})^2}}{\cos\theta} \tag{3.14}$$

$$\pm f_4 = \rho L_3/2 - \sqrt{r_x^2 + r_y^2}\tan\theta + r_z. \tag{3.15}$$

If edge $\mathbf{ov}_4$ carries a force that exactly counter-balances its own weight, that is,

$\pm f_4 = \rho L_4/2$, we can remove this edge without affecting the whole thrust network and then L_3 is given by

$$\begin{aligned} L_3 =& \frac{2}{\rho}(\sqrt{r_x^2 + r_y^2}\tan\theta - r_z + L_4) \\ =& \frac{2}{\rho}(\sqrt{r_x^2 + r_y^2}\tan\theta + f_1 d_{1z} + f_2 d_{2z} - \frac{1}{2}\rho(L_1 + L_2 + L_4)) + L_4 \\ =& \frac{2}{\rho}(\sqrt{(f_1 d_{1x} + f_2 d_{2x})^2 + (f_1 d_{1y} + f_2 d_{2y})^2}\tan\theta + f_1 d_{1z} + f_2 d_{2z}) \\ & - L_1 - L_2. \end{aligned} \tag{3.16}$$

Degenerated edge. $a = b = c = 0$; This means that $L_3 = 0$, and, for any $\mathbf{y} \in \mathbb{R}^3$,

$$[\mathbf{y}, \mathbf{d}_4, \mathbf{r}] = a y_x + b y_y + c y_z = 0 \Rightarrow \mathbf{d}_4 \parallel \mathbf{r}. \tag{3.17}$$

We further check the value of f_3:

$$f_3 = \frac{[\mathbf{r}, \mathbf{d}_4, \lambda\mathbf{k}]}{[\mathbf{d}_3, \mathbf{d}_4, \lambda\mathbf{k}]} = -\frac{\lambda c}{[\mathbf{d}_3, \mathbf{d}_4, \lambda\mathbf{k}]} = 0. \tag{3.18}$$

This reduces to the case of a point $\mathbf{o}$ of valence 3. In this case if only the geometry is given, i.e. $\mathbf{d}_i$, L_i $(i = 1, 2, 4)$ are known, we can find, generically, a unique force triple.

3.3.2 Circularity and identifying $\mathbf{v}_3$ on the equilibrium surface

Picking point $\mathbf{v}_3$ on the equilibrium surface ensures static equilibrium at vertex $\mathbf{o}$. We would like to enforce further conditions on the geometry of the mesh such as planar faces or even faces with a circum-circle. To achieve planarity of the quad $\mathbf{o}\mathbf{v}_2\mathbf{v}_{23}\mathbf{v}_3$, we need to intersect its plane with the equilibrium surface. With $\mathbf{n}$ as unit normal

vector of that plane, this leads to the following relation between ϕ and θ,

$$\begin{aligned} &< \mathbf{n}, \mathbf{d}_3 >= 0 \\ \Rightarrow &\tan\theta = -\frac{n_x \cos\phi + n_y \sin\phi}{n_z}. \end{aligned} \tag{3.19}$$

This results in a parametric representation of the intersection curve, i.e. the locus of possible vertices $\mathbf{v}_3$.

To identifying $\mathbf{v}_3$ that both ensures static equilibrium and circularity, we further intersect this curve with the circle and get the point $\mathbf{v}_3$ see Figure 3.4(b).

3.3.3 A Cauchy problem

The discussion of equilibrium surfaces in Section 3.3.1 shows that in order to find a unique $\mathbf{v}_3$, we need to prescribe an additional point $\mathbf{v}_{23}$. As illustrated in Figure 3.3(a), we define initial data for geometry and statics as follows.

Initial data. *Initial geometry data* consist of a polyline in the propagation direction $\mathbf{s}$ and a strip of planar quads in the transversal direction $\mathbf{t}$. *Initial static data* are the forces along the propagating edges of the strip.

In order to compute the mesh layer by layer, we may begin with vertex $\mathbf{v}_0$ which is the point where the polyline meets the strip, see Figure 3.3(a). At this point the adjacent geometry is already given by the initial static data, one force is also given. The forces along the other three edges can then be determined and are generically unique.

Next we may deal with vertex $\mathbf{v}_{+1}$, which now plays the same role as point $\mathbf{o}$ in our study of the equilibrium suface. We just need two more constraints to fix the position of the free vertex. In this way we can propagate our computation in $+\mathbf{t}$-direction and then the same applies to the $-\mathbf{t}$-direction. Once the current layer is determined we can compute the next layer and generate the desired mesh. By picking different constraints, the disscussion above can be summarized into the following three results.

Proposition 3.1 A quad mesh under static equilibrium is in general determined by the initial Cauchy data if and only if exactly two constraints are prescribed at every vertex. See Figure 3.5.

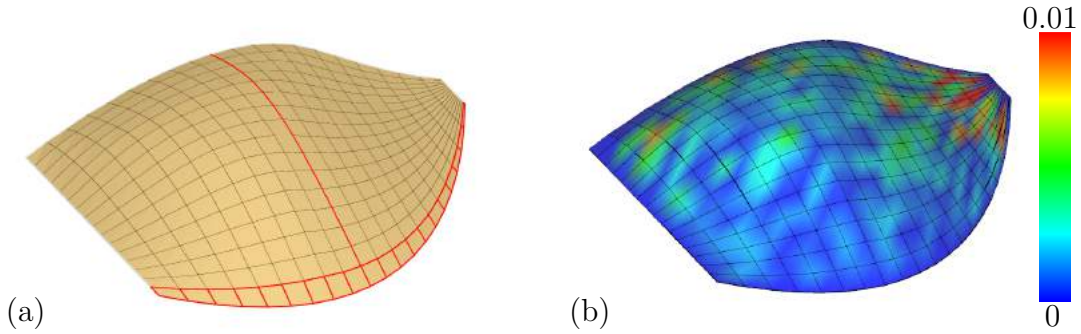

Figure 3.5: (A) A quad mesh under static equilibrium from the initial data (red lines). At each equilibrium surface, the constraints are $\mathbf{o}'\mathbf{v}'_3 = -\mathbf{o}'\mathbf{v}'_1$ and $L_1 = L_3$, see Figure 3.3(b) for notations; the primes indicate the projection onto a horizontal plane. (b) The static equilibrium measurement (3.31) for this mesh.

Proposition 3.2 A planar quad mesh under static equilibrium is determined by the initial Cauchy data if and only if the quads of the input strip are planar and exactly one constraint is prescribed at each vertex. See Figure 3.6.

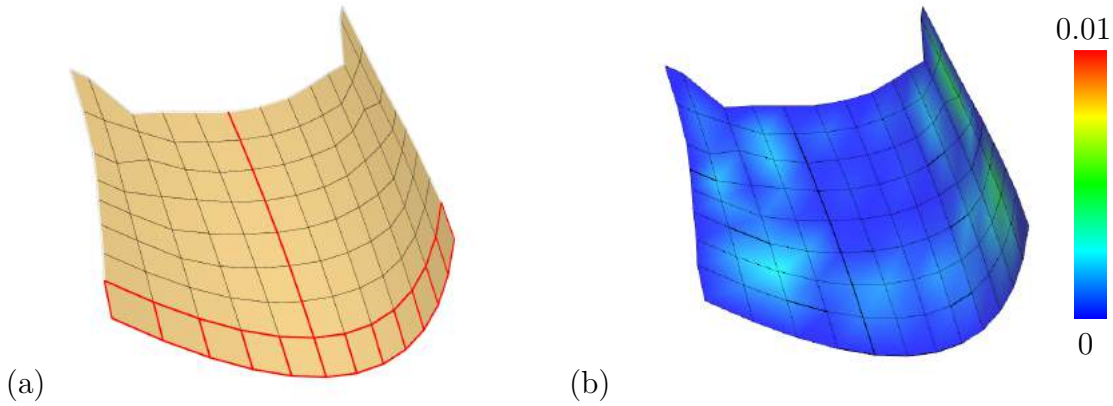

Figure 3.6: (a) A planar quad mesh under static equilibrium from the initial data (red lines). At each vertex, the constraint is $\mathbf{o}'\mathbf{v}'_3 = -\mathbf{o}'\mathbf{v}'_1$, see Figure 3.3(b) for notations; the primes indicate the projection onto a horizontal plane. (b) The static equilibrium measurement (3.31)for this mesh.

This one constraint, in other words, one degree of freedom of determining each vertex gives flexibility of computing planar quad meshes under static equilibrium (PQSE). One could prescribe a uniform constraint, for example as in Figure 3.6. More interestingly one can prescribe different constraints dynamically during the computations and achieve different shapes of PQSEs. This flexibility also shows reason why shape exploration of PQSES using method of *guided projection* in [33] is very effective.

Proposition 3.3 A circular mesh under static equilibrium is determined by the initial Cauchy data if and only if the quads of the input strip are circular. See Figure 3.7.

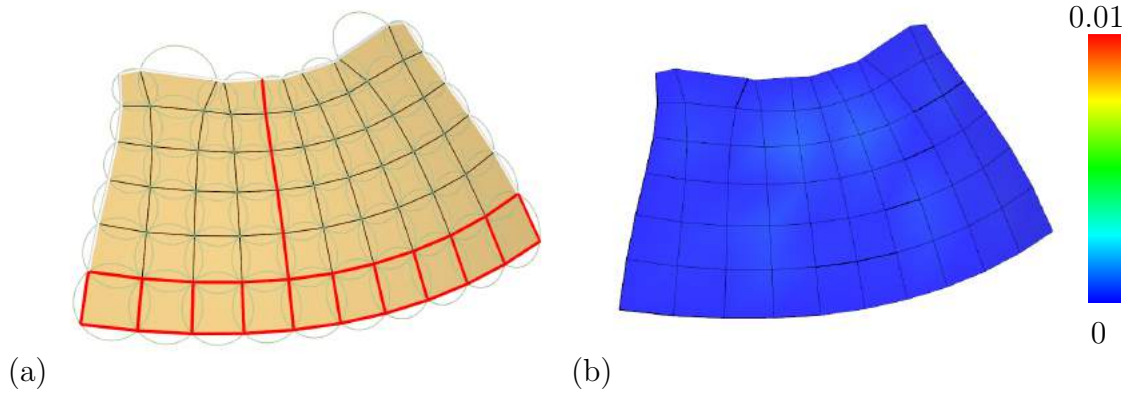

Figure 3.7: (a) A circular mesh under static equilibrium from the initial data (red lines). (b) The static equilibrium measurement (3.31)for this mesh.

3.3.4 Quality of the Cauchy data and fairness of a mesh

The point $\mathbf{v}_3$ found by the intersection of the circle and the equilibrium surface does not even need to be real, needless to say being at a 'good' position that is satisfactory for applications. In applications, especially for architecture, one uses various concepts of mesh fairness [27, 26, 33] that can control the aesthetics of polylines in a mesh.

In order to get a simple formula, we make some reasonable simplification on our data. We assume that all edges in the star of the central point $\mathbf{o}$ have the same length and have a rather symmetric location with respect to the horizontal plane through $\mathbf{o}$

(see Fig. 3.8).

This allows us to choose a basis with $\mathbf{d}_1 = [0, \cos\delta, \sin\delta]^T$, $\mathbf{d}_3 = [0, -\cos\theta, \sin\theta]^T$ (that is, $\phi = -\frac{\pi}{2}$) and $\mathbf{d}_2 = [\alpha, 0, \gamma]^T$, $\mathbf{d}_4 = [-\alpha, 0, \gamma]^T$. Moreover, we have $L_1 = L_2 = L_4 = L$. Then, we have the expression for $\mathbf{r}$

$$\begin{aligned}\mathbf{r} &= -f_1\mathbf{d}_1 - f_2\mathbf{d}_2 - \mu\mathbf{k} = -f_1\begin{bmatrix}0\\ \cos\delta\\ \sin\delta\end{bmatrix} - f_2\begin{bmatrix}\alpha\\ 0\\ \gamma\end{bmatrix} + \frac{3}{2}\rho L\begin{bmatrix}0\\ 0\\ 1\end{bmatrix} \\ &= \left[-f_2\alpha, -f_1\cos\delta, -f_1\sin\delta - f_2\gamma + 3\rho L/2\right]^T,\end{aligned} \tag{3.20}$$

If we also require that $L_3 = L$ then,

$$\begin{aligned}L = L_3 &= \frac{(d_{4y}r_z - d_{4z}r_y)\cdot 0 + (d_{4z}r_x - d_{4x}r_z)\cdot(-1) + (d_{4x}r_y - d_{4y}r_x)\tan\theta}{\lambda(d_{4y}\cdot 0 - d_{4x}\cdot(-1))} \\ &= \frac{-\alpha(-f_1\sin\delta - f_2\gamma + 3\rho L/2) - \gamma(-f_2\alpha) + (-\alpha)(-f_1\cos\delta)\tan\theta}{-\rho/2\cdot(-\alpha)} \\ &= \frac{f_1(\sin\delta + \cos\delta\tan\theta) + 2f_2\gamma - 3\rho L/2}{\rho/2}.\end{aligned} \tag{3.21}$$

Finally, we arrive at the following *fairness condition*:

$$2\rho L = f_1(\sin\delta + \cos\delta\tan\theta) + 2f_2\gamma. \tag{3.22}$$

Special case. If $\mathbf{d}_i$ and the xy-plane form small angles, that is, $\sin\delta \approx \tan\delta = d_{1z}$, $\cos\delta \approx 1$. Since $\tan\theta = d_{3z}$, $\gamma = d_{2z} = d_{4z}$ and by assuming $f_i = f$ we obtain the following simpler relation.

$$2\rho L = f\sum_{i=1}^{4} d_{iz}. \tag{3.23}$$

We define the ratio

$$\frac{f\sum_{i=1}^{4} d_{iz}}{2\rho L}, \tag{3.24}$$

which in the ideal case should be equal to one. Deviation from this value may result in

bad or even useless configurations, as illustrated in Fig. 3.8. shows how this condition affects the result of $\mathbf{v}_3$.

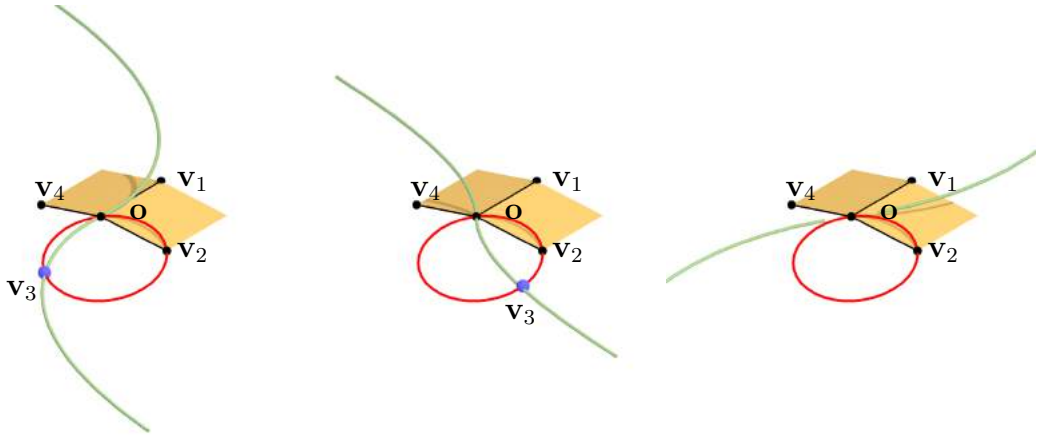

(a) Ratio 1 (b) Ratio 2 (b) Ratio 1/2

Figure 3.8: Different intersections when the ratio $\frac{f\sum_{i=1}^{4} d_{iz}}{2\rho L}$ varies. (a) The ratio is exactly 1 and the point $\mathbf{v}_3$ computed ensures a 'good' fairness located at $\mathbf{o}$. (b) The ratio is 2 and the point $\mathbf{v}_3$ locates at position which is not fair. (c). The ration is 1/2 and there is no real intersection point at a position other than $\mathbf{o}$.

We remark that the fairness condition is local and as the computation proceeds, it may no longer be satisfied. Such case, see Figure 3.9, leads to the discussion of a more robust method in the next section.

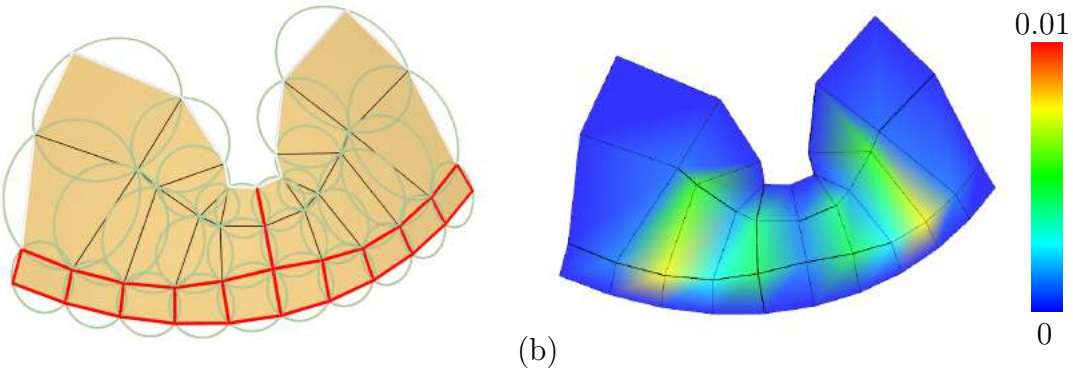

(a) (b)

Figure 3.9: The computation of a circular mesh from initial data (red lines). The first two layers from the bottom follows the fairness condition (3.22) but the computation soon leads to an undesired shape, though the resulting mesh is still a PMSE.

3.4 Global optimization

In this section, we introduce a global approach that can avoid the violation of the fairness condition (3.22) and enables relatively complex shapes of PMSE. We first review a standard nonlinear optimization which could, in some cases, get good results. Then we combine it with the Cauchy problem discussed in the previous section so that we can compute more PMSEs with good precision.

3.4.1 A direct optimization

The direct optimization we used is a standard nonlinear optimization, and we solve it by the Levenberg-Marquardt algorithm[79]. In the formulation, we introduce auxiliary variables as in [33] to increase the sparsity of the linear system. The objective function has form

$$E = \sum_i \alpha_i E_i \tag{3.25}$$

where each energy function E_i is non-negative and will be discussed below and $\alpha_i \geq 0$ are weights of the energy term.

As illustrated in Figigure 3.10(a), we introduce as auxiliary variables the face normal $\mathbf{n}$, face circum-circle center $\mathbf{c}$ and face circum-circle radius r. The circularity energy is:

$$E_c = \sum_{quads} ((\mathbf{c} - \mathbf{v}_i) \cdot \mathbf{n})^2 + ((\mathbf{c} - \mathbf{v}_i)^2 - r^2)^2 \tag{3.26}$$

In the computation, we assume that the material (line) density is normalized to one, i.e. $\rho = 1$. The energy term for static equilibrium

$$E_s = \sum (\sum_{j \sim i} w_{ij}(x_i - x_j))^2 + (\sum_{j \sim i} w_{ij}(y_i - y_j))^2 + (\sum_{j \sim i} w_{ij}(z_i - z_j) - W_i)^2. \tag{3.27}$$

As in [33], the load and the edge lengths are treated as auxiliary variables and we

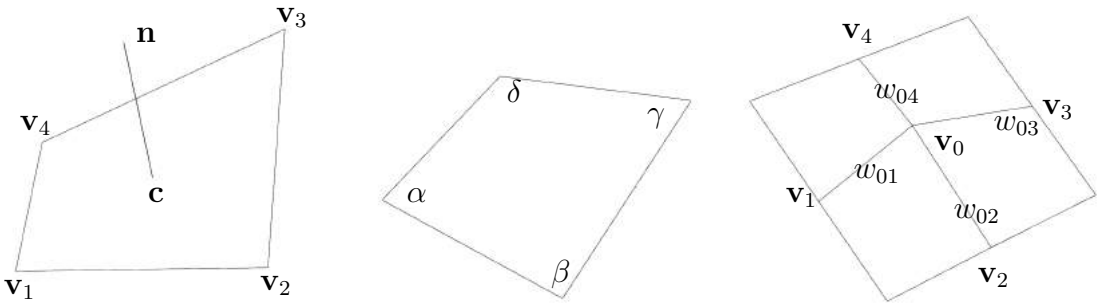

(a) (b) (c)

Figure 3.10: (a) Variables and auxiliary variables in circularity optimization (b) Circularity measurement (c) Static equilibrium measurement.

further have extra energy terms:

$$E_w = \sum (W_i - \frac{1}{2} \sum_{j \sim i} L_{ij}), \tag{3.28}$$

$$E_e = \sum_e (L_{ij}^2 - (\mathbf{v}_i - \mathbf{v}_j)^2). \tag{3.29}$$

We also use *soft energies* such as the *tangential fairness*, *proximity* and *gliding boundary* from [33].

Measurements

The *circularity measurement* M_c is the deviation in the angles from being circular, see Figure 3.10(b). To be more explicit, it is defined as

$$M_c = \max(|\pi - \alpha - \gamma|, |\pi - \beta - \delta|). \tag{3.30}$$

The *static equilibrium measurement* M_s, see Figure 3.10(c), is defined as

$$M_s = \sqrt{(\sum_{j \sim i} w_{ij}(x_i - x_j))^2 + (\sum_{j \sim i} w_{ij}(y_i - y_j))^2 + (\sum_{j \sim i} w_{ij}(z_i - z_j) - W_i)^2}. \tag{3.31}$$

Initialization. Since our objective has two major targets: circularity and static equilibrium, an initial input mesh in the optimization could be one of the following two:

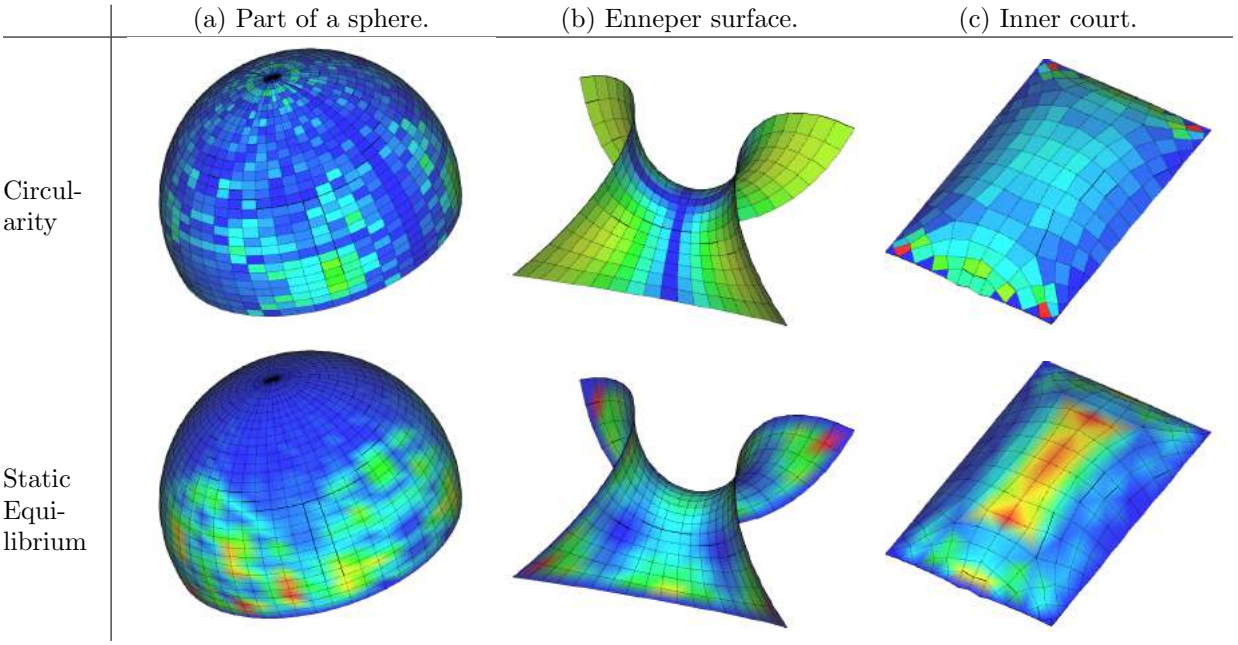

Figure 3.11: Some symmetric meshes which can be directly optimized to be PMSE. (a) The initial mesh is a circular mesh which is quadrangulated from the latitudes and longitudes of a sphere. (b) The initial mesh is a circular mesh which is quadrangulated from the principal curvature lines of an Enneper surface. (c) Th initial mesh is a mesh under static equilibrium from [33]. See Table 3.1 for the statics of the circularity and static equilibrium measurement.

1. A circular mesh with forces computed by a least square method, for instance, as in [33].

2. A planar quad mesh under static equilibrium.

Some special meshes with symmetry can be optimized for PMSE with relatively good quality, see Figure 3.11 whereas most cannot, see Figure 3.12 and Table 3.1. The direct optimization, in general, struggles to obtain a PMSE with a satisfactory precision.

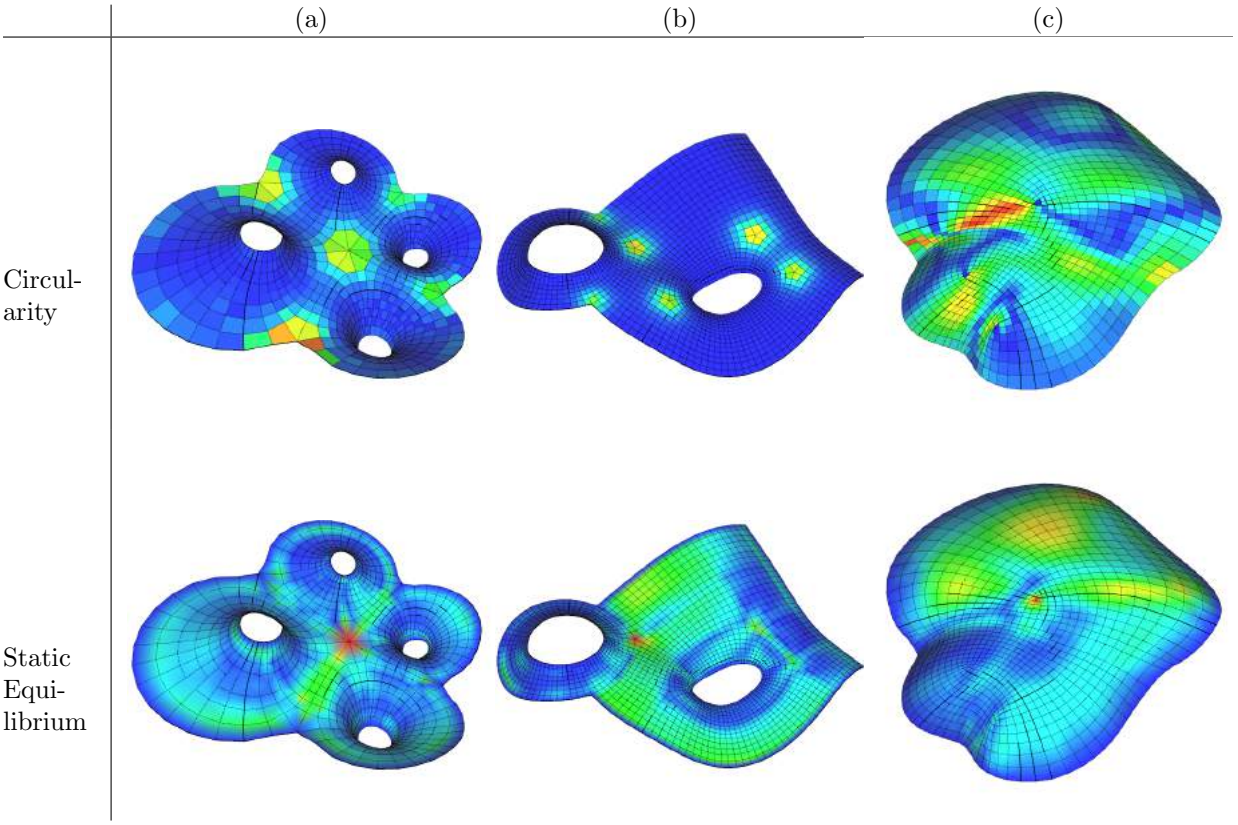

Figure 3.12: Results of a direct optimization with a circular or static equilibrium initial input. (a) and (b) The initial meshes are circular meshes from [80]. (b) The initial mesh is a mesh under static equilibrium from [33]. See table 3.1 for the statistics of the circularity and static equilibrium measurement.

	Part of a sphere		Enneper surface		Inner court	
	$M_c(^\circ)$	M_s	$M_c(^\circ)$	M_s	$M_c(^\circ)$	M_s
max	$3.82 \cdot 10^{-3}$	$2.25 \cdot 10^{-3}$	0.211	$3.35 \cdot 10^{-3}$	0.631	2.02
min	0	$7.28 \cdot 10^{-8}$	0	$1.70 \cdot 10^{-4}$	$1.25 \cdot 10^{-4}$	0
mean	$1.21 \cdot 10^{-1}$	$1.00 \cdot 10^{-3}$	$5.23 \cdot 10^{-4}$	$3.86 \cdot 10^{-4}$	$1.15 \cdot 10^{-1}$	$5.66 \cdot 10^{-1}$
	Figure 3.12(a)		Figure 3.12(b)		Figure 3.12(c)	
	$M_c(^\circ)$	M_s	$M_c(^\circ)$	M_s	$M_c(^\circ)$	M_s
max	9.07	11.3	2.36	11.1	$7.02 \cdot 10^{1}$	$3.74 \cdot 10^{-2}$
min	$2.73 \cdot 10^{-4}$	$9.00 \cdot 10^{-2}$	$3.81 \cdot 10^{-5}$	$2.40 \cdot 10^{-2}$	$6.37 \cdot 10^{-2}$	$3.16 \cdot 10^{-4}$
mean	$5.67 \cdot 10^{-1}$	1.49	$1.11 \cdot 10^{-1}$	1.94	$2.19 \cdot 10^{1}$	$9.31 \cdot 10^{-3}$

Table 3.1: Statistics of circularity measurements M_c and static equilibrium measurements M_s correspond to the models in Figure 3.11 and 3.12. Value 0 means that the value hits the machine precision.

3.4.2 A combined approach

In order to get a PMSE by optimization, we would need a better initialization, a mesh that is more "close" to PMSE than a circular mesh or a mesh under static equilibrium. We, therefore, propose the following method which combines the computation of PMSE from Cauchy data and the global optimization:

1. Start with a set of initial geometry and static data.
2. Compute the approximated PMSE for the next few layers.
3. Optimize the current existing layers.
4. Repeat from Step 2 until one obtains the full mesh.

Step 1. Initial data. The initial geometry data is a strip of circular quads. The initial static data can be estimated from the fairness condition 3.22 or 3.23.

Step 2. Computation from Cauchy data. In this step, we compute the new layers of the mesh largely the same as Section 3.3.3, see Figure 3.15(b,d,f). The only difference is that we may need to alter the new point computed for each quad (point $\mathbf{v}_3$ in Section 3.3.2). In the computation, the mesh fairness could be bad, due to the error accumulation that occurs inevitably in such a propagating computation, or violation of the fairness condition. In this case, we compute the new layers "approximately" with "acceptable" fairness. To be more precise, as illustrated in Figure. 3.13, at each vertex we prescribe a feasible region of fairness $\mathcal{F}$, which is the set of points that ensures the fairness at $\mathbf{o}$. We then compute the point $\mathbf{v}_3$ that is the exact intersection of the equilibrium surface and the circle. Instead of using $\mathbf{v}_3$ as the mesh vertex, we project it to the nearest point $\bar{\mathbf{v}}_3$ within $\mathcal{F}$ and add the projection $\bar{\mathbf{v}}_3$ to the mesh.

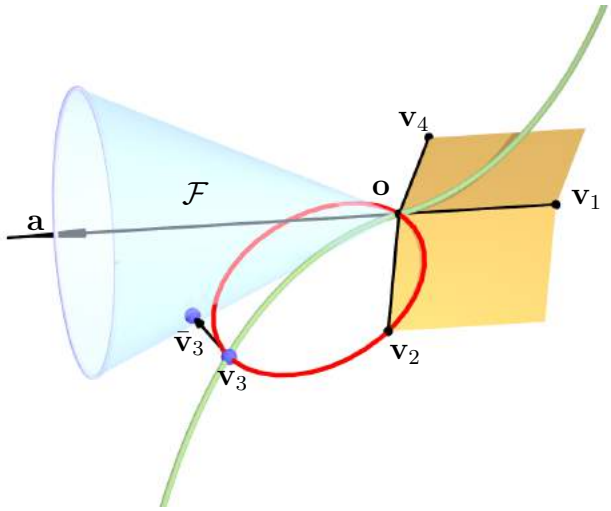

Figure 3.13: The feasible region of fairness is a right circular cone with apex $\mathbf{o}$ and axis $\mathbf{a} = -\mathbf{o}\mathbf{v}_1$. The projection point $\bar{\mathbf{v}}_3$ is the new mesh vertex.

Step 3. Optimization of the partial mesh. We optimize the current partial mesh for PMSE as in Section 3.4.1 and redistribute the forces. The top layer together with the forces are the new Cauchy data for the next step, see Figure 3.15(c,e,g).

Adapting the combined method, we can obtain a PMSE that is both precise in circularity and static equilibrium, see Figure 3.14

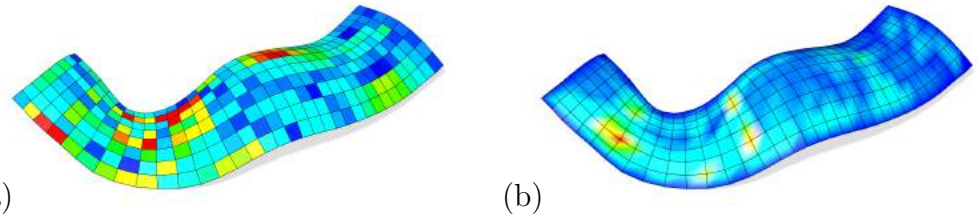

(a) (b)

Figure 3.14: A PMSE computed by the combined method. (a) Circularity $M_c(^\circ)$ max/min/mean: $1.2 \cdot 10^{1}/1.6 \cdot 10^{-3}/3.2 \cdot 10^{-1}$. (b) Static equilibrium M_s max/min/mean: $3.0 \cdot 10^{-3}/3.1 \cdot 10^{-5}/4.7 \cdot 10^{-4}$.

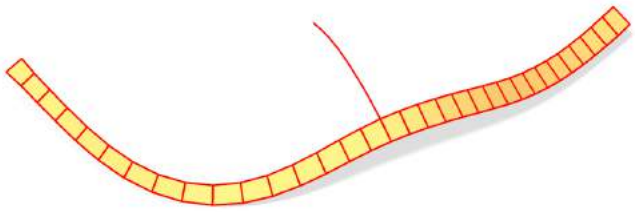

(a) The input Cauchy data.

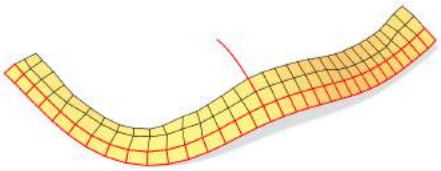

(b) Three-layer PMSE computed.

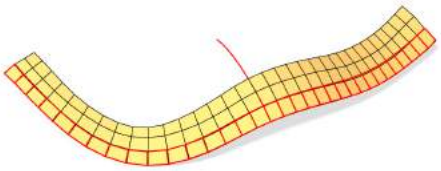

(c) Three-layer PMSE optimized.

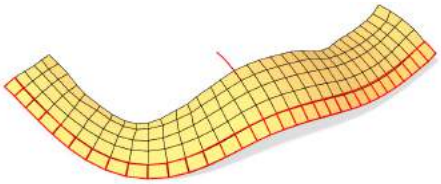

(d) Five-layer PMSE computed.

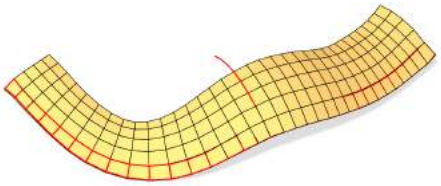

(e) Five-layer PMSE optimized.

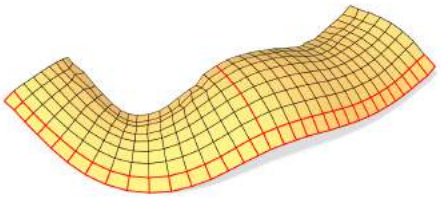

(f) Full PMSE computed.

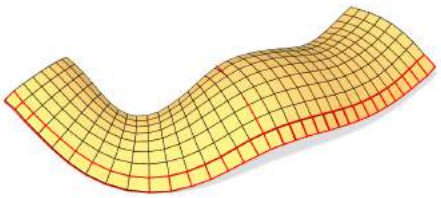

(g) Full PMSE optimized.

Figure 3.15: Steps of the combined method that computes a PMSE.

Chapter 4

Vertex normals and face curvatures of triangle meshes

4.1 Smooth line congruences

The introduction into line congruences in this section follows the paper by Wang et al. [36]. A line congruence $\mathcal{L}$ is a smooth 2D manifold of lines described locally by lines $L(u,v)$ which connect corresponding points $\mathbf{a}(u,v)$ and $\mathbf{b}(u,v)$ of two surfaces. With $\mathbf{e}(u,v) = \mathbf{b}(u,v) - \mathbf{a}(u,v)$ indicating the direction of the line $L(u,v)$ (see Fig. 4.1), we employ the volumetric parametrization

$$\mathbf{x}(u,v,\lambda) = \mathbf{a}(u,v) + \lambda\mathbf{e}(u,v) = (1-\lambda)\mathbf{a}(u,v) + \lambda\mathbf{b}(u,v).$$

Any 1-parameter family $\mathcal{R}(t) = L(u(t),v(t))$ of lines results in a ruled surface $\mathbf{r}(t,\lambda) = \mathbf{x}(u(t),v(t),\lambda)$ contained in the congruence. We are particularly interested in *developable* ruled surfaces: The developability condition reads

$$\begin{aligned} &u_t^2[\mathbf{e}_u,\mathbf{a}_u,\mathbf{e}] + u_t v_t([\mathbf{e}_u,\mathbf{a}_v,\mathbf{e}] + [\mathbf{e}_v,\mathbf{a}_u,\mathbf{e}]) + v_t^2[\mathbf{e}_v,\mathbf{a}_v,\mathbf{e}] \\ &= (u_t, v_t) \begin{pmatrix} [\mathbf{e}_u,\mathbf{a}_u,\mathbf{e}] & [\mathbf{e}_u,\mathbf{a}_v,\mathbf{e}] + [\mathbf{e}_v,\mathbf{a}_u,\mathbf{e}] \\ \text{symm.} & [\mathbf{e}_v,\mathbf{a}_v,\mathbf{e}] \end{pmatrix} \begin{pmatrix} v_t \\ u_t \end{pmatrix} = 0, \end{aligned} \tag{4.1}$$

if we use subscripts to indicate differentiation and square brackets for the determinant. Equation (4.1) tells us that for any (u,v) there are up to two so-called *torsal* directions $u_t : v_t$ which belong to developable surfaces. This behaviour is quite analogous to the

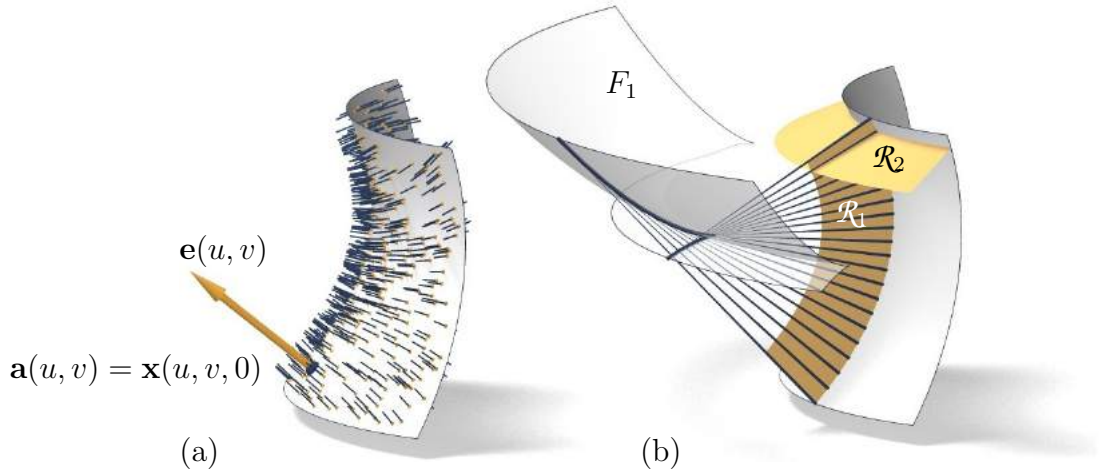

Figure 4.1: (a) A line congruence $\mathcal{L}$ is described by a surface $\mathbf{a}(u,v)$, and direction vectors $\mathbf{e}(u,v)$. (b) Developables $\mathcal{R}_1$, $\mathcal{R}_2$ contained in $\mathcal{L}$. The set of all regression curves c_i of these developables makes up the focal sheets F_1, F_2 of the congruence (here only F_1 is shown). The tangent planes of $\mathcal{R}_1$, $\mathcal{R}_2$ along the common line are the torsal planes or focal planes of that line. These images are taken from [36].

fact that for any point in a smooth surface there are two *principal* tangent directions which belong to principal curvature lines. By integrating the torsal directions one creates ruled surfaces which are developable, which is analogous to finding principal curvature lines by integrating principal directions.

4.1.1 Normal Congruences

The normals of a surface constitute the normal congruence of that surface. For such congruences the analogy between torsal directions and principal directions mentioned above is actually an equality: The surface normals along a curve form a developable surface if and only if that curve is a principal curvature line [35].

The reference surface $\mathbf{a}(u,v)$ might be the base surface the lines of $\mathcal{L}$ are orthogonal to, but this does not have to be the case. The congruence does not change if the reference surface is changed to $\mathbf{a}^*(u,v) = \mathbf{a}(u,v) + \lambda(u,v)\mathbf{e}(u,v)$, so deciding whether or not $\mathcal{L}$ is a normal congruence depends on existence of an alternative reference surface $\mathbf{a}^*$ orthogonal to the lines of $\mathcal{L}$, i.e., $\langle \mathbf{e}, \mathbf{a}^*_u \rangle = \langle \mathbf{e}, \mathbf{a}^*_v \rangle = 0$. Assuming without loss of generality that $\|\mathbf{e}(u,v)\| = 1$ and using $\langle \mathbf{e}, \mathbf{e}_u \rangle = \langle \mathbf{e}, \mathbf{e}_v \rangle = 0$ the orthogonality

condition reduces to $\lambda_u = -\langle \mathbf{a}_u, \mathbf{e} \rangle$, $\lambda_v = -\langle \mathbf{a}_v, \mathbf{e} \rangle$. This PDE for the function λ has a solution if and only if the integrability condition $\lambda_{uv} = \lambda_{vu}$ holds. It is easy to see that this is equivalent to

$$\langle \mathbf{a}_u, \mathbf{e}_v \rangle = \langle \mathbf{a}_v, \mathbf{e}_u \rangle. \tag{4.2}$$

It is not difficult to see that (4.2) is equivalent to the condition that developables contained in $\mathcal{L}$ intersect at right angles.

4.1.2 Focal surfaces and focal planes

Loosely speaking, an intersection point of a line in $\mathcal{L}$ with an infinitesimally neighbouring line produces a *focal point* of the congruence $\mathcal{L}$. The rigorous definition of focal point is a point $\mathbf{x}(u, v, \lambda)$ where the derivatives of $\mathbf{x}$ are not linearely independent: One gets the condition

$$[\mathbf{x}_u, \mathbf{x}_v, \mathbf{x}_\lambda] = [\mathbf{e}_u, \mathbf{e}_v, \mathbf{e}]\lambda^2 + \big([\mathbf{a}_u, \mathbf{e}_v, \mathbf{e}] + [\mathbf{e}_u, \mathbf{a}_v, \mathbf{e}]\big)\lambda + [\mathbf{a}_u, \mathbf{a}_v, \mathbf{e}] = 0, \tag{4.3}$$

i.e., up to two focal points per line. It is not difficult to see that such singularities are exactly the singularities of developables contained in $\mathcal{L}$, see Figure 4.1b. For this reason, the tangent planes of developables contained in $\mathcal{L}$ are called *focal planes* as well as *torsal planes*. Such a focal plane/torsal plane is spanned by a line $L(u, v)$ together with a torsal direction.

For normal congruences, the focal points are precisely the principal centers of curvature; they exist always unless one of the principal curvatures is zero. In each point of the surface, the focal plane (i.e., torsal plane) is spanned by the surface normal and a principal tangent.

4.1.3 Example: Congruences defined by linear interpolation

Congruences of the special form

$$\begin{aligned}\mathbf{x}(u,v,\lambda) &= (1-\lambda)\big(\mathbf{a}_0+\mathbf{a}_{10}u+\mathbf{a}_{20}v\big)+\lambda\big(\mathbf{b}_0+\mathbf{b}_{10}u+\mathbf{b}_{20}v\big) \\ &= \big(\mathbf{a}_0+\mathbf{a}_{10}u+\mathbf{a}_{20}v\big)+\lambda\big(\mathbf{e}_0+\mathbf{e}_{10}u+\mathbf{e}_{20}v\big)\end{aligned} \tag{4.4}$$

play an important role, both for us and in other places: for example, the set of lines described by such a congruence is the one generated by Phong shading, when one linearly interpolates vertex normals in a triangle.

We consider the planes "P_α" which are defined as the set of all points $\mathbf{x}(u,v,\alpha)$, and we study the affine mappings

$$\phi_{\alpha\beta} : P_\alpha \to P_\beta, \quad \mathbf{x}(u,v,\alpha) \mapsto \mathbf{x}(u,v,\beta).$$

The lines $L(u,v)$ of the congruence are precisely the lines which connect points $\mathbf{x}(u,v,\alpha) \in P_\alpha$ and $\mathbf{x}(u,v,\beta) \in P_\beta$. These congruences are studied e.g. in [51, Ex. 7.1.2]. Let us summarize some of their properties, which are illustrated by Figure 4.2.

1. Each intersection line $L = P_\alpha \cap P_\beta$ of two planes in the family P_λ is contained in the congruence $\mathcal{L}$. This follows from the fact that L is spanned by the points $X = \phi_{\alpha\beta}^{-1}(L) \cap L$ and $\phi_{\alpha\beta}(X) = L \cap \phi_{\alpha\beta}(L)$.

2. The lines $P_\alpha \cap P_\beta$ with α fixed, constitute a developable surface $\mathcal{R}_\alpha \subset \mathcal{L}$ which is planar and contained in P_α (in general, it is the tangent surface of a parabola r_α).

3. For properties of the focal surface, see Figure 4.2.

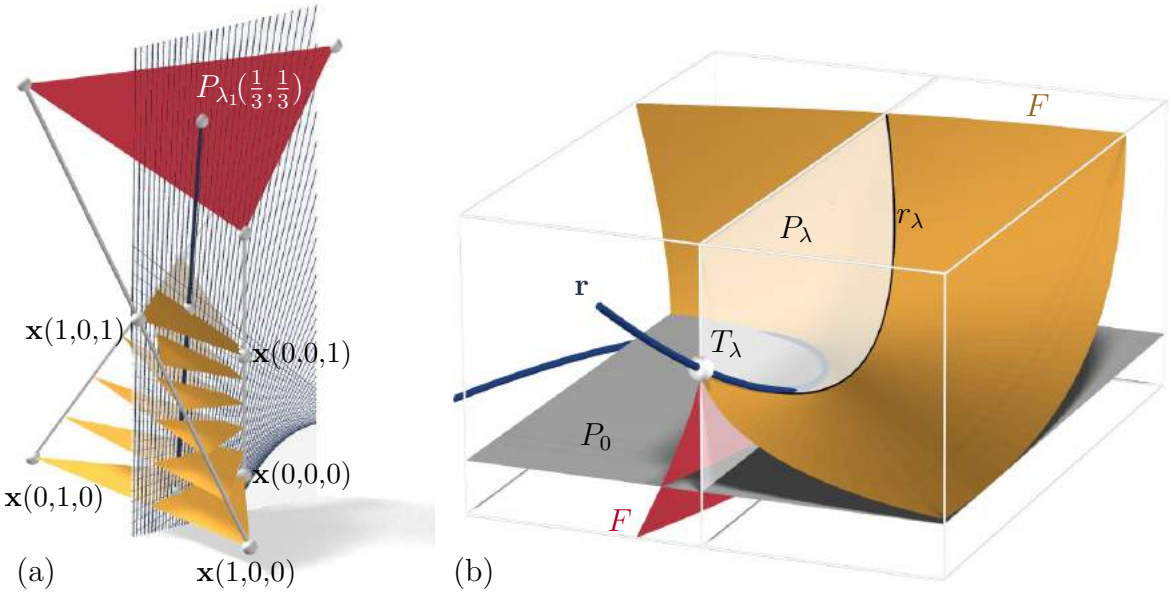

Figure 4.2: Congruences defined by a "linear" volumetric parametrization $\mathbf{x}(u, v, \lambda)$ turn out to be useful for linear interpolation of triangle meshes, but they have counter-intuitive properties. (a) Planes P_λ defined by $\lambda = \text{const.}$ are visualized as triangles. Interestingly, all of these triangles contain a planar developable $\mathcal{R}_\lambda \subset \mathcal{L}$ with a parabola r_λ as curve of regression. In particular the red triangle P_{λ_1} represents a torsal plane for the blue line $L(\frac{1}{3}, \frac{1}{3})$ which connects the barycenters of triangles P_λ. The image further shows many lines $P_{\lambda_1} \cap P_\beta$, of the planar developable $\mathcal{R}_{\lambda_1}$. (b) The focal surface F of $\mathcal{L}$ agrees with the envelope of the family of planes P_λ. It is in general the tangent surface of a cubic polynomial curve $\mathbf{r}$. We show in red and yellow the two sheets of this tangent surface F which are separated by the regression curve $\mathbf{r}$. We also indicate the point of tangency T_λ where P_λ touches $\mathbf{r}$. The hyperbolic congruence lines (those which are contained in two focal planes) are bitangents of the focal surface, i.e., they touch F in two points. The regression parabolas r_λ are contained in F and are obtained by intersecting F with one of its tangent planes P_λ.

4.2 Discrete Normal Congruences

Wang et al. [36] define discrete congruences by means of correspondences between combinatorially equivalent triangle meshes A, B with vertices $\{\mathbf{a}_i\}$ and $\{\mathbf{b}_i\}$. Each pair of corresponding triangles $\mathbf{a}_i\mathbf{a}_j\mathbf{a}_k$ and $\mathbf{b}_i\mathbf{b}_j\mathbf{b}_k$ defines, via linear interpolation, a

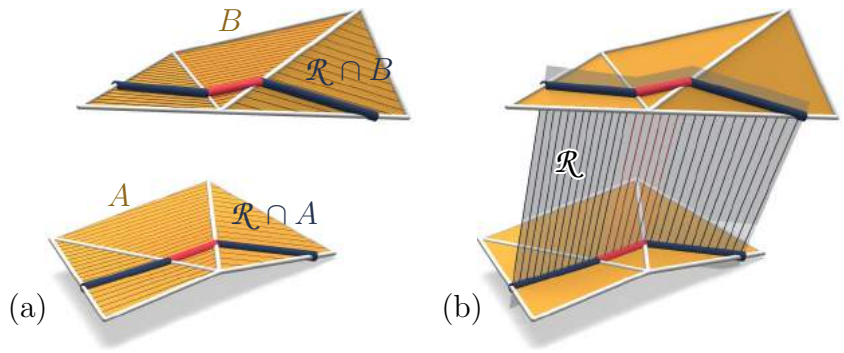

Figure 4.3: A piecewise-linear correspondence between meshes A and B defines a piecewise-smooth congruence $\mathcal{L}$. (a) Integrating torsal directions yields corresponding polylines in meshes A and B. (b) Connecting corresponding points of those two polylines yields a piecewise-flat developable $\mathcal{R} \subset \mathcal{L}$. These images are taken from [36].

piece of a smooth line congruence of the kind described by Equation (4.4):

$$\mathbf{x}(u,v,\lambda) = \mathbf{a}(u,v) + \lambda \mathbf{e}(u,v), \tag{4.5}$$

$$\mathbf{a}(u,v) = \mathbf{a}_i + u\mathbf{a}_{ji} + v\mathbf{a}_{ki}, \quad \mathbf{e}(u,v) = \mathbf{e}_i + u\mathbf{e}_{ji} + v\mathbf{e}_{ki}, \quad \text{where}$$

$$\mathbf{e}_i = \mathbf{b}_i - \mathbf{a}_i, \quad \mathbf{a}_{ij} = \mathbf{a}_i - \mathbf{a}_j, \quad \mathbf{e}_{ij} = \mathbf{e}_i - \mathbf{e}_j.$$

If the domain is restricted to $u \geq 0$, $v \geq 0$, $u + v \leq 1$, then the correspondence $\mathbf{x}(u,v,0) \longmapsto \mathbf{x}(u,v,1)$ is precisely the affine mapping of triangle $\mathbf{a}_i\mathbf{a}_j\mathbf{a}_k$ to triangle $\mathbf{b}_i\mathbf{b}_j\mathbf{b}_k$. Equations (4.1) and (4.3) serve to compute torsal directions and focal points of this congruence, and also to trace the developables contained in this congruence (see Fig. 4.3).

4.2.1 Discrete normal congruences – Version 1

It is not straightforward to define which correspondence between triangle meshes defines a *normal* congruence. Firstly this is because congruences of the form (4.4) are never normal except for degenerate cases. Secondly such a normal congruence would automatically lead to a good definition of constant-distance offset mesh of a triangle

mesh which is lacking so far.

We discuss two suitable definitions of "normal congruence" and start with a version already published. Wang et al. [36] require normality to hold only in the barycenters of faces (i.e., they require that Equation (4.2) holds for barycenters of faces), see Figure 4.4. Figure 4.5 shows an example demonstrating the efficiency of this definition. Proposition 4.1 below gives an equivalent analytic condition.

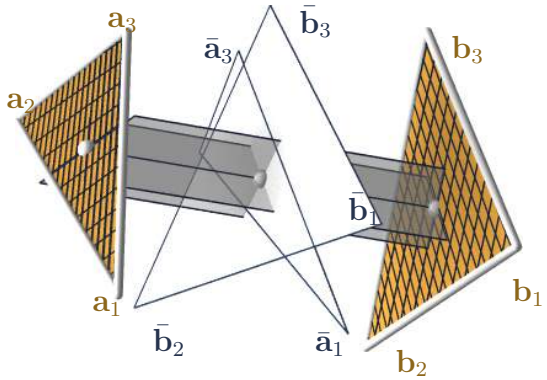

Figure 4.4: (a) Congruences defined by the piecewise-affine correspondence of meshes A, B can be called *discrete-normal*, if the normality condition is fulfilled for barycenters of faces. This figure also illustrates the auxiliary projection used by Equation (4.7). This normality condition is called 'version 1 normality' here (image taken from [36]).

Proposition 4.1 Consider two combinatorially equivalent triangle meshes and the line congruence $\mathcal{L}$ defined by the piecewise-linear corresondence of faces. For each pair $\mathbf{a}_1\mathbf{a}_2\mathbf{a}_3$, $\mathbf{b}_1\mathbf{b}_2\mathbf{b}_3$ of corresponding faces perform orthogonal projection in direction of the line which connects their respective barycenters, yielding triangles $\bar{\mathbf{a}}_1\bar{\mathbf{a}}_2\bar{\mathbf{a}}_3$, $\bar{\mathbf{b}}_1\bar{\mathbf{b}}_2\bar{\mathbf{b}}_3$. Then $\mathcal{L}$ is normal in the barycenters of the two faces if and only if the following analogue of (4.2) holds:

$$\langle \bar{\mathbf{a}}_j - \bar{\mathbf{a}}_i, \bar{\mathbf{b}}_k - \bar{\mathbf{b}}_i \rangle = \langle \bar{\mathbf{a}}_k - \bar{\mathbf{a}}_i, \bar{\mathbf{b}}_j - \bar{\mathbf{b}}_i \rangle, \quad \text{or equivalently,} \tag{4.6}$$

$$\langle \bar{\mathbf{a}}_j - \bar{\mathbf{a}}_i, \bar{\mathbf{e}}_k - \bar{\mathbf{e}}_i \rangle = \langle \bar{\mathbf{a}}_k - \bar{\mathbf{a}}_i, \bar{\mathbf{e}}_j - \bar{\mathbf{e}}_i \rangle, \quad \text{where} \quad \mathbf{e}_i = \mathbf{b}_i - \mathbf{a}_i. \tag{4.7}$$

It is sufficient that these conditions hold for at least one choice of indices $i, j, k \in \{1, 2, 3\}$, $i \neq j \neq k$.

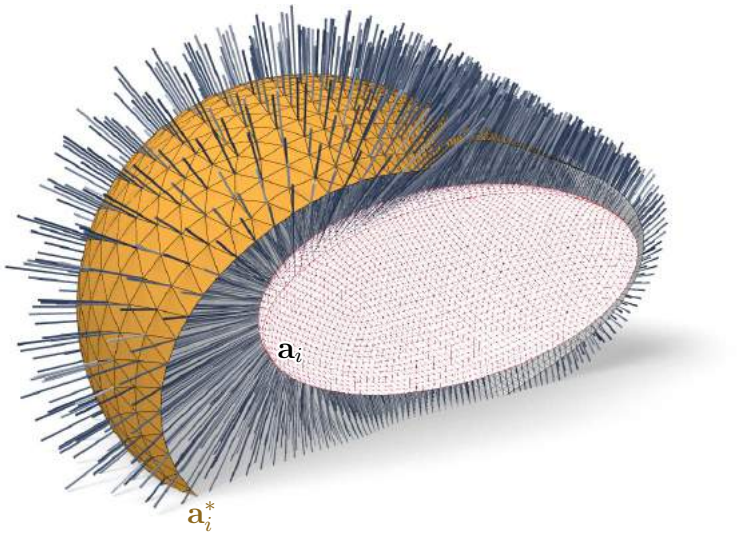

Figure 4.5: We demonstrate that Equation (4.7) is a working definition of normality: Given a triangle mesh $\{\mathbf{a}_i\}$ (white), we find unit vectors $\mathbf{e}_i$ by optimizing for shading effects according to Wang et al. [36] under the normality constraint (4.7). Subsequently we check if a triangle mesh $\{\mathbf{a}_i^*\}$ orthogonal to the congruence can be found. We let $\mathbf{a}_i^* = \mathbf{a}_i + \lambda_i \mathbf{e}_i$ and solve for λ_i such that the faces of the new mesh are orthogonal to the congruence in their barycenters. The result of this computation yields a mesh $\{\mathbf{a}_i^*\}$ (yellow) where face normals and congruence lines (in face barycenters) differ by an angle β, which assumes a maximum of 4.1°, a mean of 0.9°, and a median of 0.8°. Instead of the mesh computed here, any constant-distance offset would have been a solution as well. We chose one which lies at a small distance from the original mesh.

4.2.2 Discrete normal congruences – Version 2

There is an obvious analogy between conditions (4.2) and (4.7): they express normality in the smooth and discrete cases respectively. However Equation (4.7) is not entirely satisfying as a definition since it involves a projection operator. It is therefore natural to define discrete-normality by the following two equations which replace Equations (4.6), (4.7):

$$\langle \mathbf{a}_j - \mathbf{a}_i, \mathbf{b}_k - \mathbf{b}_i \rangle = \langle \mathbf{a}_k - \mathbf{a}_i, \mathbf{b}_j - \mathbf{b}_i \rangle \quad \text{or, equivalently,} \tag{4.6*}$$

$$\langle \mathbf{a}_j - \mathbf{a}_i, \mathbf{e}_k - \mathbf{e}_i \rangle = \langle \mathbf{a}_k - \mathbf{a}_i, \mathbf{e}_j - \mathbf{e}_i \rangle. \tag{4.7*}$$

We will show that theses conditions are suitable to define normality of discrete congru-

ences defined by a correspondence of triangle meshes. Besides numerical experiments (see later), we show geometric properties of congruences which fulfill these conditions. The first property is a discrete version of the following two facts (i) A normal congruence $\mathcal{L}$ has a 1-parameter family of surfaces orthogonal to it, and (ii) for any point in such a surface there are 3 mutually orthogonal planes spanned by the normal and the two principal directions. We show that in the discrete-normal case, there are analogous *principal trihedra*:

Proposition 4.2 Consider two combinatorially equivalent triangle meshes and the line congruence $\mathcal{L}$ defined by the piecewise-affine corresondence of faces, and consider in particular one such pair $\mathbf{a}_1\mathbf{a}_2\mathbf{a}_3$, $\mathbf{b}_1\mathbf{b}_2\mathbf{b}_3$ of corresponding faces. In the generic case, the normality condition (4.6*) implies the following property:

For each plane P_λ spanned by the vertices $(1-\lambda)\mathbf{a}_i + \lambda\mathbf{b}_i$ there is a congruence line $N_\lambda = L(u_\lambda, v_\lambda)$ such that the two focal planes of that line together with P_λ form a trihedron of mutually orthogonal planes.

The meaning of "generic" is discussed in the proof.

Proof. Generically, vectors $\mathbf{e}_i = \mathbf{b}_i - \mathbf{a}_i$ are linearly independent, so we can express a normal vector $\mathbf{n}$ of the triangle $\mathbf{a}_1\mathbf{a}_2\mathbf{a}_3$ (which spans P_0) as a linear combination $\mathbf{n} = \sum_{i=1}^{3} \alpha_i \mathbf{e}_i$. Generically, $\sum \alpha_i \neq 0$, so by multiplying $\mathbf{n}$ with a factor we can achieve $\sum \alpha_i = 1$ and by relabeling the coefficients α_i we get $\mathbf{n} = (1-u-v)\mathbf{e}_1 + u\mathbf{e}_2 + v\mathbf{e}_3$. Then Equation (4.5) shows that the line $L(u,v)$ is orthogonal to P_0.

Consider the affine correspondence of triangles $\mathbf{a}_1\mathbf{a}_2\mathbf{a}_3$ and $\mathbf{b}_1\mathbf{b}_2\mathbf{b}_3$ followed by orthogonal projection onto P_0. A vertex $\mathbf{a}_i$ is mapped to $\bar{\mathbf{b}}_i = \mathbf{b}_i + \lambda_i\mathbf{n}$. There is a linear mapping α with $\alpha(\mathbf{a}_i - \mathbf{a}_j) = \bar{\mathbf{b}}_i - \bar{\mathbf{b}}_j$. It is clear from Figure 4.3 that the eigenvectors of α indicate the directions of torsal planes through the line $L(u,v)$.

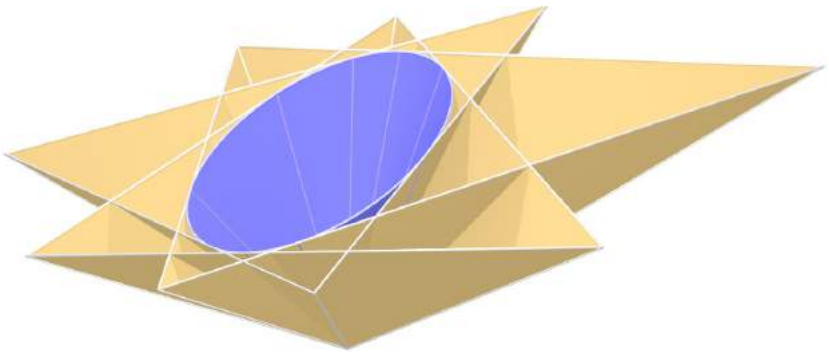

Figure 4.6: The "principal" trihedra mentioned in Proposition 4.2, when moved to the origin, lie tangent to a so-called *Monge cone*. Since these planes rotate about an entire cone as the interpolation parameter λ varies, one cannot without restrictions interpret these principal trihedra as tangent planes plus principal planes of an offset family of surfaces. Such an interpretation is valid only for small λ.

Conditions (4.6*), (4.7*) imply

$$\begin{aligned}
&\langle \mathbf{a}_j - \mathbf{a}_i, \bar{\mathbf{b}}_k - \bar{\mathbf{b}}_i \rangle - \langle \mathbf{a}_k - \mathbf{a}_i, \bar{\mathbf{b}}_j - \bar{\mathbf{b}}_i \rangle \\
&= \langle \mathbf{a}_j - \mathbf{a}_i, \mathbf{b}_k + \lambda_k \mathbf{n} - \mathbf{b}_i - \lambda_i \mathbf{n} \rangle - \langle \mathbf{a}_k - \mathbf{a}_i, \mathbf{b}_j + \lambda_j \mathbf{n} - \mathbf{b}_i - \lambda_i \mathbf{n} \rangle \\
&= \langle \mathbf{a}_j - \mathbf{a}_i, \mathbf{b}_k - \mathbf{b}_i \rangle - \langle \mathbf{a}_k - \mathbf{a}_i, \mathbf{b}_j - \mathbf{b}_i \rangle = 0,
\end{aligned}$$

i.e., symmetry of α and orthogonality of eigenvectors of α. This shows orthogonality of torsal planes and verifies the statement for the case $\lambda = 0$. The case $\lambda = 1$ is analogous, since condition (4.6*) is invariant if we replace $\mathbf{a}_i$ by $\mathbf{b}_i$ and vice versa. For all other values $\lambda \neq 1$ we note that replacing vertices $\mathbf{b}_i$ by vertices $\mathbf{a}_i + \lambda \mathbf{e}_i$ inflicts the change $\mathbf{e}_i \to \lambda \mathbf{e}_i$ without changing $\mathbf{a}_i$, which does not affect the normality condition (4.7*). □

As illustrated by Figure 4.2, congruences defined by the affine correspondence of triangles have counter-intuitive properties: The planes P_λ generated by linear interpolation of the defining triangles at the same time are the focal planes of $\mathcal{L}$ (and vice versa) since any P_λ carries the developable surface generated by the lines $\{P_\lambda \cap P_\alpha\}_{\alpha \in \mathbb{R}}$. The torsal planes P_λ are tangent to the focal surface F of $\mathcal{L}$. It is known that

F is the tangent surface of a cubic polynomial curve, cf. [51, Ex. 7.1.2]. Proposition 4.2 now tells us that this curve has infinitely many triples of mutually orthogonal tangent planes. Translating these planes (the principal trihedra) through the origin, they become tangent planes of the directing cone of F, which is a quadratic cone. This cone is quadratic and must likewise have infinitely many orthogonal circumscribed trihedra. It is therefore a so-called *Monge cone*, see Figure 4.6.

There is a phenomenon in geometry, called *porism*, cf. [81]. It refers to situations where existence of one object of a certain kind implies existence of an entire 1-parameter family of such objects. Monge cones are an instance of a porism: If a quadratic cone has one circumscribed orthogonal trihedron, then one can move this trihedron around the cone while it remains tangential. This fact is classical knowledge in projective geometry, see e.e. [82, pp. 33-34].

The same porism is hidden in the proof of Proposition 4.2: The normality condition (4.6*) was equivalent to existence of the principal trihedron associated with P_0, but it also implied existence of the trihedron for all P_λ.

4.2.3 Details on principal trihedra in discrete-normal congruences

We wish to interpret the three mutually orthogonal planes referred to by Proposition 4.2 as the tangent plane and principal planes of a surface. In particular the normal vector $\mathbf{n}_\lambda$ of P_λ shall be the normal vector, and the line N_λ shall be the surface normal, while the torsal planes should represent the principal directions. In order to understand better the behavior of the objects involved, we study the volumetric parametrization according to Equation (4.4) in an adapted coordinate system: the plane P_0 is the xy plane, and the two torsal planes associated with it shall be the xz and zy planes. Since the affine correspondence between planes P_0, P_1 may be defined by *any* pair of corresponding triangles, we choose $\mathbf{a}_1 = \mathbf{o}$, $\mathbf{a}_2 = (1, 0, 0)$, $\mathbf{a}_3 = (0, 1, 0)$. We may still change the plane P_1 without changing the congruence, so we choose

$\mathbf{b}_1 = (0,0,1)$. The vertices $\mathbf{b}_2, \mathbf{b}_3$ must lie in the xy and xz planes because of our assumption on the torsal planes. Thus we get

$$\mathbf{x}(u,v,\lambda) = \begin{pmatrix} u \\ v \\ 0 \end{pmatrix} + \lambda \begin{pmatrix} -\kappa_1 u \\ -\kappa_2 v \\ au + bv + 1 \end{pmatrix} \tag{4.8}$$

$$\implies \mathbf{n}_\lambda = \frac{\partial \mathbf{x}}{\partial u} \times \frac{\partial \mathbf{x}}{\partial v} = \begin{pmatrix} a\lambda(\kappa_2\lambda - 1) \\ b\lambda(\kappa_1\lambda - 1) \\ (\kappa_1\lambda - 1)(\kappa_2\lambda - 1) \end{pmatrix}.$$

We will later interpret κ_1, κ_2 as principal curvatures and vectors $(1,0,0)$ and $(0,1,0)$ as principal directions. Obviously, they are eigenvectors of the linear map α which occurs in the proof of Proposition 4.2. The plane P_λ is given as

$$\begin{aligned} n_{1,\lambda}x_1 + n_{2,\lambda}x_2 + n_{3,\lambda}x_3 - n_{0,\lambda} &= a\lambda(\kappa_2\lambda - 1)x_1 + b\lambda(\kappa_1\lambda - 1)x_2 \\ &+ (\kappa_1\lambda - 1)(\kappa_2\lambda - 1)x_3 - \lambda(\kappa_1\lambda - 1)(\kappa_2\lambda - 1) = 0. \end{aligned}$$

This is a cubic family of planes. Translating them through the origin yields the planes $n_{1,\lambda}x_1 + n_{2,\lambda}x_2 + n_{3,\lambda}x_3 = 0$, which are tangent planes of the tangent cone illustrated in Figure 4.6. Since the plane coefficients satisfy the quadratic equation $(\kappa_1 - \kappa_2)n_1n_2 - an_2n_3 + bn_1n_3 = 0$, it is indeed a quadratic cone.[1]

We now look for a line $L(u_\lambda, v_\lambda)$ orthogonal to P_λ. The direction of $L(u,v)$ can

[1]The vector of coefficients (n_1, n_2, n_3) of the equation of a plane is a normal vector of that plane. This shows that the orthogonal polar cone of the Monge cone fulfills the equation $(\kappa_1 - \kappa_2)x_1x_2 - ax_2x_3 + bx_1x_3 = 0$. Since the Monge cone had many circumscribed orthogonal trihedra, its polar cone has many inscribed orthogonal frames. These frames are generated by translating the frames seen in Figure 4.7b through the origin.

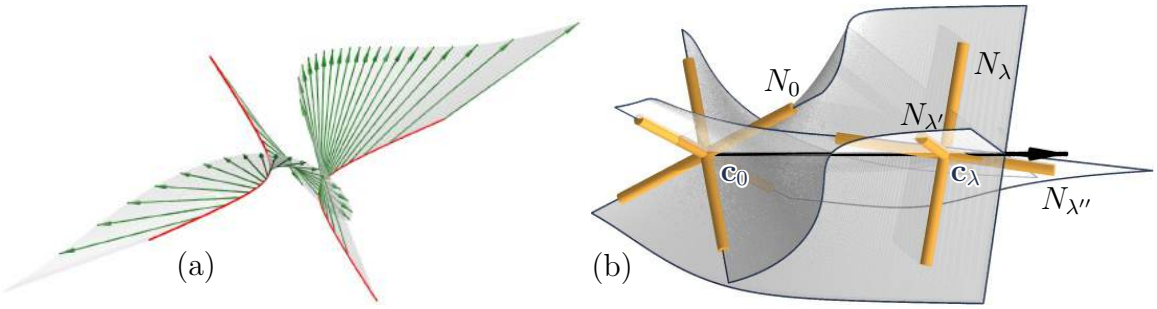

Figure 4.7: Behaviour of the principal trihedron and the normal N_λ of planes P_λ in a congruence defined by the affine correspondence between two triangles. (a) The normals N_λ (green) intersect the plane P_0 in the points $\mathbf{c}(u_\lambda, v_\lambda, 0)$ of a conic (red). (b) As λ changes, the apex $\mathbf{c}_\lambda = \mathbf{x}(u_\lambda, v_\lambda, \lambda)$ of the principal trihedron (yellow) moves along a straight line (blue). The ruled surfaces traced out by the edges of the trihedron are shown; their union forms one algebraic ruled surface of degree four.

be read off (4.8), so the condition $L(u_\lambda, v_\lambda) \parallel \mathbf{n}_\lambda$ reads

$$\begin{aligned} &\frac{\kappa_1 u_\lambda}{\kappa_2 v_\lambda} = \frac{a(\kappa_2\lambda - 1)}{b(\kappa_1\lambda - 1)}, \quad \frac{\kappa_1 u_\lambda}{a u_\lambda + b v_\lambda + 1} = \frac{a\lambda}{1 - \kappa_1\lambda} \\ &\implies u_\lambda = \frac{a\lambda\kappa_2(1 - \kappa_2\lambda)}{\nu_\lambda}, \quad v_\lambda = \frac{b\lambda\kappa_1(1 - \kappa_1\lambda)}{\nu_\lambda}, \\ &\text{where} \quad \nu_\lambda = \kappa_1\kappa_2(\kappa_1\lambda - 1)(\kappa_2\lambda - 1) + a^2\kappa_2\lambda(\kappa_2\lambda - 1) + b^2\kappa_1\lambda(\kappa_1\lambda - 1). \end{aligned} \tag{4.9}$$

In particular we see that the curve $\mathbf{x}(u_\lambda, v_\lambda, 0)$, consisting of all points $N_\lambda \cap P_0$, is a conic. In fact, for every α, the curve $\{N_\lambda \cap P_\alpha\}_{\lambda\in\mathbb{R}}$ is a conic it corresponds to the curve $N_\lambda \cap P_0$ under the affine mapping $\phi_{0\alpha} : \mathbf{x}(u, v, 0) \mapsto (u, v, \alpha)$, see Figure 4.7a. The surface of all N_λ's is then algebraic of degree four.

Let us now compute the "apex" $\mathbf{c}_\lambda = N_\lambda \cap P_\lambda = \mathbf{x}(u_\lambda, v_\lambda, \lambda)$ of the principal trihedron: From

$$\mathbf{c}_\lambda = \frac{\lambda(1 - \kappa_1\lambda)(1 - \kappa_2\lambda)}{\nu_\lambda} \begin{pmatrix} \kappa_2 a \\ \kappa_1 b \\ \kappa_1\kappa_2 \end{pmatrix} \tag{4.10}$$

we see that $\mathbf{c}_\lambda$ moves on a straight line, but the parametrization of this line is cubic.

Since the planes P_λ and the torsal planes stem from the same 1-parameter family of planes, any torsal plane will play the role of $P_{\lambda'}$ for another value λ'; in total each orthogonal trihedron will occur three times, and each of the three edges of the trihedron will play the role of N_λ three times (see Figure 4.7b). We summarize:

Proposition 4.3 If a congruence is defined by the affine correspondence between two triangles $\mathbf{a}_1\mathbf{a}_2\mathbf{a}_3$ and $\mathbf{b}_1\mathbf{b}_2\mathbf{b}_3$ and satisfies the normality condition (4.6*), then its focal surface has a 1-parameter family of circumscribed 'principal' orthogonal trihedra whose apex moves on a straight line and whose edges form an algebraic surface of degree 4 which contains that line as a triple line.

The complicated geometry of these congruences reflects the difficulties in defining offset pairs of triangle meshes.

4.2.4 Discrete normal congruences – Version 3

The identity

$$\begin{aligned}&\langle \mathbf{a}_j - \mathbf{a}_i, \mathbf{e}_k - \mathbf{e}_i\rangle - \langle \mathbf{a}_k - \mathbf{a}_i, \mathbf{e}_j - \mathbf{e}_i\rangle \\ =&\langle \mathbf{a}_i - \mathbf{a}_j, \mathbf{e}_i + \mathbf{e}_j\rangle + \langle \mathbf{a}_k - \mathbf{a}_i, \mathbf{e}_k + \mathbf{e}_i\rangle + \langle \mathbf{a}_j - \mathbf{a}_k, \mathbf{e}_j + \mathbf{e}_k\rangle,\end{aligned} \tag{4.11}$$

shows that either of the two conditions (4.6*), (4.7*) is implied by the stronger condition

$$\langle \mathbf{a}_j - \mathbf{a}_i, \mathbf{e}_j + \mathbf{e}_i\rangle = 0, \tag{4.12}$$

when imposed on all three edges of a triangle. This third version of normality is a more direct expression of the orthogonality between triangle mesh and congruence: the edges $\mathbf{a}_i\mathbf{a}_j$ of the mesh are required to be orthogonal to the arithmetic mean of normal vectors $\mathbf{e}_i, \mathbf{e}_j$ at either endpoint of the edge.

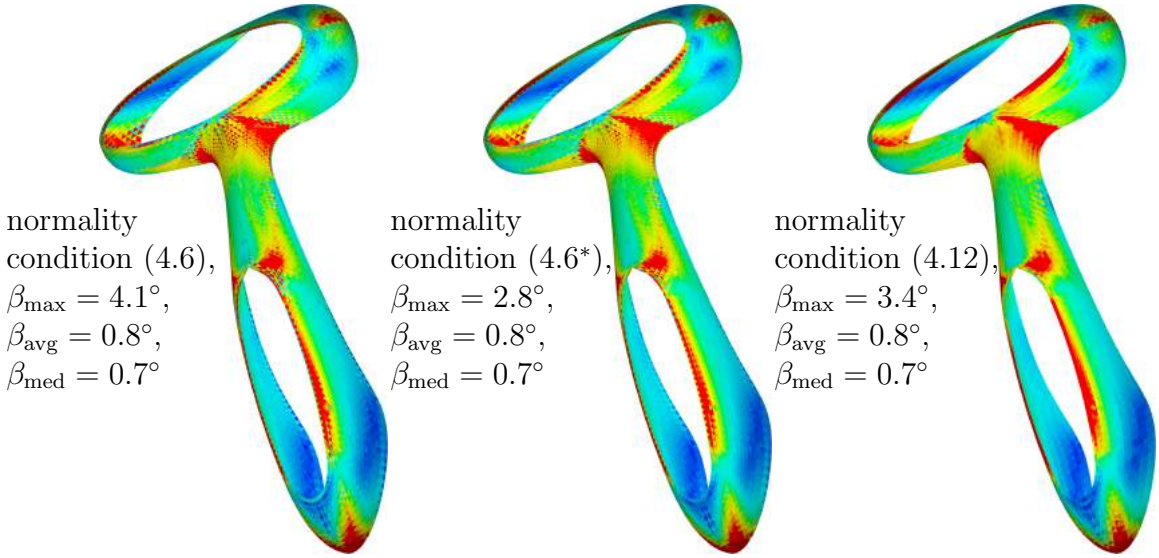

Figure 4.8: Optimization of normal congruences. For a given mesh with vertices $\mathbf{a}_i$, a discrete-normal congruence, defined by unit vectors $\mathbf{e}_i$, has been found by global optimization such that one of the normality conditions considered here is fulfilled. Each of these conditions is linear, so optimization was done by least squares. It turns out that there is no substantial difference between Equations (4.6*) and Equations (4.12). Faces are colored according to the angle β enclosed between the congruence line at the barycenter and the face's normal there. We also give statistics on β for each figure.

4.2.5 Comparison of definitions

The various definitions of discrete normal congruences have different advantages. When one wants to design a normal congruence (as in Wang et al. [36]), version 1 may be better because it ensures orthogonality of focal planes in the part of the line congruence which is actually realized. Using version 2, orthogonal focal planes may occur outside the realized part. On the other hand, when using the normal congruence of a given surface, version 2 has the advantage that one plane of a principal frame contains the base mesh triangle; moreover discrete principal directions are orthogonal and lie in the plane of the triangle. Version 3 normality is not used here except for Figure 4.8 where we show that imposing version 3 normality leads to results comparable to version 2. Since the weaker condition of version 2 is sufficient to achieve the same results, it is not necessary to impose version 3 normality.

4.3 Curvatures of faces of triangle meshes

Recall that a smooth normal congruence $\mathcal{L}$ possesses a surface A orthogonal to the lines of $\mathcal{L}$. Then automatically all offsets A^t also lie orthgonal to $\mathcal{L}$. We assume labeling of offsets such that surfaces A^t, A^s are at constant distance $|t-s|$ from each other. Then corresponding infinitesimal surface area elements "$dA^t(u,v)$" obey Steiner's formula

$$\frac{dA^t(u,v)}{dA^0(u,v)} = 1 - 2tH(u,v) + t^2K(u,v), \tag{4.13}$$

where H and K denote mean and Gaussian curvature of the surface A^0, respectively. The sign of H depends on the unit normal vector field; in our case the unit normal vector field points from A^0 to the surfaces A^t with $t > 0$.

We now return to a discrete congruence $\mathcal{L}$ defined by the piecewise-linear correspondence between triangle meshes A, B. Assuming A, B approximate an offset pair of surfaces at distance 1, we consider corresponding faces $\mathbf{a}_1\mathbf{a}_2\mathbf{a}_3$ and $\mathbf{b}_1\mathbf{b}_2\mathbf{b}_3$. We write $\mathbf{b}_i = \mathbf{a}_i + \mathbf{e}_i$, where the vectors $\mathbf{e}_i$ approximate unit normal vectors of the mesh A. An offset mesh at distance approximately t then has vertices and faces

$$\mathbf{a}_i^t = \mathbf{a}_i + t\mathbf{e}_i \quad \Delta^t = \mathbf{a}_1^t\mathbf{a}_2^t\mathbf{a}_3^t.$$

We further assume that the congruence $\mathcal{L}$ is a normal congruence (which we have defined in two different ways).

- If $\mathcal{L}$ is normal in the sense of Equations (4.6) and (4.7), then we apply the projection mentioned in Proposition 4.1, resulting in vertices $\bar{\mathbf{a}}_1\bar{\mathbf{a}}_2\bar{\mathbf{a}}_3$, $\bar{\mathbf{b}}_1\bar{\mathbf{b}}_2\bar{\mathbf{b}}_3$. The projection is in the direction of a certain unit vector $\mathbf{n}$.

- As an alternative, the congruence may be normal in the sense of Equations (4.6*), (4.7*). Here we consider orthogonal projection onto the plane P_0 which

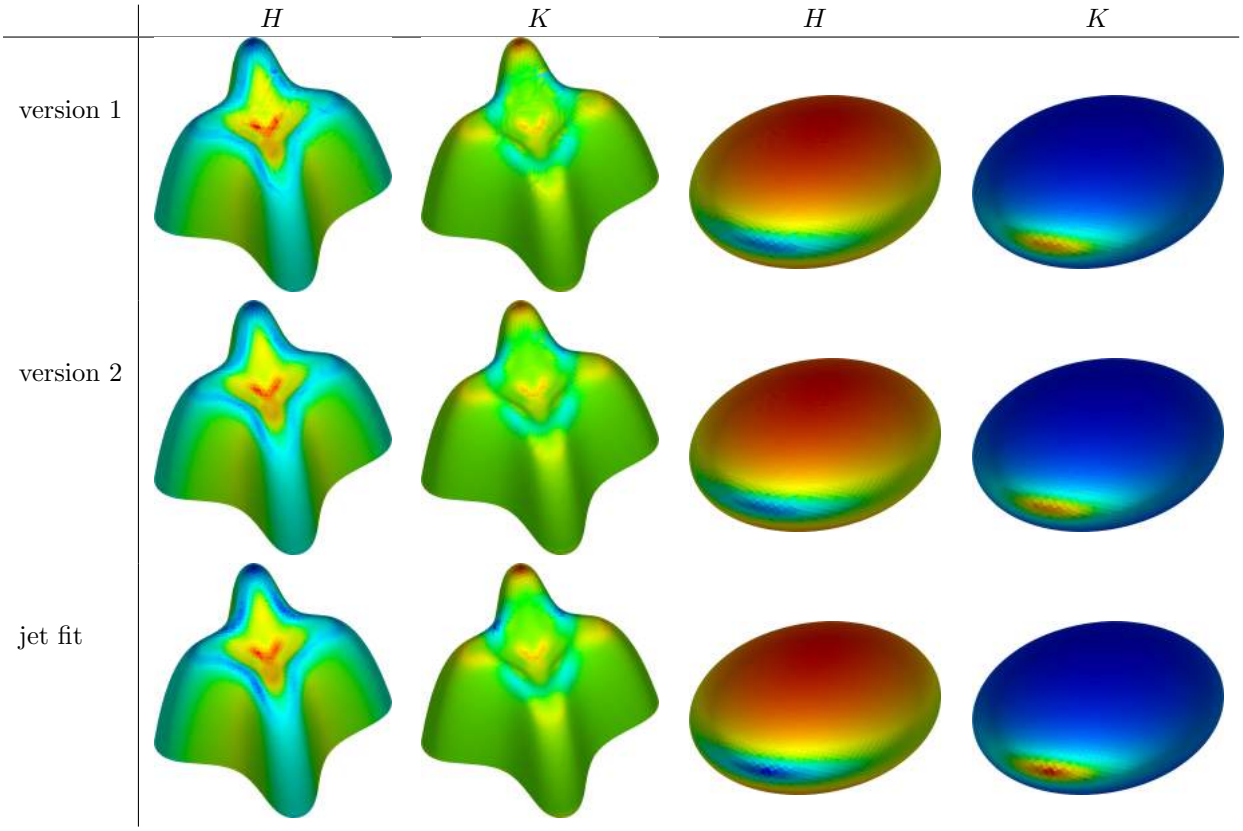

Figure 4.9: Computing mean curvature H and Gaussian curvature K by means of normal congruences: "version 1" and "version 2" refer to normality defined by Equations (4.6) and (4.6*), respectively. Estimated normals are optimized so as to become a normal congruence which allows us to compute curvatures in faces. For comparison, curvatures computed by a 3rd order jet fit have been used, cf. [54]. The color scale is the same for each kind of curvature and each model, throughout the 3 methods of computation. One can hardly see any difference. For each mesh, normal congruences have been computed in the way employed for Figure 4.8.

contains $\mathbf{a}_1\mathbf{a}_2\mathbf{a}_3$. This projection results in vertices $\bar{\mathbf{a}}_i = \mathbf{a}_i$ and $\bar{\mathbf{b}}_i$. The projection is in direction of the unit normal vector $\mathbf{n} = \mathbf{n}_0$ of the plane P_0.

We now study the behaviour of the area of the face Δ^t as t changes. We do not measure the actual area, but apply the projection just mentioned. The area of projected triangles is measured via a determinant in the plane:

$$\text{p-area}(\mathbf{x}_1\mathbf{x}_2\mathbf{x}_3) = \frac{1}{2}[\bar{\mathbf{x}}_2 - \bar{\mathbf{x}}_1, \bar{\mathbf{x}}_3 - \bar{\mathbf{x}}_1] = \frac{1}{2}[\mathbf{n}, \bar{\mathbf{x}}_2 - \bar{\mathbf{x}}_1, \bar{\mathbf{x}}_3 - \bar{\mathbf{x}}_1] = \frac{1}{2}[\mathbf{n}, \mathbf{x}_2 - \mathbf{x}_1, \mathbf{x}_3 - \mathbf{x}_1]$$

With the notation $\bar{\mathbf{a}}_{ij} = \bar{\mathbf{a}}_i - \bar{\mathbf{a}}_j$, $\bar{\mathbf{b}}_{ij} = \bar{\mathbf{b}}_i - \bar{\mathbf{b}}_j$, $\bar{\mathbf{e}}_{ij} = \bar{\mathbf{b}}_{ij} - \bar{\mathbf{a}}_{ij}$ we get

$$\frac{\text{p-area}(\triangle^t)}{\text{p-area}(\triangle^0)} = \frac{\frac{1}{2}[\bar{\mathbf{a}}_{12} + t\bar{\mathbf{e}}_{12}, \bar{\mathbf{a}}_{13} + t\bar{\mathbf{e}}_{13}]}{\frac{1}{2}[\bar{\mathbf{a}}_{12}, \bar{\mathbf{a}}_{13}]} = 1 + t\frac{[\bar{\mathbf{a}}_{12}, \bar{\mathbf{e}}_{13}] + [\bar{\mathbf{e}}_{12}, \bar{\mathbf{a}}_{13}]}{[\bar{\mathbf{a}}_{12}, \bar{\mathbf{a}}_{13}]} + t^2\frac{[\bar{\mathbf{e}}_{12}, \bar{\mathbf{e}}_{13}]}{[\bar{\mathbf{a}}_{12}, \bar{\mathbf{a}}_{13}]}.$$

4.3.1 Discrete curvatures and shape operator

The obvious similarity of this relation with (4.13) immediately leads to a definition of the mean curvature H and the Gauss curvature K of the face $\mathbf{a}_1\mathbf{a}_2\mathbf{a}_3$ under consideration:

$$K = \frac{[\mathbf{n}, \mathbf{e}_{12}, \mathbf{e}_{13}]}{[\mathbf{n}, \mathbf{a}_{12}, \mathbf{a}_{13}]}, \qquad 2H = -\frac{[\mathbf{n}, \mathbf{a}_{12}, \mathbf{e}_{13}] + [\mathbf{e}_{12}, \mathbf{a}_{13}]}{[\mathbf{n}, \mathbf{a}_{12}, \mathbf{a}_{13}]}. \tag{4.14}$$

Principal curvatures κ_1, κ_2 are defined by the relations

$$\kappa_1 + \kappa_2 = 2H, \quad \kappa_1\kappa_2 = K.$$

Completing the analogy with the smooth case, we define a shape operator Λ as the linear mapping which maps

$$\bar{\mathbf{a}}_i - \bar{\mathbf{a}}_j \overset{\Lambda}{\longmapsto} -(\bar{\mathbf{e}}_i - \bar{\mathbf{e}}_j), \quad \text{for all } i, j \in \{1, 2, 3\}.$$

Recall that the bar indicates projection (which in turn depends on which version of "normality" we employ). In analogy to the smooth case, principal directions are given by the focal planes of the congruence $\mathcal{L}$. All these notions fit together:

Proposition 4.4 The eigenvalues of the shape operator Λ are the principal curvatures κ_1, κ_2, and its trace and determinant are given by $2H$ and K, respectively. Eigenvectors of Λ indicate the principal directions.

Proof. Proof. We first show the statement for 'version 2' normality. Recall the linear

mapping α in the proof of Proposition 4.2 which maps $\bar{\mathbf{a}}_i - \bar{\mathbf{a}}_j \overset{\alpha}{\longmapsto} (\bar{\mathbf{a}}_i + \bar{\mathbf{e}}_i) - (\bar{\mathbf{a}}_j + \bar{\mathbf{e}}_j)$. Since by construction, $\Lambda = \mathrm{id} - \alpha$, Λ has the same eigenvectors as α, i.e., the torsal directions. The statement about $\operatorname{tr}\Lambda$ and $\det\Lambda$ follows from the relations $\det\Lambda = \frac{\det(\Lambda(\mathbf{x}),\Lambda(\mathbf{y}))}{\det(\mathbf{x},\mathbf{y})}$ and $\operatorname{tr}\Lambda = \frac{\det(\Lambda(\mathbf{x}),\mathbf{y})+\det(\mathbf{x},\Lambda(\mathbf{y}))}{\det(\mathbf{x},\mathbf{y})}$ which generally hold for linear mappings of $\mathbb{R}^2$. The statement about eigenvalues follows immediately.

For version 1 normality the proof is the same, only the bars have a different meaning. The mapping α is also referred to in the proof of Proposition 4.1 in [36]. □

Since we have defined principal curvatures κ_1, κ_2 implicitly via mean curvature H and Gauss curvature K, their relation to focal geometry is still unclear. In the smooth case, points at distance $1/\kappa_i$ from the surface are focal points of the normal congruence. This property holds in the discrete case too, if we use version 2 normality:

Proposition 4.5 Consider a congruence with parametric representation $\mathbf{x}(u, v, \lambda)$ which is defined by the correspondence of two triangles $\mathbf{a}_1\mathbf{a}_2\mathbf{a}_3$ and $\mathbf{b}_1\mathbf{b}_2\mathbf{b}_3$. Assume that it is normal in the sense of Equation (4.6*), and consider (in the notation of Proposition 4.2) the plane P_0 which contains $\mathbf{a}_1\mathbf{a}_2\mathbf{a}_3$ and the corresponding normal $L(u_0, v_0)$. Then the focal points of that line lie at distance $1/\kappa_1$, $1/\kappa_2$ from the plane P_0, with κ_i as the principal curvatures, i.e., the focal points are precisely the points $\mathbf{x}(u_0, v_0, 1/\kappa_i)$.

Proof. We consider the parametrization (4.8) which is with respect to an adapted coordinate system, so that $u_0 = 0$ and $v_0 = 0$. It is easy to see that the values κ_1, κ_2 ocurring there are indeed the principal curvatures. A simple computation shows that for the special case $u = v = 0$, the determinant of partial derivatives of $\mathbf{x}(u, v, \lambda)$ specializes to $[\mathbf{x}_u, \mathbf{x}_v, \mathbf{x}_\lambda] = (1 - \lambda\kappa_1)(1 - \lambda\kappa_2)$. Thus we have a singularity if $\lambda = 1/\kappa_i$. □

4.3.2 Special cases

An *umbilic* point is characterized by equality of principal curvatures, i.e., $\kappa_1 = \kappa_2 = \kappa$. In this case some of the geometric objects discussed above simplify. E.g. the above-mentioned cubic family of planes becomes the set of tangent planes of a quadratic cone with vertex $(0, 0, 1/\kappa)$. Such an umbilic occurs every time two corresponding triangles $\mathbf{a}_1\mathbf{a}_2\mathbf{a}_3$ and $\mathbf{b}_1\mathbf{b}_2\mathbf{b}_3$ are in homothetic position, but the converse is not true.

A *parabolic* point is characterized by one principal curvature, say κ_1, being zero. In this case, Equation (4.8) immediately shows that the congruence vectors $\mathbf{e}_1, \mathbf{e}_2, \mathbf{e}_3$ associated with vertices $\mathbf{a}_1, \mathbf{a}_2, \mathbf{a}_3$ are not linearly independent, so Proposition 4.2 does not apply. Along the x axis, the lines of the congruence are parallel to each other, which is in accordance with the fact that the focal point $(0, 0, 1/\kappa_1)$ has moved to infinity. The above-mentioned cubic family of planes is quadratic (in fact, it is the family of tangent planes of a parabolic cylinder).

Remark 4.1 We should mention that the approach to curvatures presented here carries over to *relative* differential geometry where the image of the Gauss map is not a sphere but a general convex body [83]. Another straightforward extension is to curvatures at vertices, which however does not lead to a shape operator in such a natural manner.

4.4 Results and discussion

4.4.1 Numerical examples

Vertex normals of a mesh can be estimated (e.g. as area-weighted averages of face normals). Any such collection of sensible normals is not far away from being a "normal" congruence in our sense. By applying optimization, we can make it as normal as possible, meaning that (4.6) is fulfilled in the least-squares sense. Numerical experiments show that this improves the quality of the normal field (even if there are not enough d.o.f. to satisfy (4.6) fully if the vertices of the mesh are kept fixed). Since

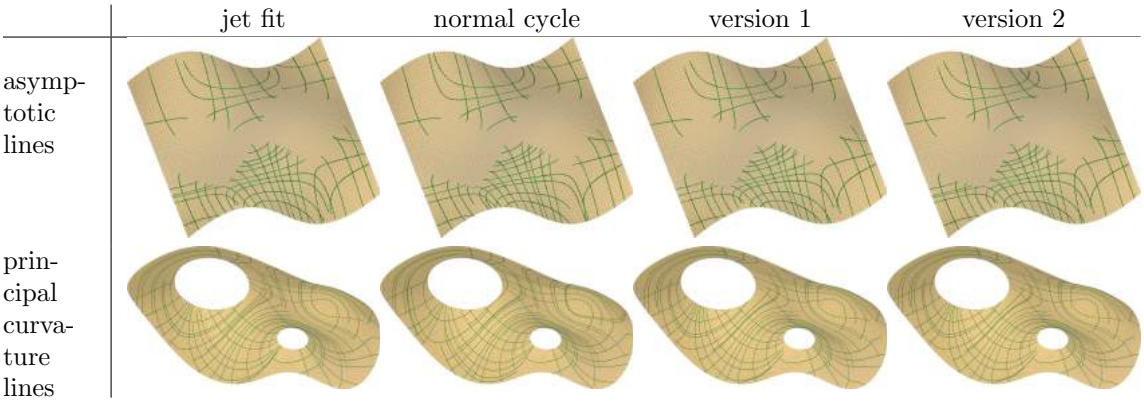

Figure 4.10: We compute asymptotic lines and principal curvature lines of meshs by various means. For the figures of the first column, we have used the 3rd order jet fit method of [54]. For the second column, we used the method of normal cycles (see [84] and next chapter). The 3rd and 4th column are computed using our the shape operators, where version 1 and version 2 refer to normality w.r.t. Equation (4.6) or Equation (4.6*), respectively. In both cases the normal congruence needed for defining the shape operator was obtained in the same way as for Figure 4.8. The almost identical figures of the asymptotic lines and principal curvature lines according to the four methods shows that all of these approaches are effective in computing curvature directions. The jet fit method is an approximation, whereas the version 1 & 2 method, as well as the normal cycle method (which will be discussed in the next chapter) are curvature theories.

curvatures and the distribution of normals are inseparable, it makes sense to study curvatures not only as quantities derived from a mesh, but as quantities which arise naturally from the the result of the optimization procedure just mentioned. In this way the natural sensitivity of curvatures with respect to noise is moderated.

The basic task is, of course, the computation of a normal congruence for a given mesh. This is done via a standard optimization procedure, which is initialized from estimated vertex normals. We express the validity of the normality condition in terms of least squares, and minimize subject to the constraints that (in the terminology of previous sections), vectors $\mathbf{e}_i$ are of unit length. Figure 4.8 shows an example. In particular one can see that normality according to Equation (4.6) ("version 1") behaves differently from normality according to Equation (4.6*) ("version 2"), while there is hardly any difference between conditions (4.6*) and (4.12).

Degrees of freedom and topology. When optimizing a normal congruence of a mesh with v vertices, e edges and f faces, we count $3v$ variables for the normals and $f+v$ constraints. If a number b of boundary vertices is present, we fix the normals at the boundary, resulting in $3(v-b)$ variables and $f+(v-b)$ constraints, i.e., $2v-f-2b$ d.o.f. Elementary manipulations show that

$$\text{d.o.f.} = 2\chi - b,$$

with $\chi = f+v-e$ as the Euler characteristic. We see for meshes of sphere topology we can expect a unique solution, but topological features diminish the available degrees of freedom. If boundary normals are kept fixed, long boundaries diminish this freedom even more. By allowing vertices to move during optimization, we can achieve zero residual again, but of course a compromise has to be found between the quality of the normal congruence and the deviation of the mesh from its previous shape. Table 4.1 shows some numerical experiments.

	sphere		torus				disk w/ holes, see Fig. 4.10			
	fixed vertices		fixed vertices		moving vertices		fixed vertices		moving vertices	
	c	n	c	n	c	n	c	n	c	n
v.1	$7.8{\cdot}10^{-3}$	0	$7.7{\cdot}10^{\ 0}$	0	–	–	$1.5{\cdot}10^{\ 0}$	0	–	–
v.2	$9.7{\cdot}10^{-5}$	0	$9.6{\cdot}10^{-1}$	0	$6.9{\cdot}10^{-5}$	$8.1{\cdot}10^{-7}$	$1.9{\cdot}10^{-2}$	0	$4.0{\cdot}10^{-5}$	$2.2{\cdot}10^{-9}$
v.3	$9.0{\cdot}10^{-2}$	0	$1.3{\cdot}10^{-1}$	0	$6.9{\cdot}10^{-4}$	$6.3{\cdot}10^{-4}$	$2.4{\cdot}10^{-1}$	0	$9.6{\cdot}10^{-5}$	$9.5{\cdot}10^{-10}$

Table 4.1: Comparison of residuals regarding normalcy of the congruence ("c") and unit vectors being normalized ("n") when optimizing congruences. All meshes are normalized for unit average edge length, and a zero means a zero up to machine precision. The rows in this table correspond to versions 1, 2, 3 of the normalcy condition for congruences. One can see that zero residual happens only for sphere topology.

Computing Curvatures. Once a normal congruence is availabe, we can compute curvatures (see Figure 4.9) and we can integrate the field of principal curvature directions as well as the field of asymptotic directions (see Figure 4.10 for an example). It must be said, however, that we do not want to compete with the many other methods for

computing curvatures, and we do not regard the ability to compute curvatures a main result of this study.

Robustness by using normals. Figure 4.11 demonstrates that considering a mesh and its normal congruence *together* allows us to handle optimization/smoothing in a stable way. After a mesh and its normals have been perturbed (Figure 4.11b), an optimization procedure attempts to restore both. We use a target functional composed of a sum of least squares expressing condition (4.6*) and also the property of vectors $\mathbf{e}_i$ having length 1 (weight 1), proximity to the input data (weight 1/4), Laplacian fairing for the mesh (weight 10^{-6}), Laplacian fairing for the normal vectors (weight 10^{-4}) and comptabibility between normal and mesh by penalizing deviation from orthogonality between congruence lines in mesh barycenters and face (weight 10^{-4}). Figure 4.11c shows the repaired mesh.

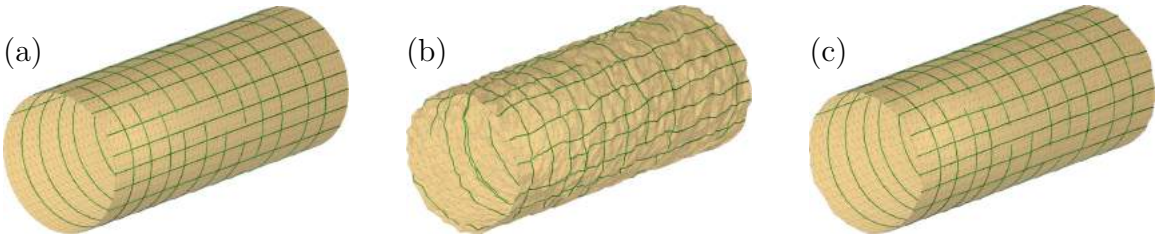

Figure 4.11: Computing normals and principal curvature lines for noisy data. Subfigure (a) shows a triangulated cylinder and some of its principal curvature lines. In (b) the jet fit method has been used to obtain principal curves for data where noise has been added to both vertex coordinates and normals. Subfigure (c) shows the result of optimization applied to (b), which results in a smooth mesh equpped with a normal congruence. For (c) we again show the principal curvature lines computed by our method.

4.4.2 Relevance for discrete differential geometry.

The idea of employing the Steiner formula for defining curvatures has proved very helpful in bringing together various different notions of curvature, and indeed, various different notions of discrete surfaces (like discrete minimal surfaces and discrete cmc surfaces) which were defined in a way not involving curvature directly but by

other means like Christoffel duality. We refer to [25] and [12] for more details. The theory presented in [25] is restricted to offset-like pairs of polyhedral surfaces where corresponding edges and faces are parallel. There are ongoing efforts to extend this theory to more general situations (we point to recent work on quad meshes [85] and on isothermic triangle meshes of constant mean curvature [86]). It is therefore remarkable that at least for the situation described here, triangle meshes allow an approach to curvatures and even a shape operator which is likewise guided by the Steiner formula, but without the rather restrictive property of parallelity (which for triangle meshes would be even more restrictive).

4.5 Applications to the shading systems

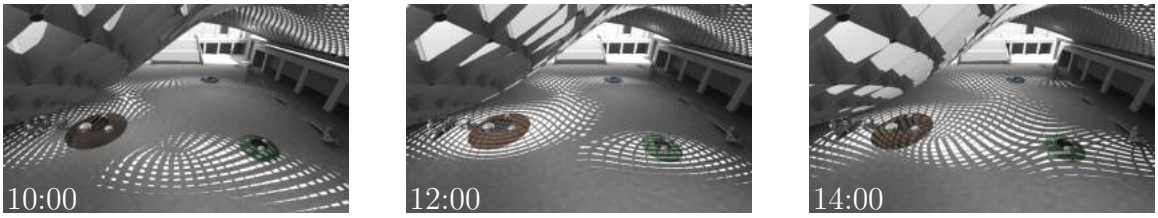

Figure 4.12: Selective Shading: Moving patterns generated by shading system optimized for blocking light at 12:00 except at designated areas. Figure from [36].

The applications of the line congruences to the shading systems are first demonstrated in [36]. Here we briefly review the one of the examples there. See Figure 4.12. This architectural design is to give shade except for a designated area where shading fins are to be parallel to incoming rays. Such design is based on the so-called *torsion-free support structures* [21, 36], which is a special case of the double-layer support structures [21]. The base mesh is realized as the inner-layer of the support structure and the line congruences across the edges are realized as its fins. The shading effects is obtained by adding additional constraints to the reflection of the light wave. Detail of the process can be found in [36].

Chapter 5

Asymptotic Cones of Embedded Singular Spaces

Some notation For details on the theory of smooth Riemannian submanifolds, the reader may consult for instance, [87] or [88]. We use the following notation. Let W^n be an n-dimensional closed (oriented) smooth submanifold embedded in a smooth N-dimensional (oriented) Riemannian manifold $(M^N, <.,.>)$. The manifold W^n inherits a Riemannian structure by pulling back $<.,.>$ by the embedding, which we still denote by $<.,.>$. We denote by $TW^n \stackrel{\pi_{W^n}}{\longrightarrow} W^n$ (*resp.* $TM^N \stackrel{\pi_{M^N}}{\longrightarrow} M^N$) the tangent bundle of W^n (*resp.* M^N) and $\Xi(W^n)$ (*resp.* $\Xi(M^N)$) the space of tangent vector fields over W^n (*resp.* M^N). We denote by $\tilde{\nabla}$ (*resp.* ∇) the Levi-Civita connection on $(M^N, <.,.>)$ (*resp.* W^n). We denote by $T^{\perp}W^n \stackrel{\pi_{W^n}}{\longrightarrow} W^n$ the normal bundle of the submanifold W^n. The *second fundamental form* of the submanifold W^n is the symmetric vector-valued $(2,0)$-tensor

$$h \ : TW^n \times TW^n \to T^{\perp}W^n$$

defined as follows:

$$\forall x \in TW^n, \forall y \in TW^n, h(x,y) = \tilde{\nabla}_x y - \nabla_x y.$$

Let m be a point of W^n. The isotropic cone

$$\mathbf{C}_m^{W^n} = \{x \in T_m W^n \ : h_m(x,x) = 0\} \tag{5.1}$$

of h_m is classically called the *asymptotic cone* of W^n at m. For any $\xi_m \in T_m^{\perp}W^n$, the eigenvalues of $< h_m(.,.), \xi_m >$ are the *principal curvatures* of W^n at m in the direction ξ_m.

5.1 The case of smooth surfaces in $\mathbb{E}^3$

We first restrict our attention to smooth closed (oriented) surfaces W^2 embedded in the (oriented) Euclidean space $(\mathbb{E}^3, < .,. >)$ bounding a domain D. Let ξ be the normal vector field compatible with these orientations. The second fundamental form of W^2 can now be identified with the tensor $< h(.,.), \xi >$ taking its values in $\mathcal{C}^\infty(W^2)$. We denote by $\lambda_{1_m}, \lambda_{2_m}$ the principal curvatures of W^2 at the point m, that is, the eigenvalues of h_m, by G the Gauss curvature of W^2, that is, the determinant of h and by H its mean curvature, that is, its trace (in an orthonormal frame). In a frame of principal vectors (e_{1_m}, e_{2_m}) at m (that is, eigenvectors of h_m) the matrix of h_m is

$$\begin{pmatrix} \lambda_{1_m} & 0 \\ 0 & \lambda_{2_m} \end{pmatrix}.$$

At each point $m \in W^2$ with negative Gauss curvature, the asymptotic cone $\mathbf{C}_m^{W^2}$ is the union of two lines. Integrating the corresponding vector fields gives rise to foliations of W^2 by the so-called *asymptotic curves*. By definition, at each point, the principal normal directions of these curves (considered as curves in $\mathbb{E}^3$) are tangent to W^2.

Using measure theory, the goal of this chapter is to define and study analogous cones associated with a (regular or) singular subspace of a Riemannian manifold M^N, lying above any Borel subset of M^N.

Let us begin by explaining how we define such cones over any Borel subset of $\mathbb{E}^3$ in the regular case; that is, when the subset is a (compact) domain bounded by a

smooth surface W^2. Let $T_{W^2}\mathbb{E}^3$ be the tangent bundle of $\mathbb{E}^3$ restricted to W^2. If x is any vector field on $T_{W^2}\mathbb{E}^3$, we build a signed measure $\Phi^x_{W^2}$ as follows: For any Borel subset B of $\mathbb{E}^3$, we write

$$\Phi^x_D(B) = \int_{B\cap W^2} h_m(pr_{T_mW^2}x, pr_{T_mW^2}x)dm, \tag{5.2}$$

where $pr_{T_mW^2}$ denotes the orthogonal projection on T_mW^2 and dm is the Lebesgue measure on $\mathbb{E}^3$. Let us now fix B and consider the map

$$x \mapsto \Phi^x_D(B), \tag{5.3}$$

where x runs over the (huge) space of vector fields $\Xi(\mathbb{E}^3)|_{W^2}$. This map is quadratic in x. If we force x to be a constant vector field, then we get a quadratic form (that we still denote by $\Phi^\bullet_D(B)$) on $\mathbb{E}^3$. This quadratic form has generically three eigenvalues, $\lambda_1(B), \lambda_2(B), \lambda_3(B)$, that we call the *principal curvatures* of B. The corresponding eigenvectors are called the *principal vectors* of B, and the matrix of $\Phi^\bullet_{W^2}(B)$ in this frame is

$$\begin{pmatrix} \lambda_1(B) & 0 & 0 \\ 0 & \lambda_2(B) & 0 \\ 0 & 0 & \lambda_3(B) \end{pmatrix}.$$

From this construction, we also introduce the *isotropic cone* associated with $\Phi^\bullet_D(B)$:

$$\mathcal{C}^{\mathrm{par},D}_B = \{x \in \mathbb{E}^3; \Phi^x_D(B) = 0\}, \tag{5.4}$$

(the notation coming from the fact that we restrict our isotropic cone to constant - that is, parallel - vector fields in $\mathbb{E}^3$). We call it the *asymptotic cone* of B (with respect to D).

To clarify that this construction is linked with the classical pointwise situation,

suppose that B is reduced to a point $\{m\} \in W^2$. If y is a constant vector field such that $y_m \in T_m W^2$, then

$$\Phi_D^y(\{m\}) = h_m(y_m, y_m). \tag{5.5}$$

If z is a constant vector field such that $z_m = \xi_m$, then

$$\Phi_D^z(\{m\}) = 0. \tag{5.6}$$

This implies that in the frame $(e_{1_m}, e_{2_m}, \xi_m)$, the matrix of $\Phi_D^\bullet(\{m\})$ is

$$\begin{pmatrix} \lambda_{1_m} & 0 & 0 \\ 0 & \lambda_{2_m} & 0 \\ 0 & 0 & 0 \end{pmatrix}. \tag{5.7}$$

Consequently, the asymptotic cone $\mathcal{C}_m^{\mathrm{par},D}$ is nothing but the cone spanned by the normal ξ_m and $\mathbf{C}_m^{W^2}$.

This construction has some advantages:

One can define the asymptotic cones at different scales by scaling the Borel sets (for instance, by taking balls of radius $\frac{1}{k}$ as Borel subsets).

Generically, we get three geometric invariants, $\lambda_1(B), \lambda_2(B), \lambda_3(B)$, instead of two, and a two-dimensional cone instead of the union of two lines.

Moreover, another important advantage of replacing functions by measures, is that this framework can be used for a large class of singular spaces (for instance, polyhedra, algebraic subsets, subanalytic subsets) of any codimension in any Riemannian manifold, as long as we can extend the notion of normal space. For instance, if one replaces the smooth surface by a polyhedron P bounding a domain $\mathcal{D}$, we will get the following explicit simple expression approximating the cone $\mathcal{C}_B^{\mathrm{par},\mathcal{D}}$ (see Equation (5.36), and also Equation (5.34) for the exact formulas) :

$$\Phi^x_{\mathcal{D}}(B) \sim \sum_{e\in\mathbf{E}} l(e\cap B)\angle(e) < x, e^- >^2,$$

and

$$\mathcal{C}^{\mathrm{par},\mathcal{D}}_B \sim \{x \in \mathbb{E}^3 : \sum_{e\in\mathbf{E}} l(e\cap B)\angle(e) < x, e^- >^2 = 0\},$$

(see Section 5.3 for the notation). This is why the theory of the normal cycle, extensively studied over the last decades [39, 40], will be our framework. In the following we describe the construction of asymptotic cones in such a large context.

5.2 Asymptotic forms

To be self contained, we begin with a summary of the geometry of the tangent bundle of an (oriented) N-dimensional smooth Riemannian manifold $(M^N, <.,.>)$. The reader may consult [89, 90, 38] for details. We denote by $TTM^N \overset{\pi_{TM^N}}{\to} TM^N$ the tangent bundle of the manifold TM^N. As usual, we consider the exact sequence of vector bundles:

$$0 \longrightarrow TM^N \times_{M^N} TM^N \overset{i}{\longrightarrow} TTM^N \overset{j}{\longrightarrow} TM^N \times_{M^N} TM^N \longrightarrow 0, \tag{5.8}$$

where i denotes the natural injection defined by

$$i(u_1, u_2) = \frac{d}{dt}(u_1 + tu_2)\Big|_{t=0} \tag{5.9}$$

and

$$j = (\pi_{TM^N}, d\pi_{M^N}). \tag{5.10}$$

The *vertical bundle* of M is the subbundle $V(M^N) = \ker j$ of TTM^N. The morphism i induces an isomorphism:

$$\bar{i} : TM^N \times_{M^N} TM^N \to V(M^N). \tag{5.11}$$

If $m \in M^N$ and $x \in T_mM^N$, the *vertical lift* of $z \in T_mM^N$ at x is the vector $z^v = i(x, z)$. The morphism $J = i \circ j$ is an almost tangent structure on M^N ($J^2 = 0$) and $V(M^N) = \ker J$. Let

$$\delta : TM^N \longrightarrow TM^N \times_{M^N} TM^N \tag{5.12}$$

be the canonical vector field defined by $\delta(x) = (x, x)$ and let $C : TM^N \longrightarrow V(M^N)$ be the vertical vector field associated with the (global) one-parameter group of homotheties with positive ratio, acting on the fibers of TM^N. We have $C = i \circ \delta$. We write $\eta = pr_2 \circ \bar{i}^{-1}$, where pr_2 denotes the projection on the second factor of $TM^N \times_{M^N} TM^N$. Since M^N is endowed with a Riemannian metric $< \cdot, \cdot >$ and its Levi-Civita connection, we can build the corresponding right splitting

$$\gamma : TM^N \times_{M^N} TM^N \longrightarrow TTM^N \tag{5.13}$$

of the exact sequence (5.8), (satisfying $j \circ \gamma = \mathrm{Id}_{TM^N \times_{M^N} TM^N}$). Let $m \in M^N$ and $x \in T_mM^N$. *The horizontal lift* of $z \in T_mM^N$ at x is the vector $z^h = \gamma(x, z)$. We denote $H_x(M^N) = \mathrm{Im}(\gamma(x, \cdot))$, from which we construct the horizontal bundle $H(M^N)$ such that, for all $x \in T_mM^N$

$$T_xTM^N = V_x(M^N) \oplus H_x(M^N). \tag{5.14}$$

We denote by $\mathcal{V}(M^N)$ (*resp.* $\mathcal{H}(M^N)$) the space of vertical (*resp.* horizontal) vector fields. We denote by $\mathtt{h} : TTM^N \longrightarrow H(M^N)$ the horizontal projection, and by $\mathtt{v} : TTM^N \longrightarrow V(M^N)$ the vertical projection. We remark that $\mathtt{h} = \gamma \circ j$. The morphism

$$K = \eta \circ \mathtt{v} : TTM^N \to TM^N$$

is the *connector* associated with the Levi-Civita connection. At every point $x \in T_mM^N$, the morphism

$$(d\pi_M \times K)_x : T_xTM \to T_mM^N \times T_mM^N$$

is an isomorphism that identifies $V_x(M^N)$ with T_mM^N and $H_x(M^N)$ with T_mM^N. The bundle $TTM^N \overset{\pi_{TM^N}}{\longrightarrow} TM^N$ is canonically endowed with the *Sasaki metric* $< \cdot, \cdot >$ defined by the following conditions:

$$\begin{cases} V(M^N) \text{ and } H(M^N) \text{ are orthogonal,} \\ i \text{ is an isometry,} \\ \gamma \text{ is an isometry.} \end{cases} \tag{5.15}$$

If

$$\alpha : M^N \to M^N \times M^N$$

is the diagonal map defined by $\alpha(m) = (m, m)$, then for every $x \in TM^N$,

$$(d\pi_M \times K)^{-1} \circ d\alpha(x) = x^v \oplus x^h.$$

Finally, the bundle $TTM^N \stackrel{\pi_{TM^N}}{\longrightarrow} TM^N$ is also endowed with an almost complex structure F ($F^2 = -\mathrm{Id}$), defined by the following conditions

$$\begin{cases} FJ = \mathtt{h} \\ F\mathtt{h} = -J. \end{cases} \tag{5.16}$$

Therefore $F|_V : V(M^N) \longrightarrow H(M^N)$ and $F|_H : H(M^N) \longrightarrow V(M^N)$ are isometries. In this Riemannian context, we give the following definition:

Definition 5.1

1. The vector valued $(N-1)$-form on TM^N defined for each $X \in \mathcal{H}(M^N)$ by

$$\mathbf{h}^X = [*_{\mathrm{Hodge}}(FC \wedge X)] \wedge FX \tag{5.17}$$

   is called the asymptotic $(N-1)$-form on TM^N.

2. The vector valued $(N-1)$-form on M^N defined for each $x \in \Xi(M^N)$ by

$$\mathbf{h}^x = [*_{\mathrm{Hodge}}(FC \wedge x^h)] \wedge x^v \tag{5.18}$$

   is called the asymptotic $(N-1)$-form on M^N.

In this definition, $*_{\mathrm{Hodge}}$ denotes the Hodge duality on $H_x(M^N)$ for each $x \in TM^N$. (The introduction of the Hodge operator in the definition of the generalized second fundamental form can be found in [91] when the ambient space is Euclidean. We adapt it here to the general Riemannian situation. It is equivalent to the initial definition given in [38]). Using the identification of vector fields and 1-forms induced by the Riemannian structure, $*_{\mathrm{Hodge}}(FC \wedge X)$ is a $(N-2)$-form on $\mathcal{H}(M^N)$. On the other hand, FX is (identified with) a 1-form, null on $H(M^N)$ and acting on $V(M^N)$, and $*_{\mathrm{Hodge}}(FC \wedge X)$ is (identified with) an $(N-2)$-form null on $V(M^N)$ and acting on $H(M^N)$.

5.3 Normal cycles, asymptotic measures, asymptotic cones

5.3.1 Currents and normal cycles of singular spaces

Let $\mathcal{D}_l(TM^N)$ be the space of *l-currents* of TM^N ($0 \leq l \leq 2N$); that is, the topological dual of the space $\mathcal{D}^l(TM^N)$ of *l-differential forms* with compact support on TM^N, endowed with the topology of uniform convergence on any compact subset, of all partial derivatives of any order. The duality bracket will be still denoted by $< \cdot, \cdot >$ if no confusion is possible. The space $\mathcal{D}_l(TM^N)$ is naturally endowed with the weak topology: if $(C_k)_{k\in\mathbb{N}}$ is a sequence of l-currents of TM^N and if C is a l-current of TM^N, then

$$\lim_{k\to\infty} C_k = C \Longleftrightarrow \forall \omega \in \mathcal{D}^l(TM^N), \lim_{k\to\infty} < C_k, \omega > = < C, \omega > . \tag{5.19}$$

An l-current is *rectifiable* if it is associated with a rectifiable subset (see [23] for details). An l-current is *integral* if it is rectifiable and its boundary is rectifiable.

When it exists, the *normal cycle* of a (compact singular) subset $\mathcal{W}$ of a Riemannian manifold M^N is a closed integral current $\mathbf{N}(\mathcal{W}) \in \mathcal{D}_{N-1}(TM^N)$, which is Legendrian for the symplectic structure on TM^N dual to the canonical one on T^*M^N in the duality defined by the metric. The normal cycle is the direct generalization of the unit normal bundle of a smooth submanifold. Its formal definition was given in [39]. Although the normal cycle cannot be defined on any compact subset of M^N, it exists for a large class of subsets, as convex subsets, polyhedra, subsets of positive reach, subanalytic subsets for instance. Following [39], any compact subset $\mathcal{G}$ of M^N such that $\mathbf{N}(\mathcal{G})$ exists is said to be *geometric*, and $\mathbf{N}(\mathcal{G})$ is called its normal cycle. One of the main properties of the normal cycle for our purpose is its additivity [39]:

Proposition 5.1 If $\mathcal{G}_1$ and $\mathcal{G}_2$ are geometric, then $\mathcal{G}_1 \cup \mathcal{G}_2$ and $\mathcal{G}_1 \cap \mathcal{G}_2$ are geometric

and

$$\mathbf{N}(\mathcal{G}_1 \cup \mathcal{G}_2) = \mathbf{N}(\mathcal{G}_1) + \mathbf{N}(\mathcal{G}_2) - \mathbf{N}(\mathcal{G}_1 \cap \mathcal{G}_2). \tag{5.20}$$

Here are some classical examples:

1. The normal cycle of a smooth submanifold of a Riemannian manifold is the closed current associated with its unit normal bundle.

2. If D is a compact domain whose boundary is a smooth hypersurface, then its normal cycle is the closed current associated with its outward unit normal vector field.

3. If C is a convex body, then its normal cycle is the closed current associated with the oriented set

$$\{(m, \xi) : m \in \partial C, \xi \in \mathbb{E}^3, ||\xi|| = 1, \forall z \in C, < \xi, \overrightarrow{mz} > \leq 0\}.$$

4. The normal cycle of a polyhedron of $\mathbb{E}^N$ can be computed by applying Equation (5.20) to a decomposition of the polyhedron into (convex) simplices and using 3.

5.3.2 Asymptotic measures, asymptotic cones

Let us now define an *asymptotic (signed) Radon measure* on M^N (*resp.* TM^N) associated with a geometric subset. We denote by $\mathcal{B}_{M^N}$ (*resp.* $\mathcal{B}_{TM^N}$) the class of Borel subsets of M^N (*resp.* TM^N) with compact closure.

Definition 5.2 Let $\mathcal{G}$ be a geometric subset of M^N.

1. The asymptotic measure defined on TM^N, associated with $\mathcal{G}$ and $X \in \mathcal{H}(M)$ is the map

$$\Phi_{\mathcal{G}}^X : \mathcal{B}_{TM^N} \longrightarrow \mathbb{R} \tag{5.21}$$

defined as follows:

$$\forall B \in \mathcal{B}_{TM^N}, \Phi^X_{\mathcal{G}}(B) =< \mathbf{N}(\mathcal{G}), \chi_B \mathbf{h}^X > . \tag{5.22}$$

2. The asymptotic measure defined on M^N, associated with $\mathcal{G}$ and $x \in \Xi(M^N)$ is the map $\Phi^x_{\mathcal{G}}$ defined as follows:

$$\forall B \in \mathcal{B}_{M^N}, \Phi^x_{\mathcal{G}}(B) =< \mathbf{N}(\mathcal{G}), \chi_{\pi^{-1}_M(B)} \mathbf{h}^x > . \tag{5.23}$$

If $\mathcal{G}$ and B are fixed, the map

$$x \to < \mathbf{N}(\mathcal{G}), \chi_{\pi^{-1}_M(B)} \mathbf{h}^x >$$

is quadratic, inducing its isotropic cone. This remark leads to the following definition:
Definition 5.3 Let $\mathcal{G}$ be a geometric subset of M^N. With any Borel subset $B \in \mathcal{B}_{M^N}$, we associate the cone

$$\mathcal{C}^{\mathcal{G}}_B = \{x \in \Xi(M^N) : \Phi^x_{\mathcal{G}}(B) = 0\} \tag{5.24}$$

and the cone

$$\mathcal{C}^{\mathrm{par},\mathcal{G}}_B = \{x \in \Xi(M^N) : x \text{ parallel}, \Phi^x_{\mathcal{G}}(B) = 0\}, \tag{5.25}$$

which we call the asymptotic cones associated with B.

In many applications, and for simplicity, it is easier to consider the cone of *parallel* vector fields, identifying a parallel vector field with its value at any point $m \in B$. Obviously, $\mathcal{C}^{\mathrm{par},\mathcal{G}}_B \subset \mathcal{C}^{\mathcal{G}}_B$. We remark, however, that this new definition can be quite restrictive depending on the geometry of M^N. For instance, if M^N has non-zero constant sectional curvature, the only parallel vector field is the null vector field. In contrast, if $M^N = \mathbb{E}^N$, the space of parallel vector fields is the space of constant vector fields, which can be identified with $\mathbb{E}^N$, which is much easier to manipulate.

We deduce easily from (5.23) explicit expressions of these curvature measures in some particular cases.

The case of smooth submanifolds. Let W^n be a (compact smooth) submanifold (with or without a boundary) embedded in M^N and $X \in \mathcal{H}(TM^N)$. Since the normal cycle of a smooth submanifold is its unit normal bundle, we deduce from [38] or [23] (Corollary 16 page 215) that for any $B \in \mathcal{B}_{TM^N}$,

$$\Phi^X_{W^n}(B) = \int_{ST^\perp W^n \cap B} h^\xi(\mathrm{pr}_{TW^n} d\pi_M(X), \mathrm{pr}_{TW^n} d\pi_M(X)) d\xi dv, \tag{5.26}$$

where h^ξ denotes the second fundamental form of W^n in the direction of the unit vector ξ, $ST^\perp W^n$ denotes the unit normal bundle of W^n and pr_{TW^n} denotes the orthogonal projection onto the tangent bundle TW^n. In particular, let W^{N-1} be a (smooth oriented) hypersurface of M^N bounding a domain D. (This assumption is not restrictive in our case, since our results are local. It allows to simplify some technical points by considering "only one side" of the normal cycles (the one corresponding to the outward unit normals). we have, for any B in $\mathcal{B}_{M^N}$,

$$\Phi^X_D(B) = \int_{W^{N-1} \cap B} h(\mathrm{pr}_{TW^{N-1}} d\pi_M(X), \mathrm{pr}_{TW^{N-1}} d\pi_M(X)) dv, \tag{5.27}$$

where ξ is the outward (with respect to D) unit normal vector field of W^{N-1}, and h is the second fundamental form of W^{N-1} in the direction ξ. We have then a correct generalization of Equation (5.2). Consequently,

- If B is reduced to a point m,

$$\mathcal{C}^{W^n}_m = \{x \in T_m M^N : h_m(pr_{TW^n} x, pr_{TW^n} x) = 0\}. \tag{5.28}$$

We deduce that $\mathcal{C}^{W^n}_m$ is the cone spanned by $\mathbf{C}^{W^n}_m$ and $T^\perp_m W^n$; that is, we have the direct generalization of the corresponding cone defined for surfaces in $\mathbb{E}^3$ in

Section 5.1.

- If W^{N-1} is a (smooth-oriented) hypersurface of $\mathbb{E}^N$ bounding a domain D, then

$$\mathcal{C}_B^D = \{x \in TM^N : \int_{W^{N-1}\cap B} h(pr_{TW^{N-1}}x, pr_{TW^{N-1}}x)dv = 0\}, \tag{5.29}$$

and

$$\mathcal{C}_B^{\mathrm{par},D} = \{x \in \mathbb{E}^N : \int_{W^{N-1}\cap B} h(pr_{TW^{N-1}}x, pr_{TW^{N-1}}x)dv = 0\}. \tag{5.30}$$

The case of polyhedra. We will extend Equations (5.29) and (5.30) to polyhedra. Let $\mathcal{D}$ be a domain in $\mathbb{E}^N$ bounded by a $(N-1)$-dimensional polyhedron P^{N-1}. For $X \in \mathcal{H}(P^N)$, we can evaluate $\Phi_{\mathcal{D}}^X$ above each simplex. In particular, if σ^{N-2} is a $(N-2)$-simplex, the support of $N(\mathcal{D})|_{\sigma^{N-2}}$ is the product $\sigma^{N-2} \times C_\sigma$, where C is a portion of circle. Let $(e_1, ..., e_{N-2})$ be an orthonormal frame field tangent to σ^{N-2}. Any point of $\sigma^{N-2} \times C_\sigma$ is a couple (m, e_{N-1}), where m is a point of σ^{N-2} and e_{N-1} is a unit vector orthogonal to σ^{N-2}. With these notations, we deduce from [38] or [23] (Theorem 72 page 216) that for any $B \in \mathcal{B}_{M^N}$,

$$\Phi_{\mathcal{D}}^X(B) = \sum_{\sigma^{N-2}\subset\partial P^N} \int_{(\sigma^{N-2}\cap B)\times C} < X, e_{(N-1)}^h >^2 . \tag{5.31}$$

We also deduce that for any $B \in \mathcal{B}_{\mathbb{E}^N}$,

$$\mathcal{C}_B^{\mathrm{par},\mathcal{D}} = \{x \in \mathbb{E}^N : \int_{(\sigma^{N-2}\cap B)\times C} < x^h, e_{(N-1)}^h >^2 = 0\}. \tag{5.32}$$

In particular, if $\mathcal{D}$ is a domain of $\mathbb{E}^3$ bounded by a polyhedron P^2, Equation (5.32) can be reduced to an explicit simple expression: First of all, we identify the (vector) plane $e^\perp$ orthogonal to any (oriented) edge e of P with $\mathbb{C}$, as follows : Let $n_1 \in e^\perp$ (*resp.* $n_2 \in e^\perp$) be the unit (oriented) normal to the faces f_1, (*resp.* f_2) incident to e.

Let e^+ (*resp.* e^-) be the (oriented) normalized vectors spanning the bisectors of n_1 and n_2 (so that (e^+, e^-, e) is a direct frame of $\mathbb{E}^3$). Any vector $ae^+ + be^-$ of $e^\perp$ is now identified with the complex number $a + ib$. An explicit integration over each term of type $(\sigma^1 \cap B) \times C$ in Equation (5.32) gives the following expression of the asymptotic measure and asymptotic cone:

Proposition 5.2

1. For any $B \in \mathcal{B}_{\mathbb{E}^3}$ and any *constant* vector field x of $\mathbb{E}^3$,

$$\Phi^x_{\mathcal{D}}(B) = \sum_{e \in \mathbf{E}} \frac{l(e \cap B)}{2} \big[(\angle(e) ||pr_{e^\perp} x||^2 - \sin(\angle(e)) \mathcal{R}\big((pr_{e^\perp} x)^2\big) \big], \qquad (5.33)$$

   where $\mathbf{E}$ denotes the set of edges of P^2, $\angle(e)$ the angle of the normal to the faces incident to e (being positive if and only if e is convex), $pr_{e^\perp}$ the orthogonal projection on $e^\perp$, and $\mathcal{R}(pr_{e^\perp} x)^2$ the real part of the complex number $(pr_{e^\perp} x)^2$.

2. In particular,

$$\mathcal{C}^{\mathrm{par},\mathcal{D}}_B = \{x \in \mathbb{E}^3 : \sum_{e \in \mathbf{E}} \frac{l(e \cap B)}{2} \big[(\angle(e) ||pr_{e^\perp} x||^2 - \sin(\angle(e)) \mathcal{R}\big((pr_{e^\perp} x)^2\big] = 0\}. \quad (5.34)$$

We remark that if the $\angle(e)$'s are "small enough" (this can happen for instance when P approximates "smoothly" a smooth surface), then $\sin(\angle(e))$ is "close to" $\angle(e)$ and

$$\Phi^x_{\mathcal{D}}(B) \sim \sum_{e \in \mathbf{E}} l(e \cap B) \angle(e) < x, e^- >^2 . \qquad (5.35)$$

And then,

$$\mathcal{C}^{\mathrm{par},\mathcal{D}}_B \sim \{x \in \mathbb{E}^3 : \sum_{e \in \mathbf{E}} l(e \cap B) \angle(e) < x, e^- >^2 = 0\}. \qquad (5.36)$$

After choosing a scale r, we construct from the previous construction, a *cone subbundle* of TM^N associated with a geometric subset of M^N. Let us denote by $B(m, r)$ the ball of radius r, centered at $m \in M^N$. With each point $m \in M^N$, and

for a fixed (small enough) real number $r > 0$, we associate the cone $\mathcal{C}^{\text{par},\mathcal{G}}_{B(m,r)}$.

Definition 5.4 We call $\cup_{m\in\mathbb{E}^N}\mathcal{C}^{\text{par},\mathcal{G}}_{B(m,r)}$ the cone subbundle of $T\mathbb{E}^N$ at scale r associated with $\mathcal{G}$.

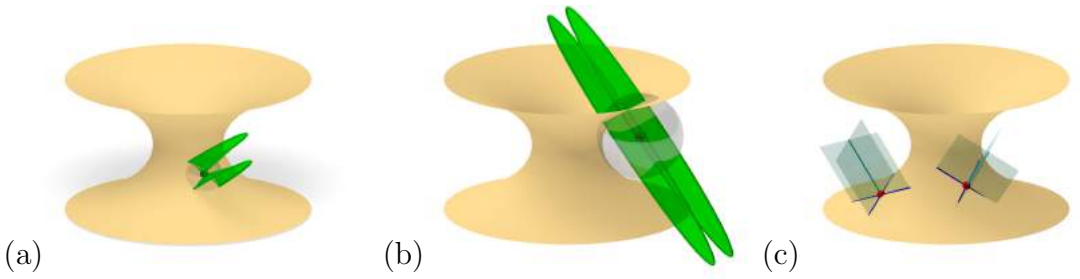

(a) (b) (c)

Figure 5.1: Some asymptotic cones built on a smooth surface (here on a portion of a catenoid) (a) An asymptotic cone in green whose vertex is at the center of its corresponding Borel set (a transparent ball) (b) The center of the ball may be out of the surface (c) When the Borel set is reduced to a single point on the surface, the asymptotic cone degenerates to the union of two planes

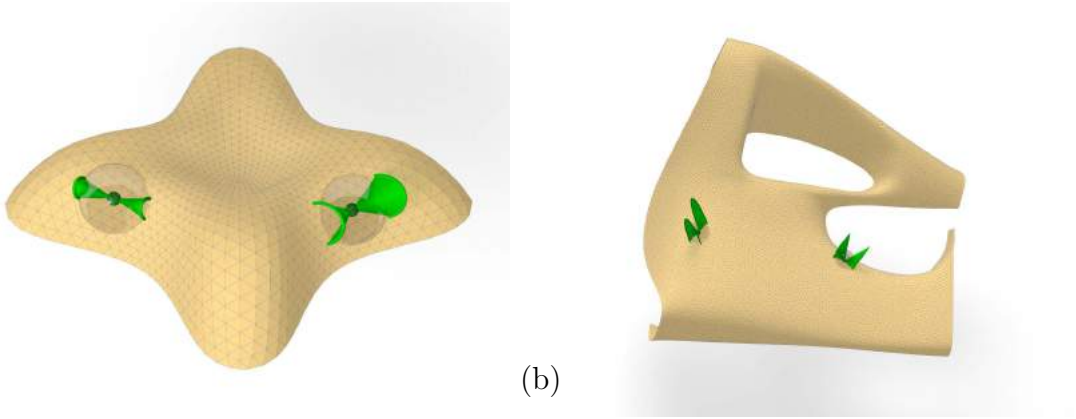

(a) (b)

Figure 5.2: (a) Asymptotic cones built on a non-smooth surface, here a triangulation: the top of the Lilium tower (designed by architect Zaha Hadid) in Warsaw, Poland. (b) Asymptotic cones built on a non smooth-surface. Here another triangulation: the Heydar Aliyev Center (designed by architect Zaha Hadid) in Baku, Azerbaijan

We remark that the dimension of each fiber may change with m. This bundle is defined over the whole M^N, even at the points m which are "far" from $\mathcal{G}$. If $B(m,r)$ does not intersect the support of $\mathcal{G}$, then $\mathcal{C}^{\text{par},\mathcal{G}}_{B(m,r)} = T_mM^N$. This phenomenon is visualized in Fig. 5.1 where the cone in Fig. 5.1(a) has its vertex (the black point) on the catenoid, and the cone in Fig. 5.1(b) has its vertex out of the catenoid. More

examples of asympotic cones are shown in Fig. 5.2.

5.4 Convergence and approximation results

In the previous paragraphs, we gave our first justification of the denomination of *asymptotic cones*. For surfaces W^2 in $\mathbb{E}^3$, this cone reduces at each point m of W^2 to (the product of the normal line by) the standard asymptotic directions of W^2 at m. We give now a second justification in terms of the convergence of sequences of polyhedra of $\mathbb{E}^N$. For simplicity, we restrict our study to (oriented) smooth hypersurfaces or polyhedra of $\mathbb{E}^N$ bounding a (compact) domain. We will show, in particular, that, if a sequence of domains $\mathcal{D}_k$ whose boundaries are polyhedra P_k^{N-1}, converges to a domain D whose boundary is a smooth hypersurface W^{N-1} (in a sense that will be clarified later), then for a large class of Borel subsets B, the sequence of asymptotic cones $\mathcal{C}_B^{\mathcal{D}_k}$ (resp. $\mathcal{C}_B^{\mathrm{par},\mathcal{D}_k}$) converges to $\mathcal{C}_B^D$ (resp. $\mathcal{C}_B^{\mathrm{par},D}$). We will use the following terminology [23]:

- The *fatness* $\Theta(P^{N-1})$ of a polyhedron P^{N-1} is defined as follows: If σ is an l-simplex, we begin to define the *size* $\epsilon(\sigma)$ of σ: It is the maximum over all edges e of σ of the length of e. Then, the *fatness* of σ is the real number

$$\Theta(\sigma) = \min_{\mu \ l\text{-simplex in } \sigma} \min_{j\in\{1,\ldots,l\}} \frac{vol_j(\mu)}{\epsilon(\sigma)^j}.$$

  Finally, the *fatness* of P is the minimum of the fatness of its simplices. We denote by $\mathbf{F}_\theta$ the class of polyhedra in $\mathbb{E}^N$ with fatness greater or equal to θ.

- An $(N-1)$ dimensional polyhedron P^{N-1} in $\mathbb{E}^N$ is *closely inscribed* in a smooth hypersurface W^{N-1} if its vertices belong to W^{N-1} and if the orthogonal projection of P^{N-1} onto W^{N-1} is a bijection.

- Let P^{N-1} be an $(N-1)$ dimensional polyhedron (bounding a domain $\mathcal{D}$) closely

inscribed in a smooth hypersurface W^{N-1} in $\mathbb{E}^N$. The *angular deviation* α_m between $m \in P^{N-1}$ and $pr_{W^{N-1}}(m)$ is the maximal angle between the normal $\xi_{pr_{W^{N-1}(m)}}$ of W^{N-1} and (m, n_m), where (m, n_m) belongs to the support of $\mathbf{N}(\mathcal{D})$. If B is any Borel subset of $\mathbb{E}^N$, we write

$$\alpha_B = \sup_{m \in B} \alpha_m.$$

One of the classical observations is that a "good" fatness of a polyhedron and a "small" Hausdorff distance of this polyhedron to a smooth hypersurface in which it is closely inscribed imply that the angular deviation is "small".

5.4.1 A convergence result

Let us state now our convergence theorem. For any cone $\mathcal{C}$, we denote by $\mathcal{UC}$ the basis of $\mathcal{C}$; that is, $\mathcal{UC} = \mathcal{C} \cap \mathbb{S}^{N-1}(0,1)$, where $\mathbb{S}^{N-1}(0,1)$ is the unit sphere centered at the origin. We also use the distance $\tilde{d}$ defined on the class of subsets of $\mathbb{E}^N$ by

$$\tilde{d}(A, B) = \inf_{x \in A, y \in B} d(x, y). \tag{5.37}$$

Theorem 5.1 Let D be a (compact) domain of $\mathbb{E}^N$ bounded by a smooth hypersurface W^{N-1}. Let $(\mathcal{D}_k)$ be a sequence of domains of $\mathbb{E}^N$ bounded by polyhedra (P_k^{N-1}) closely inscribed in W^{N-1} such that:

1. The limit of (P_k^{N-1}) is W^{N-1} for the Hausdorff distance.

2. The fatness of (P_k^{N-1}) is uniformly bounded from below by a non-negative constant: there exists $\theta > 0$ such that for all $k \in \mathbb{N}$, $P_k^{N-1} \in \mathbf{F}_\theta$.

Let $B \in \mathcal{B}_{\mathbb{E}^N}$, such that for all $x \in \mathbb{E}^N$, $|\Phi_D^x|(\partial B) = 0$. Then, every sequence $(x_k \in \mathcal{C}_B^{\mathcal{D}_k})$ of unit vectors admits a subsequence (still denoted by $(x_k \in \mathcal{C}_B^{\mathcal{D}_k})$) that

converges to a unit vector of $\mathcal{C}_B^D$. In particular,

$$\lim_{k\to\infty} \tilde{d}(\mathcal{UC}_B^{\mathrm{par},\mathcal{D}_k}, \mathcal{UC}_B^{\mathrm{par},D}) = 0. \tag{5.38}$$

In the smooth case, the assumption on the boundary of B can be translated in terms of the second fundamental form of W^{N-1}. We say that the *normal curvature* at a point p of a submanifold V of W^{N-1} is null if the second fundamental form h_p of W^{N-1} satisfies $h_p(u,u) = 0$ for every u tangent to V at p. We get:

Corollary 5.1 Under assumptions 1 and 2 of Theorem 5.1, suppose that B is a Borel set such that $W^{N-1} \cap \partial B$ is smooth and with null normal curvature. Then, the conclusion of Theorem 5.1 holds.

To prove this corollary, we simply remark that under these assumptions,

$$\Phi_D^x(\partial B) = \int_{W^{N-1}\cap\partial B} h(pr_{TW^{N-1}}x, pr_{TW^{N-1}}x) = 0. \tag{5.39}$$

The rest of this section focuses on the proof of Theorem 5.1.

Convergence of sequences of normal cycles. We need to introduce the *flat norm* on $\mathcal{D}_l(\mathbb{E}^N)$ as follows. The *mass* of an l-current T is the real number

$$\mathbf{M}(T) = \sup\{T(\omega)\}, \tag{5.40}$$

where the supremum is taken over all l-differential forms with compact support such that $\sup_{m\in\mathbb{E}^N} |\omega_m| \leq 1$. The flat norm of an l-current T is the real number

$$\mathcal{F}(T) = \inf\{\mathbf{M}(A) + \mathbf{M}(B)\}, \tag{5.41}$$

where the infimum is taken over all rectifiable l-currents A and $(l+1)$-currents B such that $T = A + \partial B$. Our main ingredient in our study of convergence and approximation

of the asymptotic cones is the following result, which is a simple reformulation of Theorem 67 of [23] (page 200) for polyhedra:

Theorem 5.2 If P^{N-1} is a closed $(N-1)$ dimensional polyhedron bounding a domain D and closely inscribed in a smooth closed hypersurface W^{N-1} of $\mathbb{E}^N$ bounding a domain $\mathcal{D}$, then for any Borel subset B of P^{N-1},

$$\begin{aligned}\mathcal{F}\big(\mathbf{N}(\mathcal{D})_{|T_B\mathbb{E}^N} - \mathbf{N}(D)_{|T_{pr_{W^{N-1}}B}\mathbb{E}^N}\big)&\\ \leq K(\delta_B + \alpha_B)\mathbf{M}(\mathbf{N}(\mathcal{D})_{|T_B\mathbb{E}^N}),&\end{aligned} \tag{5.42}$$

where δ_B is the Hausdorff distance between B and $pr_{W^{N-1}}(B)$ and K is a constant depending on the norm of the second fundamental form of W^{N-1}.

The following proposition can be deduced from Theorem 5.2 in a slightly different version, see also [65].

Proposition 5.3 Under the assumptions 1 and 2 of Theorem 5.1,

1. The masses $\mathbf{M}(\big(\mathbf{N}(\mathcal{D}_k)\big))$ are uniformly bounded from above;

2. The sequence $(\mathbf{N}(\mathcal{D}_k))$ converges to $\mathbf{N}(D)$ for the flat norm.

Convergence of sequences of asymptotic measures. Our framework is the space of (signed) Radon measures on $\mathbb{E}^N$ with finite total variation, endowed with the norm $||.||_1$ defined for every μ (with finite total variation $|\mu|$) by

$$||\mu||_1 = \int_{\mathbb{E}^N} d|\mu|.$$

It is well known that this space is the (topological) dual to the space $\mathcal{C}_c(\mathbb{E}^N)$ of continuous functions with compact support on $\mathbb{E}^N$, endowed with the norm $||.||$ defined by

$$||f|| = \sup_{x\in\mathbb{E}^N} |f(x)|.$$

The space of (signed) Radon measures (with finite total variation) can also be endowed with the topology of *weak convergence of measures*: a sequence of Radon measures (μ_k) on $\mathbb{E}^N$ (weakly) converges to μ if, for every continuous function f with compact support on $\mathbb{E}^N$ (*resp.* $T\mathbb{E}^N$), $\mu_k(f)$ converges to $\mu(f)$.

Proposition 5.4 Under the assumptions 1 and 2 of Theorem 5.1,

1. For each vector $x \in \mathbb{E}^N$, the sequence of measures $(\Phi^x_{\mathcal{D}_k})$ converges to Φ^x_D for the weak convergence of measures on $\mathbb{E}^N$;

2. For each unit vector $x \in \mathbb{E}^N$, the sequence of measures $(\Phi^x_{\mathcal{D}_k})$ is $||.||_1$-bounded.

Proof. Item 1 is a direct consequence of Proposition 5.3, since the flat convergence of the sequence of normal cycles $(\mathbf{N}(\mathcal{D}_k))$ implies the weak convergence of the measures $(\Phi^x_{\mathcal{D}_k})$. Item 2 is an application of the Theorem of Banach-Steinhaus: Since $(\Phi^x_{\mathcal{D}_k})$ converges to Φ^x_D for the weak convergence of measures on $\mathbb{E}^N$, for each $f \in \mathcal{C}_c(\mathbb{E}^N)$, $\sup_k | < \Phi^x_{\mathcal{D}_k}, f >< +\infty$. The Theorem of Banach-Steinhaus then implies that $||\Phi^x_{\mathcal{D}_k}||_1$ is uniformly bounded with respect to k; that is, the sequence of measures $(|\Phi^x_{\mathcal{D}_k}|)$ is $||.||_1$-bounded. □

Let us now explain our assumption on the boundary of the Borel subset B in Theorem 5.1. In general, the weak convergence of the sequence $(\Phi^x_{\mathcal{D}_k})$ *does not* imply the convergence of $(\Phi^x_{\mathcal{D}_k}(B))$ to $(\Phi^x_D(B))$ for every Borel subset. Indeed, generically, characteristic functions are not continuous. That is why we restrict our study to a class of Borel subsets with suitable boundaries with respect to D, such that we can use the following general lemma (see [92] Chapter 4 for instance):

Lemma 5.1 Let (μ_k) be a sequence of (signed) Radon measures on $\mathbb{E}^N$ such that

1. (μ_k) converges to μ for the weak topology,

2. the sequence $(|\mu_k|)$ of total variation of (μ_k) converges to a Radon measure ν, for the weak topology.

If the boundary ∂B of $B \in \mathcal{B}_{\mathbb{E}^N}$ satisfies $\nu(\partial B) = 0$, then

$$\lim_{k\to\infty} \mu_k(B) = \mu(B). \tag{5.43}$$

Since the sequence $(|\Phi^x_{\mathcal{D}_k}|)$ is $||.||_1$-bounded, we can extract a subsequence that converges. From Proposition 5.3 and Lemma 5.1, we deduce:

Proposition 5.5 Under assumptions 1 and 2 of Theorem 5.1, if $x \in \Xi(E^N)$ and $B \in \mathcal{B}_{\mathbb{E}^N}$ satisfy $|\Phi^x_D|(\partial B) = 0$, then

$$\lim_{k\to\infty} \Phi^x_{\mathcal{D}_k}(B) = \Phi^x_D(B). \tag{5.44}$$

The last step of the proof of Theorem 5.1 is to relate the behavior of the sequence $(\Phi^x_{\mathcal{D}_k})$ for any x to the behavior of their associated quadratic cones. For a fixed $B \in \mathcal{B}_{\mathbb{E}^N}$, we will study the quadratic forms $x \to \Phi^x_{\mathcal{D}_k}(B)$ and $x \to \Phi^x_D(B)$ introduced in Section 5.3.2. We use the norm of uniform convergence on the space of quadratic forms: A sequence of quadratic forms (q_k) defined on $\mathbb{E}^N$ *converges* to a quadratic form q if $\sup_{||x||=1} |q_k(x) - q(x)|$ tends to 0 when k tends to infinity.

Lemma 5.2 Let (q_k) be a sequence of quadratic forms defined on $\mathbb{E}^N$, which converges to a quadratic form q. Let (x_k) be a sequence of unit vectors in $\mathbb{E}^N$, such that for each $k \in \mathbb{N}$, x_k belongs to the isotropic cone $\mathcal{C}_k$ of q_k (i.e. $q_k(x_k) = 0$). Then there exists a subsequence of (x_k) that converges to a unit vector x belonging to the isotropic cone $\mathcal{C}$ of q.

Proof. We have

$$\lim_{k\to\infty} \sup_{||z||=1} |q(z) - q_k(z)| = 0. \tag{5.45}$$

Suppose that (x_k) is a sequence of unit vectors such that for all k, $x_k \in \mathcal{C}_k$. Then, by the compacity of the unit sphere, there exists a subsequence (that we still denote by

(x_k)), that converges to a unit vector x. From Equation (5.45), we deduce

$$\lim_{k\to\infty} |q(x_k) - q_k(x_k)| = \lim_{k\to\infty} |q(x_k)| = |q(x)| = 0, \tag{5.46}$$

which means that $x \in \mathcal{C}$. □

We remark that under the assumption of Lemma 5.2, we cannot claim that the sequence of Hausdorff distances between $\mathcal{UC}_k$ and $\mathcal{UC}$ tends to 0 when k tends to infinity, as shown in the following example. Consider the quadratic forms in $\mathbb{E}^3$ defined for every $k \in \mathbb{N}^*$ by

$$q_k(u, v, w) = \frac{1}{k}(u^2 + v^2 + w^2). \tag{5.47}$$

We have for every $k \in \mathbb{N}^* \mathcal{C}_k = \{0\}$, $\mathcal{C} = \mathbb{E}^N$, $\mathcal{UC}_k = \emptyset$ and $\mathcal{UC} = \mathbb{S}^{N-1}(0, 1)$.

The proof of Theorem 5.1 follows from Proposition 5.3, Lemma 5.1, Proposition 5.5 and Lemma 5.2.

5.4.2 An approximation result

In this section, for simplicity, we restrict our study to surfaces in $\mathbb{E}^3$. We assume that W^2 (bounding D) and P (bounding $\mathcal{D}$) are fixed, with P being closely inscribed in W^2. We suppose (without any restriction) that P is endowed with a triangulation, denoting by t a generic triangle, and by $r(t)$ its circum-radius. The following theorem compares the asymptotic cone of $\mathcal{D}$ over a Borel set B composed of a union of triangles of P and the asymptotic cone of D over the orthogonal projection $pr_{W^2}(B)$ of B on W^2. If C is the isotropic cone of a quadratic form q, we denote by $\mathcal{A}^\epsilon(UC)$ the set of unit vectors x ϵ-close to C; that is, $|q(x)| \leq \epsilon$.

Theorem 5.3 Let D be a domain of $\mathbb{E}^3$ bounded by a smooth hypersurface W^2. Let $\mathcal{D}$ be a domain of $\mathbb{E}^3$ bounded by a polyhedron $P \in \mathcal{F}_\theta$, $\theta > 0$ closely inscribed in

W^2. For any $\epsilon > 0$, there exists $\eta > 0$ such that if $\max\{r(t), t \in B\} \leq \eta$, then

$$\mathcal{UC}^{\mathrm{par},\mathcal{D}} \subset \mathcal{A}^{\epsilon}(\mathcal{UC}^{\mathrm{par},D}_{\mathrm{pr}_{W^2}(B)}). \tag{5.48}$$

In other words, roughly speaking, under the assumptions of Theorem 5.3, the asymptotic cones of $\mathcal{D}$ are close to the asymptotic cones of D. The proof uses the results of Section 5-2 of [38]. We summarize them in the following proposition.

Proposition 5.6 Under the assumptions of Theorem 5.3, for every unit vector x,

$$|\Phi^x_{\mathcal{D}}(B) - \Phi^x_D(\mathrm{pr}_{W^2}(B))| = \mathbf{K} \max\{r(t), t \in B\}, \tag{5.49}$$

where $\mathbf{K}$ is a constant depending on the area of B, the length of its boundary, the geometry of W^2, and θ.

If x is a unit vector belonging to $\mathcal{UC}^{\mathrm{par},\mathcal{D}}_B$, then Equation (5.49) implies that

$$|\Phi^x_D(B)| = \mathbf{K} \max\{r(t), t \in B\}. \tag{5.50}$$

Consequently, if the triangles of P have a sufficiently small circumradius, then

$$|\Phi^x_D(\mathrm{pr}_{W^2}(B))| \leq \epsilon. \tag{5.51}$$

The conclusion follows.

5.5 Some basic experiments

5.5.1 Construction of asymptotic directions of a triangulation

To mimic the smooth situation, it may be interesting to deduce asymptotic directions and asymptotic lines from the asymptotic cones defined on a singular surface. This construction may be achieved if one has a natural plane field on this surface. This is

the case for triangulated surfaces, where each triangle spans a plane. Then, to build asymptotic directions at a point of a triangulated surface P^2, associated to a Borel set B, one can proceed as follows (see Fig. 5.3 and 5.4):

1. Consider a point m on P^2 (bounding $\mathcal{D}$) and build a Borel set B around m; for instance, a ball centered at m with a suitable radius.

2. Build the asymptotic cone $\mathcal{C}_B^{\text{par},\mathcal{D}}$ whose vertex is m, associated with B.

3. Build the intersection of $\mathcal{C}_B^{\text{par},\mathcal{D}}$ with the plane spanned by the face of the triangle that contains m. The result is two directions, called the *asymptotic directions* of P^2 at m.

4. When m runs over the surface, build a cross field (reduced to a point when the cone is reduced to a point). By integrating the cross field, we have asymptotic lines.

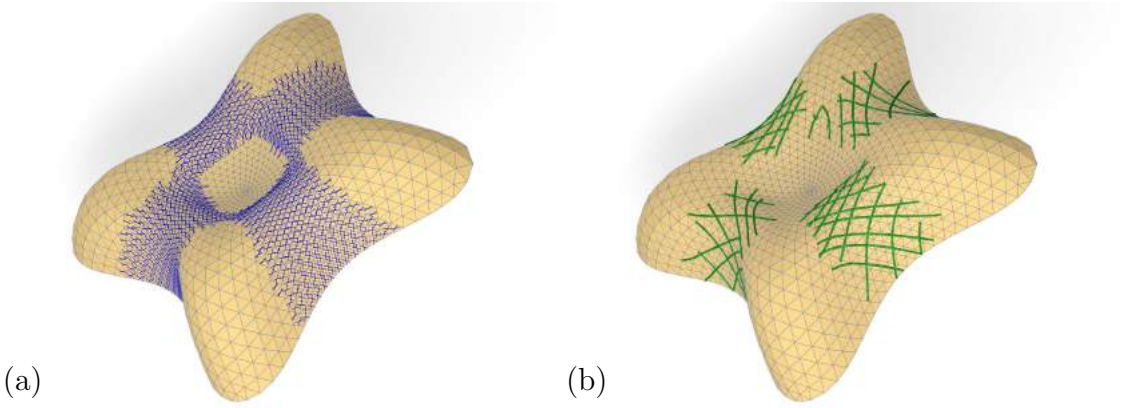

(a) (b)

Figure 5.3: (a) At each point where the asymptotic cone is not reduced to $\{0\}$, we build two asymptotic directions on the top of the Lilium tower. (b) By integration we have asymptotic lines.

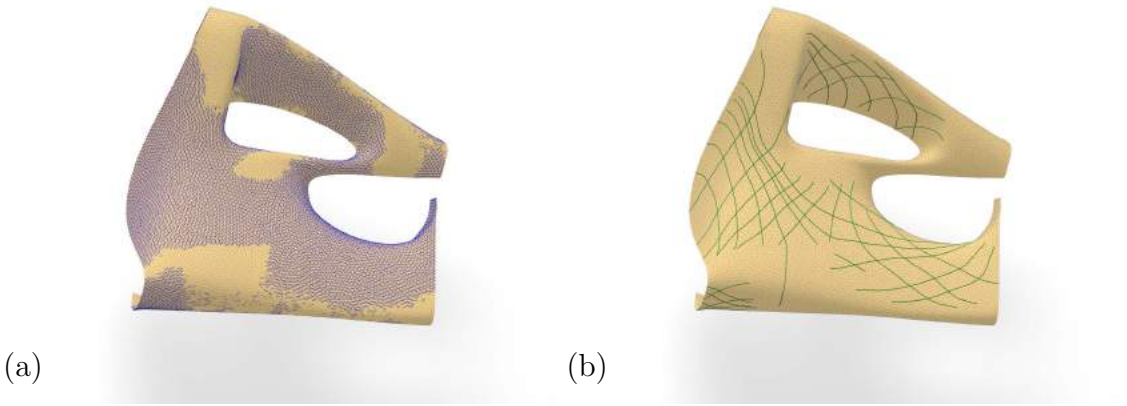

(a) (b)

Figure 5.4: (a) The cross field of asymptotic directions on the Heydar Aliyev Center in Baku. (b) The asymptotic lines obtained by integrating the asymptotic directions

5.5.2 Approximation of the asymptotic lines of a smooth surface

Using the construction of asymptotic cones, we can approximate the asymptotic directions (*resp.* lines) of a smooth surface W^2 in $\mathbb{E}^3$. We give an explicit example here.

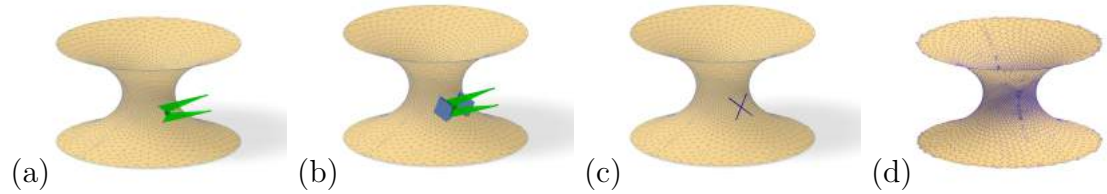

(a) (b) (c) (d)

Figure 5.5: (a) Step 1: A green asymptotic cone built at a point m of a triangulated surface approximating a (smooth) catenoid. (b) Step 2: The blue plane is an approximation of the tangent plane of the (smooth) catenoid at m. (c) Step 3: The intersection of the green asymptotic cone and the blue plane gives two lines intersecting at m. (d) Step 4: When m runs over the triangulation, we obtain a cross field that approximates the field of asymptotic directions of the (smooth) catenoid.

First of all, let us consider a portion of a (smooth) catenoid W^2, and a triangulation P^2 closely inscribed in W^2, with a sufficiently dense set of vertices. As shown in Fig. 5.5, the intersection of the tangent plane of W^2 at a point m with the asymptotic cone of a ball centered at m is reduced to two lines that are a discrete approximation of the asymptotic directions of W^2 at m. If necessary, we can approximate the tan-

gent plane itself by the plane spanned by a face of the triangulation. By integrating the directions field, we obtain discrete asymptotic lines, as shown in Fig. 5.6. The reader can compare the asymptotic lines directly built on the smooth catenoid (these lines are orthogonal since the catenoid is a minimal surface) with the "discrete ones" obtained by this procedure.

5.5.3 Comparison of asymptotic lines

We remark that the previous example gives (roughly speaking) "very good" results because the triangulated polyhedron approximating the catenoid suits it correctly, in the sense that the "good" fatness of the triangles implies that the normal of any triangle t is close to the normals of the orthogonal projection of t on the catenoid. To be more precise, we can estimate the error er as follows: Let W^2 be a smooth surface approximated by a triangulated polyhedron P^2 closely inscribed on it. Let m be a vertex of P^2, and let us denote by e_1 and e_2 the asymptotic directions of W^2 at m, and by ϵ_1, ϵ_2 the approximated asymptotic directions at m. We define

$$er_m = \inf\big(\frac{1}{2}(\angle(e_1,\epsilon_1)+\angle(e_2,\epsilon_2)), \frac{1}{2}(\angle(e_1,\epsilon_2)+\angle(e_2,\epsilon_1))\big), \tag{5.52}$$

where all the angles belong to $(0, \frac{\pi}{2})$.

For instance, let us consider the portion of the Enneper surface shown in Fig. 5.7, and a triangulated polyhedron closely inscribed on it. The error er is always less than or equal to 2.5 degrees.

In the following example, we show that, in accordance with the theory, the error may be large even with a very thin triangulation closely inscribed in a smooth surface, if the angle between the tangent plane at a point and the corresponding triangle is too large (the same phenomenon appears when one compares the area of a cylinder with the area of a Lantern of Schwarz inscribed on it, see [23] for instance). Here, we consider a (smooth) surface W^2 in $\mathbb{R}^3$ obtained as the graph of a tensor product

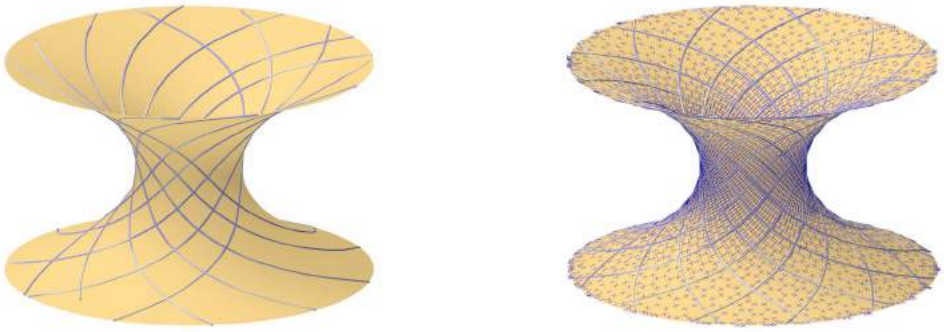

(a) (b)

Figure 5.6: (a) Integrating the cross field gives an approximation of the asymptotic lines of the catenoid. (b) The cross field is an approximation of the field of asymptotic directions on the (smooth) catenoid. They can be compared with the blue lines, which are the asymptotic lines directly computed on the (smooth) catenoid.

B-spline function

$$f : G = [0, 1] \times [0, 1] \to \mathbb{R},$$

of degree 3 in each variable, defined by 5×5 control points over a regular grid of 80×80 points. Each square of G is triangulated by taking both diagonals. We build the corresponding (piecewise linear) triangulation P^2 inscribed on W^2. Then, we compare, at each vertex m of the triangulation, the normal of W^2 at m and the average of the normals of the triangles incident to m. The error varies between 0 and 0.5 degree (see Fig. 5.8(b)). On the other hand, we compute on the same triangulation the asymptotic directions of W^2 and the asymptotic cones of P^2, from which we deduce discrete asymptotic directions by intersecting the cones with the tangent planes as before. Then, we compare at each point m the error er_m given in Fig. 5.8(a). The error at each vertex m varies between 0 and 5 degrees, according to the behavior of the normal of the faces incident to m with respect to the normal of W^2 at m.

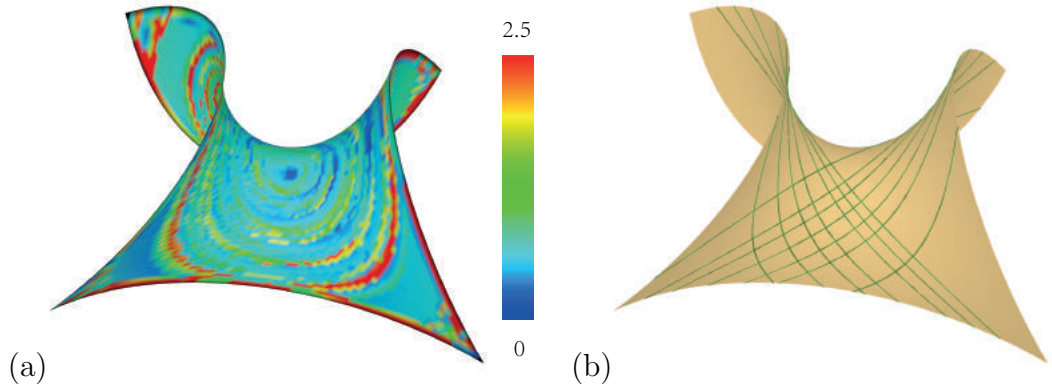

Figure 5.7: (a) Comparison of discrete and smooth asymptotic lines on the Enneper surface. This result shows that the difference between the approximated directions and theoretic ones are small when the triangulation is closely inscribed on its approximating smooth surface. (b) Some asymptotic lines computed on the polyhedron.

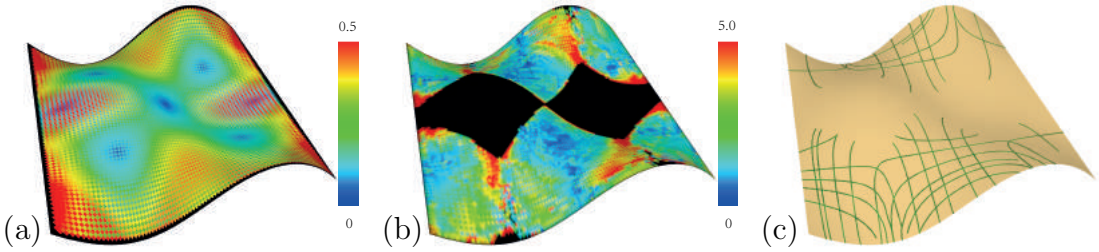

Figure 5.8: (a) Comparison of the normals computed on a B-spline surface and an approximating triangulation. (b) Comparison of the asymptotic directions by computing er_m at each vertex m (the black points are convex points, where the asymptotic cone is reduced to $\{0\}$. (c) Some asymptotic lines computed on the triangulation. Comparison with other existing methods of computing curvature lines is shown in Figure 4.10 in the previous chapter.

5.5.4 Deformation of asymptotic lines of discrete surfaces

In the following example (Fig. 5.9), we produce a deformation of "discrete" asymptotic lines as follows: We build a triangulation closely inscribed on a smooth surface W^2 (here a Chen's surface). We then compute asymptotic lines by the previous process using balls of radius $R = 3$ (the normalization is such that the average length of the edges is 1). Then, we slightly modify the position of the vertices that can now be out of W^2 (in other words, we create noisy data), without modifying the topology of the triangulation. With this new triangulation, we compute new asymptotic lines

using the same process and using balls of the same radius ($R = 3$) or a different radius ($R = 6$).

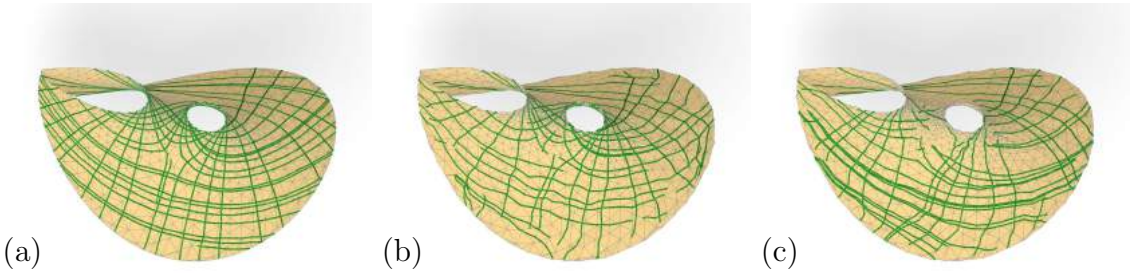

(a) (b) (c)

Figure 5.9: By perturbing the positions of the vertices of the approximated Chen's surface, we get noisy data and corresponding noisy discrete asymptotic lines. (a) The initial triangulation with asymptotic lines ($R = 3$). (b) Asymptotic lines with noisy data and $R = 3$. (c) Asymptotic lines with noisy data and $R = 6$. With larger size of the Borel subset, we can get more smooth asymptotic lines.

5.6 Application to face recognition

In this section we show how asymptotic cones are used as feature descriptors in face recognition.

5.6.1 Overview of the recognition process

The proposed asymptotic cones based 3D face recognition (FR) method here could be separated into the following parts (shown in Fig.5.10): face preprocessing, face alignment, curvatures extracted with help of asymptotic cones, creating three auxiliary 2D images called *curvature component faces*, extracting LNP (local normal pattern [73])-based facial descriptors from the curvature faces, W-SRC (weighted sparse representation-based classifier [93, 73]) matching and fusion. As a result we test the FR on FRGC v2.0 data base [69] with different fusions [94, 95] of the descriptors. Details can be found in [96]. Here we focus on the role that asymptotic cones play in this recognition process.

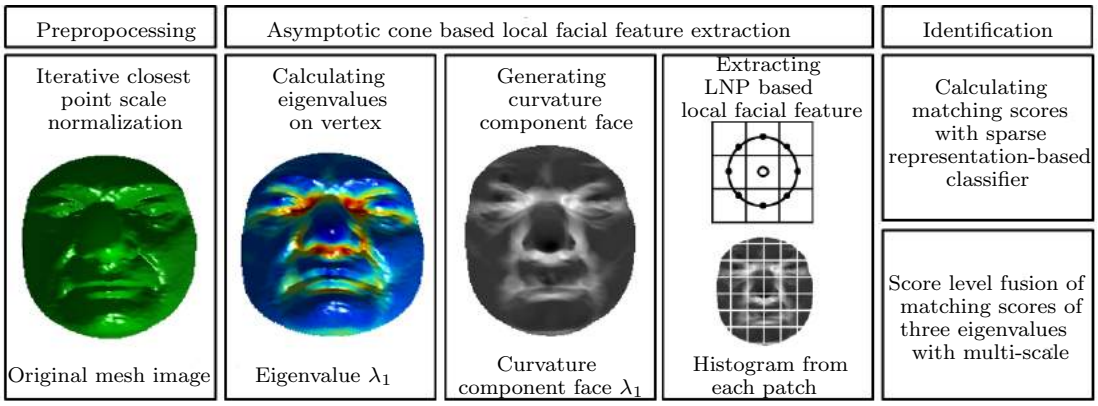

Figure 5.10: Flow of the recongition process.

5.6.2 Asymptotic cones as feature descriptors

The estimated principal curvatures has been extensively used as feature descriptors [97, 72, 74]. With the notion of asymptotic cone, we aim to use this new notion of curvature as feature descriptors, replacing the estimated principal curvatures. For the convenience in the computation (which is important in practice), we adapted a rotated asymptotic cone defined in [84]. It follows the equation:

$$\sum_{e \in E} l(e \cap B) \angle(e) < x, e >^2 = 0, \tag{5.53}$$

where the notations are defined as Equation (5.33). The selected cones over the faces are shown in Fig. 5.11. The left-hand-side of Equation (5.53) is quadratic in x and its matrix H is $\sum_{e \in E} l(e \cap B) \angle(e)\ e \cdot e^T$. The matrix H is exactly the *discrete anisotropic curvature measure* defined in [37]. Two of the three eigenvalues of H are estimated as principal curvatures [37, 98].

Our new descriptor is represented by all three eigenvalues λ_1, λ_2 and λ_3 of H. In the context of FR, we use the fusion of the three, formally $\lambda_1 + \lambda_2 + \lambda_3$, to represent this descriptor.

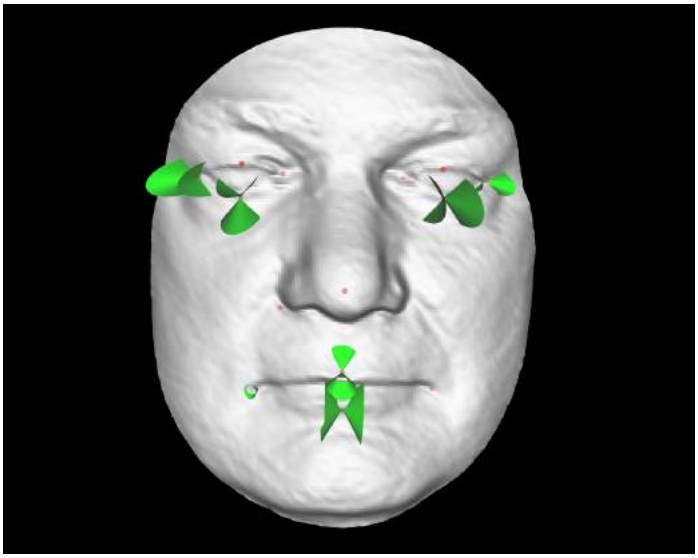

Figure 5.11: Asymptotic cones found around feature points [72](cones are colored in green and feature points are colored in red dots). Face data from FRGC v2.0 [69].

5.6.3 Experiment results

We test the discriminative power of each eigenvalue based LNP descriptor in each scale and their combinations as displayed in Table 5.1. The rank-1 recognition rate which uses the asymptotic cone (the fusion $\lambda_1 + \lambda_2 + \lambda_3$) as descriptors is higher than the one which uses the estimated principal curvatures (the fusion $\lambda_1 + \lambda_2$) at all the different scales.

Scale of Borel subset	Radius 3 (%)	Radius 5 (%)	Radius 7 (%)	Scale related Fusion (%)
λ_1	85.82	85.87	85.70	90.30
λ_2	85.87	85.48	85.33	89.99
λ_3	83.06	85.39	84.46	89.70
$\lambda_1 + \lambda_2$	89.42	89.56	88.79	92.23
$\lambda_1 + \lambda_2 + \lambda_3$	90.72	90.72	90.50	93.16

Table 5.1: Rank-1 identification rate of each eigenvalue related descriptor and the fusion under balls (Borel subsets) of different radius. λ_1 and λ_2 are the estimated discrete anisotropic curvatures. $\lambda_1 + \lambda_2$ is the fusion of the two, the same applies to $\lambda_1 + \lambda_2 + \lambda_3$.

This result indicates that each of the three eigenvalues are meaningful in FR based on a mesh model, and they can offer mutual complementary geometric information to improve the recognition performance. For more results, one may read [96].

Chapter 6

Concluding Remarks

The theory of discrete curvatures is a very broad topic that appears in various forms in mathematics and applications. In this thesis, we both contributed to theory and applications.

The first contribution is a combination of geometry and statics in form of the PMSEs. We discussed two ways of generating PMSEs. One is a propagating computation from Cauchy-like data. Here, we introduced the equilibrium surface and studied fairness conditions. The other is that we combine the computation with a global optimization to obtain more complex results without losing accuracy.

The second contribution addresses the discrete differential geometry of triangle meshes in combination with a study of discrete line congruences associated with such meshes. We discussed when a congruence defined by linear interpolation of vertex normals deserves to be called a normal congruence. Our main results are a discussion of various definitions of normality, a detailed study of the geometry of such congruences, and a concept of curvatures and shape operators associated with the faces of a triangle mesh. These curvatures are compatible with both normal congruences and the Steiner formula.

The third contribution is a study of asymptotic cones. With any smooth subspace or singular geometric subspace W of a Riemannian manifold M, we associated a family of cones, defined over any Borel subset of M. These cones are the generalization of the asymptotic directions defined at each point of a smooth surface of the Euclidean

space. We obtained convergence and approximation theorems when a sequence of polyhedra tends to a smooth subspace. We found good approximations of asymptotic lines of a triangulated surface and used asymptotic cones to generate descriptors for face recognition.

6.1 Future work

Topology editing in computing PMSEs It is practical to change the topology of a mesh in the process of computing and optimizing the mesh layer by layer. The current work will only generate PMSEs that are regular – all vertices are of valence four. More interesting examples can only be generated by including irregular vertices.

Material usage of PMSEs Special types of PMSEs are known to be optimal in the sense of minimal material usage [34]. It would be interesting to get more insight into these material minimizing structures and their shape limitations. In fact, even the shape restrictions on PMSEs are not yet fully understood.

Vanishing mean curvature in the triangle-based curvature theory It is still unclear how known constructions of special discrete surfaces relate to the curvatures defined here: For instance, we are lacking nice geometric properties from the condition of vanishing mean curvature. Nevertheless, one of the known constructions of discrete minimal surfaces might be equipped with a canonical normal congruence such that, when our theory is applied, mean curvature vanishes.

Deeper understanding of normality condition 3 Equation (4.12) of defining a normal congruence is stronger and applies the other two versions, but it is not precisely applicable to compute normals for any input triangle mesh. Meshes which have the ability to satisfy normality condition 3, their geometric properties and those of the derived normal congruences are a subject of further research.

Applications of line congruences Architectural applications of line congruences have been discussed by Wang et al. [36], but there might be other examples of geometry

processing tasks where the notion of line congruence, or even normal congruence, becomes relevant.

Principal cones It is natural to study if there are 'principal cones' that extend the concept of principal directions of a smooth manifold.

REFERENCES

[1] M. Kline, *Mathematical thought from ancient to modern times*, vol. 3. Oxford University Press, 1990.

[2] C. B. Boyer and U. C. Merzbach, *A history of mathematics*. John Wiley & Sons, 2011.

[3] G. A. Jennings, *Modern geometry with applications*. Springer Science & Business Media, 2012.

[4] S. M. Carroll, *Spacetime and geometry. An introduction to general relativity*, vol. 1. 2004.

[5] S. Katz, *Enumerative geometry and string theory*, vol. 32. American Mathematical Soc., 2006.

[6] E. Grinspun, M. Desbrun, K. Polthier, P. Schröder, and A. Stern, "Discrete differential geometry: an applied introduction," *ACM SIGGRAPH Course*, vol. 7, 2006.

[7] M. E. Mortenson, "Geometric modeling," 1997.

[8] W. Böhm, G. Farin, and J. Kahmann, "A survey of curve and surface methods in cagd," *Computer Aided Geometric Design*, vol. 1, no. 1, pp. 1–60, 1984.

[9] D. Marsh, *Applied geometry for computer graphics and CAD*. Springer Science & Business Media, 2006.

[10] H. Pottmann, A. Asperl, M. Hofer, and A. a. Kilian, *Architectural geometry*, vol. 10. Bentley Institute Press, 2007.

[11] M. Botsch, L. Kobbelt, M. Pauly, P. Alliez, and B. uno Levy, *Polygon Mesh Processing*. AK Peters, 2010.

[12] A. Bobenko and Y. Suris, *Discrete Differential Geometry: Integrable Structure*. American Math. Soc., 2009.

[13] A. I. Bobenko, J. M. Sullivan, P. Schröder, and G. M. Ziegler, *Discrete differential geometry*. Springer, 2008.

[14] M. Meyer, M. Desbrun, P. Schröder, and A. H. Barr, "Discrete differential-geometry operators for triangulated 2-manifolds," in *Visualization and mathematics III*, pp. 35–57, Springer, 2003.

[15] A. N. Hirani, *Discrete exterior calculus*. PhD thesis, California Institute of Technology, 2003.

[16] J. Cheeger, W. Müller, and R. Schrader, "On the curvature of piecewise flat spaces," *Communications in Mathematical Physics*, vol. 92, no. 3, pp. 405–454, 1984.

[17] G. Xu, "Discrete laplace–beltrami operators and their convergence," *Computer Aided Geometric Design*, vol. 21, no. 8, pp. 767–784, 2004.

[18] J. M. Sullivan, "Curvature measures for discrete surfaces," in *ACM SIGGRAPH 2005 Courses*, p. 3, ACM, 2005.

[19] A. I. Bobenko and P. Schröder, "Discrete willmore flow," in *ACM SIGGRAPH 2005 Courses*, p. 5, ACM, 2005.

[20] M. Jin, J. Kim, and X. D. Gu, "Discrete surface ricci flow: Theory and applications," in *Mathematics of Surfaces XII*, pp. 209–232, Springer, 2007.

[21] H. Pottmann, Y. Liu, J. Wallner, A. Bobenko, and W. Wang, "Geometry of multi-layer freeform structures for architecture," *ACM Trans. Graphics*, vol. 26, no. 3, pp. # 65,1–11, 2007. Proc. SIGGRAPH.

[22] M. Wardetzky, S. Mathur, F. Kälberer, and E. Grinspun, "Discrete laplace operators: no free lunch," in *Symposium on Geometry processing*, pp. 33–37, 2007.

[23] J.-M. Morvan, *Generalized Curvatures*, vol. 2 of *Geometry and Computing*. 2008.

[24] M. Jin, J. Kim, F. Luo, and X. Gu, "Discrete surface ricci flow," *Visualization and Computer Graphics, IEEE Transactions on*, vol. 14, no. 5, pp. 1030–1043, 2008.

[25] A. Bobenko, H. Pottmann, and J. Wallner, "A curvature theory for discrete surfaces based on mesh parallelity," *Math. Annalen*, vol. 348, pp. 1–24, 2010.

[26] H. Pottmann, M. Eigensatz, A. Vaxman, and J. Wallner, "Architectural geometry," *Computers and Graphics*, 2015. to appear.

[27] Y. Liu, H. Pottmann, J. Wallner, Y.-L. Yang, and W. Wang, "Geometric modeling with conical meshes and developable surfaces," *ACM Trans. Graphics*, vol. 25, no. 3, pp. 681–689, 2006. Proc. SIGGRAPH.

[28] H. Pottmann and J. Wallner, "The focal geometry of circular and conical meshes," *Adv. Comp. Math*, vol. 29, pp. 249–268, 2008.

[29] A. Bobenko, H. Pottmann, and J. Wallner, "A curvature theory for discrete surfaces based on mesh parallelity," *Math. Annalen*, vol. 348, pp. 1–24, 2010.

[30] P. Block and J. Ochsendorf, "Thrust network analysis: A new methodology for three-dimensional equilibrium," *J. Int. Assoc. Shell and Spatial Structures*, vol. 48, no. 3, pp. 167–173, 2007.

[31] P. Block, *Thrust Network Analysis: Exploring Three-dimensional Equilibrium*. PhD thesis, Massachusetts Institute of Technology, 2009.

[32] E. Vouga, M. Höbinger, J. Wallner, and H. Pottmann, "Design of self-supporting surfaces," *ACM Trans. Graphics*, 2012. Proc. SIGGRAPH.

[33] C. Tang, X. Sun, A. Gomes, J. Wallner, and H. Pottmann, "Form-finding with polyhedral meshes made simple," *ACM Trans. Graph.*, vol. 33, pp. 70:1–70:9, July 2014.

[34] T. Mitchell, "A limit of economy of material in shell structures," 2013.

[35] I. R. Porteous, *Geometric differentiation: for the intelligence of curves and surfaces*. Cambridge University Press, 2001.

[36] J. Wang, C. Jiang, P. Bompas, J. Wallner, and H. Pottmann, "Discrete line congruences for shading and lighting," *Computer Graphics Forum*, vol. 32, no. 5, pp. 53–62, 2013. Proc. Symp. Geometry Processing.

[37] D. Cohen-Steiner and J.-M. Morvan, "Restricted delaunay triangulations and normal cycle," in *Proceedings of the Nineteenth Annual Symposium on Computational Geometry*, SCG '03, (New York, NY, USA), pp. 312–321, ACM, 2003.

[38] D. Cohen-Steiner and J.-M. Morvan, "Second fundamental measure of geometric sets and local approximation of curvatures," *Journal of Differential Geometry*, vol. 74, pp. 363–394, 11 2006.

[39] J. H. G. Fu, "Monge-Ampere functions, I," *Indiana University Mathematics Journal*, vol. 38, pp. 745–771, 1989.

[40] P. Wintgen, "Normal cycle and integral curvature for polyhedra in riemmannian manifolds," *Differential geometry, Budapest 1979, Colloq. Math. Soc. Janos Bolyai*.

[41] P. Steadman, *Architectural morphology: An introduction to the geometry of building plans*. Taylor & Francis, 1983.

[42] C. Bovill and C. Bovill, *Fractal geometry in architecture and design*. Springer, 1996.

[43] H. Pottmann, M. Hofer, and A. Kilian, "Advances in architectural geometry," in *Proc. of Vienna conference*, 2008.

[44] M. J. Ostwald, "Fractal architecture: Late twentieth century connections between architecture and fractal geometry," *Nexus network journal*, vol. 3, no. 1, pp. 73–84, 2001.

[45] S. Frith, "Geometry and architecture," 2010.

[46] S. O'Shaughnessy, "Geometry in architecture," 2011.

[47] RFR, France, "Project for the Eiffel tower: Constructive geometry," in *Challenging Glass 3: Conference on Architectural and Structural Applications of Glass*, p. 93, IOS Press, 2012.

[48] H. Pottman, "Geometry and new and future spatial patterns," *Architectural Design*, vol. 79, no. 6, pp. 60–65, 2009.

[49] Y. Liu, H. Pan, J. Snyder, W. Wang, and B. Guo, "Computing self-supporting surfaces by regular triangulation," *ACM Transactions on Graphics (TOG)*, vol. 32, no. 4, p. 92, 2013.

[50] F. De Goes, P. Alliez, H. Owhadi, and M. Desbrun, "On the equilibrium of simplicial masonry structures," *ACM Transactions on Graphics (TOG)*, vol. 32, no. 4, p. 93, 2013.

[51] H. Pottmann and J. Wallner, *Computational line geometry*. Springer Science & Business Media, 2009.

[52] J. Yu, X. Yin, X. Gu, L. McMillan, and S. Gortler, "Focal surfaces of discrete geometry," in *Proc. Symp. Geometry Processing* (A. Belyaev and M. Garland, eds.), pp. 23–32, 2007.

[53] A. Doliwa, P. Santini, and M. Mañas, "Transformations of quadrilateral lattices," *J. Math. Phys.*, vol. 41, pp. 944–990, 2000.

[54] F. Cazals and M. Pouget, "Estimating differential quantities using polynomial fitting of osculating jets," *Computer Aided Geometric Design*, vol. 22, no. 2, pp. 121–146, 2005.

[55] H. Pottmann, J. Wallner, Q. Huang, and Y.-L. Yang, "Integral invariants for robust geometry processing," *Comput. Aided Geom. Design*, vol. 26, pp. 37–60, 2009.

[56] G. Eitan, G. Yotam, R. Jason, and Z. Denis, "Computing discrete shape operators on general meshes," *Computer Graphics Forum*, vol. 25, no. 3, pp. 547–556, 2006. Proc. Eurographics.

[57] H. Klaus and P. Konrad, "Generalized shape operators on polyhedral surfaces," *Computer Aided Geometric Design*, vol. 28, pp. 321–343, 2011.

[58] A. Bernig and L. Bröcker, "Courbures intrinseques dans les catégories analytico-géométriques," in *Annales de l'institut Fourier*, vol. 53, pp. 1897–1924, 2003.

[59] A. Bernig, "Curvature tensors of singular spaces," *Differential Geometry and its Applications*, vol. 24, no. 2, pp. 191 – 208, 2006.

[60] J. Cheeger, W. Müller, and S. Schrader, "Kinematic and tube formulas for piecewise linear spaces," *Indiana University Mathematics Journal*, vol. 35, pp. 737–754, 1986.

[61] J. Dai, W. Luo, S.-T. Yau, and X. D. Gu, "Geometric accuracy analysis for discrete surface approximation," in *Geometric Modeling and Processing - GMP 2006* (M.-S. Kim and K. Shimada, eds.), vol. 4077 of *Lecture Notes in Computer Science*, pp. 59–72, Springer Berlin Heidelberg, 2006.

[62] J. Dai, X. D. Gu, and F. Luo, *Variational Principles for Discrete Surfaces*. Advanced Lectures in Mathematics, International Press, 2008.

[63] H. Federer, "Curvature measures," *Trans. Amer. Math. Soc*, vol. 93, pp. 418–491, 1959.

[64] H. Federer, *Geometric measure theory*. Springer-Verlag, 1983.

[65] J. H. G. Fu, "Convergence of curvatures in secant approximations," *Journal of Differential Geometry*, vol. 37, no. 1, pp. 177–190, 1993.

[66] X. D. Gu and S.-T. Yau, *Computational Conformal Geometry*. Advanced Lectures in Mathematics, International Press, 2008.

[67] M. Zähle, "Integral and current representation of federer's curvature measures," *Archiv der Mathematik*, vol. 46, no. 6, pp. 557–567, 1986.

[68] P. J. Phillips, P. J. Flynn, T. Scruggs, K. W. Bowyer, J. Chang, K. Hoffman, J. Marques, J. Min, and W. Worek, "Overview of the face recognition grand challenge," in *Computer vision and pattern recognition, IEEE Computer Society Conference on,*, IEEE, 2005.

[69] K. W. Bowyer, K. Chang, and P. Flynn, "A survey of approaches and challenges in 3d and multi-modal 3d + 2d face recognition," *Computer vision and image understanding*, vol. 101, no. 1, pp. 1–15, 2006.

[70] C. Maes, T. Fabry, J. Keustermans, D. Smeets, P. Suetens, and D. Vandermeulen, "Feature detection on 3d face surfaces for pose normalisation and recognition," in *Biometrics: Theory Applications and Systems, IEEE International Conference on*, pp. 1–6, IEEE, 2010.

[71] I. A. Kakadiaris, G. Passalis, G. Toderici, M. N. Murtuza, Y. Lu, N. Karampatziakis, and T. Theoharis, "Three-dimensional face recognition in the presence of facial expressions: An annotated deformable model approach," *Pattern Analysis and Machine Intelligence, IEEE Trans. on*, vol. 29, no. 4, pp. 640–649, 2007.

[72] P. Szeptycki, M. Ardabilian, and L. Chen, "A coarse-to-fine curvature analysis-based rotation invariant 3d face landmarking," in *Biometrics: Theory, Applications, and Systems. IEEE International Conference on*, IEEE, 2009.

[73] H. Li, D. Huang, J.-M. Morvan, L. Chen, and Y. Wang, "Expression-robust 3d face recognition via weighted sparse representation of multi-scale and multi-component local normal patterns," *Neurocomputing*, vol. 133, pp. 179–193, 2014.

[74] K. Tonchev, A. Manolova, and I. Paliy, "Comparative analysis of 3d face recognition algorithms using range image and curvature-based representations," in *Intelligent Data Acquisition and Advanced Computing Systems (IDAACS), IEEE International Conference on*, IEEE, 2013.

[75] W. Hwang, X. Huang, K. Noh, and J. Kim, "Face recognition system using extended curvature gabor classifier bunch for low-resolution face image," in *Computer Vision and Pattern Recognition Workshops (CVPRW), IEEE Computer Society Conference on*, IEEE, 2011.

[76] J. Heyman, *The Stone Skeleton: Structural Engineering of Masonry Architecture*. Cambridge University Press, 1995.

[77] F. Fraternali, "A thrust network approach to the equilibrium problem of unreinforced masonry vaults via polyhedral stress functions," *Mechanics Res. Comm.*, vol. 37, no. 2, pp. 198 – 204, 2010.

[78] H. Pottmann and Y. Liu, "Discrete surfaces in isotropic geometry," in *Mathematics of Surfaces XII* (M. Sabin and J. Winkler, eds.), pp. 341–363, Springer, 2007.

[79] J. Nocedal and S. Wright, *Numerical optimization*. Springer Science & Business Media, 2006.

[80] Y.-L. Yang, Y.-J. Yang, H. Pottmann, and N. J. Mitra, "Shape space exploration of constrained meshes," *ACM Trans. Graph.*, vol. 30, pp. 124:1–124:12, Dec. 2011.

[81] V. Dragović and M. Radnović, *Poncelet porisms and beyond*. Basel: Birkhäuser, 2011.

[82] H. F. Baker, *Principles of Geometry*, vol. II. Cambridge University Press, 2nd ed., 1930.

[83] U. Simon, A. Schwenk-Schellschmidt, and H. Viesel, *Introduction to the affine differential geometry of hypersurfaces*. Science University of Tokyo, 1991.

[84] X. Sun and J.-M. Morvan, "Curvature measures, normal cycles and asymptotic cones," *Actes des rencontres du CIRM*, vol. 3, no. 1, pp. 3–10, 2013.

[85] T. Hoffmann, A. Sageman-Furnas, and M. Wardetzky, "A discrete parametrized surface theory in $\mathbb{R}^3$," arXiv preprint 1412.7293, 2014.

[86] W. Y. Lam and U. Pinkall, "Isothermic triangulated surfaces," arXiv preprint 1501.02587, 2015.

[87] B.-Y. Chen, *Geometry of Submanifolds*, vol. 22 of *Pure and applied mathematics*. New York, NY, USA: Marcel Dekker, 1973.

[88] M. P. do Carmo, *Riemannian Geometry*. Mathematics: Theory and Applications, 1992.

[89] J. Grifone, "Structure presque tangente et connexions I," *Annales de l'Institut Fourier*, vol. 22, no. 1, pp. 287–334, 1972.

[90] J. Grifone, "Structure presque tangente et connexions II," *Annales de l'Institut Fourier*, vol. 22, no. 3, pp. 291–338, 1972.

[91] F. Chazal, D. Cohen-Steiner, A. Lieutier, and B. Thibert, "Stability of curvature measures," in *Computer Graphics Forum*, vol. 28, pp. 1485–1496, Wiley Online Library, 2009.

[92] F. Maggi, *Sets of Finite Perimeter and Geometric Variational Problems*. Cambridge Studies in Advanced Mathematics, 2012.

[93] J. Wright, A. Y. Yang, A. Ganesh, S. S. Sastry, and Y. Ma

[94] M. Husken, M. Brauckmann, S. Gehlen, and C. Von der Malsburg, "Strategies and benefits of fusion of 2d and 3d face recognition," in *2005 IEEE Computer Society Conference on Computer Vision and Pattern Recognition (CVPR'05) - Workshops*, pp. 174–174, June 2005.

[95] D. Huang, Y. Tang, Y. Wang, L. Chen, and Y. Wang, "Hand-dorsa vein recognition by matching local features of multisource keypoints," *IEEE transactions on cybernetics*, vol. 45, no. 9, pp. 1823–1837, 2015.

[96] Y. Tang, X. Sun, D. Huang, J.-M. Morvan, Y. Wang, and L. Chen, "3d face recognition with asymptotic cones based principal curvatures," in *2015 International Conference on Biometrics (ICB)*, pp. 466–472, May 2015.

[97] G. G. Gordon, "Face recognition based on depth and curvature features," in *Computer Vision and Pattern Recognition, 1992. Proceedings CVPR'92., 1992 IEEE Computer Society Conference on*, pp. 808–810, IEEE, 1992.

[98] P. Alliez, D. Cohen-Steiner, O. Devillers, B. Lévy, and M. Desbrun, "Anisotropic polygonal remeshing," *ACM Trans. Graph.*, vol. 22, pp. 485–493, July 2003.